Alma Mater Studiorum - Università di Bologna

DOTTORATO DI RICERCA IN

MECCANICA E SCIENZE AVANZATE DELL'INGEGNERIA

Ciclo 36

Settore Concorsuale: 09/C2 - FISICA TECNICA E INGEGNERIA NUCLEARE

Settore Scientifico Disciplinare: ING-IND/10 - FISICA TECNICA INDUSTRIALE

CHARACTERIZATION OF HEAT PUMPS FOR DECARBONIZATION STRATEGIES IN THE FRAMEWORK OF BUILDING ENVELOPE – HVAC SYSTEM COUPLING

Presentata da: Vincenzo Ballerini

Coordinatore Dottorato

Lorenzo Donati

Supervisore

Eugenia Rossi di Schio

Co-supervisore

Gian Luca Morini

Matteo Dongellini

Esame finale anno 2024

Nothing in life is to be feared; it is only to be understood.

Marie-Skłodowska Curie

Abstract

In this doctoral thesis, the main research activities conducted during the three-year doctoral program are reported, focusing on analyses related to heat pumps. More specifically, various aspects of heat pumps have been analyzed, with particular emphasis on the analysis through dynamic simulations of the building-system interaction.

Initially, the performance of air-to-water heat pumps was analyzed under varying external climatic conditions. Subsequently, a dynamic analysis of performance was conducted, taking into account the defrost effect. Experimental analyses conducted in the Technical Physics Laboratory of the University of Bologna is also be presented. These experiments aimed to determine the performance of a dual-source heat pump, a thermal machine capable of simultaneously utilizing both ground and external air as thermal sources. In this context, the testing apparatus in the laboratory was also characterized.

Geothermal heat pumps coupled with vertical boreholes with ground-refill by means of thermal solar collectors were analyzed during the summer, involving long-term dynamic simulations. These simulations allowed for the determination of soil temperature drift with and without refill, as well as the effect of summer refill on annual machine performance.

Subsequently, with a focus on the energy crisis and the subsequent increase in energy prices following the Russo-Ukrainian war, the economic feasibility of using heat pumps instead of gas boilers for winter heating in Italy was studied. Various scenarios were considered, and energy and economic savings were analyzed by lowering the set-point temperature of heated spaces by 1 K, served by either a heat pump or a boiler.

Furthermore, comfort analyses were conducted to determine variations in comfort perception within a real building after the use of a gas boiler combined with cast-iron radiators or an air-to-air heat pump. These analyses were dynamic, Computational Fluid Dynamics (CFD), and experimental, aimed at validating the results obtained from the software used.

Considerable attention was also given to environmental issues, within the context of decarbonization through heat pumps. In particular, an analysis was conducted to

determine the CO_2 emissions of an electric heat pump connected to the Italian electrical grid. In this study, hourly CO_2 emission factors and approximate functions were determined for estimating the hourly CO_2 production due to the electrical consumption of appliances connected to the national grid. The study then focused on determining the annual carbon dioxide production from a heat pump.

Another environmental topic addressed (within the framework of the circular economy) was the reuse of materials (surgical masks) to create insulating panels for use in construction, with the aim of reducing energy losses and increasing indoor comfort in buildings.

Finally, a dynamic analysis was conducted on an existing building located in Bialystok (Poland, PL) to determine its performance before and after an energy retrofit intervention. The same building was then virtually relocated to Bologna to determine performance differences compared to the Bialystok case.

Contents

1. Introduction

In the current global and European energy landscape, the transition towards more sustainable solutions is not only the direction in which we are heading but is imperative. This transition is part of the decarbonization process, i.e., the reduction or complete elimination of carbon dioxide emissions and other greenhouse gases. More specifically, some of the strategies employed to reach the decarbonization goal include the adoption of renewable energies, energy efficiency, circular economy, and electrification. All these strategies will be discussed at various levels in the following chapters, but the focus will be mainly on heat pumps. In the European Union, buildings are responsible for about 40% of all energy required and are responsible for 36% of greenhouse gas emissions [**1, 2**]. Heat pumps (intended as vapor compression heat pumps and driven by an electric compressor) are crucial systems for decarbonization. In fact, compared to the systems traditionally used to meet the thermal demands of buildings (e.g., gas boilers), they have higher efficiency in energy utilization and can use electricity from renewable sources. They therefore fit perfectly into the European Green New Deal "Fit for 55" [**3, 4**], which foresees the reduction of greenhouse gas emissions by at least 55% by 2030 and the complete decarbonization of buildings throughout the Union by 2050.

In 1902, Willis Carrier invented the first air conditioner as known in our era, i.e., a device that can control both temperature and humidity. In 1929, J.A. Nekola invented the absorption heat pump, with a cycle in which a solution of water and ammonia flows). Subsequently, in 1930, the electric heat pump was invented and patented by Robert C. Webber. However, it was not until the 1950s that heat pumps began to gain popularity in the United States for heating buildings. A wider diffusion of these thermal machines occurred in the 1970s following the oil crises. Currently, research is mainly focused on maximizing efficiency and performance, using low environmental impact refrigerants, and integrating with renewable sources.

As previously mentioned, this work focuses attention on heat pumps; in particular, chapters 2 to 6 are entirely dedicated to discussing various aspects of heat pumps, while chapter 7 concerns analyses related to the energy efficiency of buildings and explores the utilization of repurposed materials in construction to enhance the energy efficiency of the buildings themselves.

In literature, the Seasonal Coefficient of Performance (SCOP) of air-source heat pumps is commonly determined utilizing standard weather data from cities/regions, derived from a Test Reference Year (TRY). However, it is crucial to note that the actual ambient

temperature can fluctuate significantly each year. Consequently, the real energy performance of air-source heat pumps systems may either underperform or, indeed, outperform the calculated predictions. While numerous studies in the literature delve into the dynamic simulation of heat pump heating systems in conjunction with residential and non-residential buildings, a limited number explore the impact of actual weather conditions (e.g., outdoor air temperature, which can exhibit substantial annual variations even within the same place) on the performances of air-source heat pumps [**5**-**7**]. Conducting such analyses is pivotal to avert the underestimation or overestimation of the advantages of utilizing a heat pump, particularly in terms of its cost-effectiveness and environmental impact. Air-source heat pumps performance is strongly influenced by external air climatic conditions. Therefore, an analysis was conducted to study the performance variation of these systems based on the climatic conditions of different locations where these machines are located. In Section 2.1, the outcomes of dynamic simulations will be showcased, which consider three distinct heat pump systems paired with an identical building, situated in three different Italian cities. These dynamic simulations were executed, taking into account real weather data (namely, outdoor air temperature, humidity, and solar radiation) pertinent to the aforementioned cities over an 8-year span (2013-2020). Additionally, the impact of weather compensation on the supply water temperature set-point on the seasonal performance of the heat pump will be analysed. Another impactful aspect on the performance of heat pumps is the formation of ice on the machine's evaporator during winter operation. Section 2.2 addresses this widely recognized issue inherent to air-source heat pumps. Indeed, under specific weather conditions, such as certain temperatures and relative humidity levels, if the evaporator coil’s surface temperature falls below the air dew point temperature and the water freezing point, ice forms on it, leading to a general degradation of the air-source heat pump's performance. The decline in the heat pump's performance is attributed to the reduction of the evaporator heat transfer coefficient, primarily for two reasons: the ice layer restricts the air flow through the heat exchanger, and it also acts as an insulant on the coil surface [**8**]. Numerous studies in literature explore the importance of temperature and relative humidity concerning frost accumulation on the heat pump's evaporator. In [**9**], Zhu et al. developed a frosting map (temperature–relative humidity) to guide defrosting control for air-source heat pumps, delineating three distinct zones in the frosting region, representing various frosting levels from severe to mild. The proposed map can be utilized to prevent mal-defrosting (an inadequate defrosting process) and enhance

defrosting efficiency. In several papers, such as [**10**–**12**], frosting/defrosting is considered from either a numerical or experimental perspective. Furthermore, a few works numerically explore the defrosting inverse cycle while considering the impact of real climate data. Section 2.2 will present a transient analysis on air-source heat pumps connected to residential buildings, taking into account the defrost effect on machine performance and electricity demand. The uniqueness of this analysis lies in its investigation into the defrost effect considering real climate data spanning 8 different years and for the same 3 Italian locations analyzed in Section 2.1, namely S. Benedetto del Tronto, Milan, and Livigno.

The dynamic analyses related to heat pump performance presented in Sections 2.1 and 2.2 will be complemented in Section 2.3 by experimental analyses on a dual-source heat pump, aiming to determine its performance in accordance with international standards [**13**]. A dual-source heat pump is a device capable of exploiting two different thermal sources: air and ground. These machines have the advantage of addressing some of the issues associated with air-source heat pumps and those coupled to the ground-source machines. Dual-source pumps offer better performance compared to air heat pumps, as they can utilize the ground in unfavourable climatic conditions (i.e. when the outdoor air temperature is too low and in climatic conditions favourable to frost formation on the evaporator). Moreover, the capability to exploit two different thermal sources allows for a reduced probe field compared to a heat pump solely coupled to the ground. The key advantages over air-source heat pumps include better performance, and compared to geothermal ones, a lower initial investment due to the requirement of a smaller probe field. Section 2.3 will also introduce the test bench used to evaluate the heat pumps, situated at the Technical Physics Laboratory of the University of Bologna [**14**].

As indicated in the previous paragraph, ground-coupled heat pumps exhibit good performance due to the stable temperature of the thermal source (i.e., the ground), but they have the disadvantage of high installation costs (mainly due to excavation, drilling, and positioning of the geothermal probes); a possible solution to have a smaller size and lower cost of the probe field is, as previously mentioned, a dual-source heat pump. Another alternative is to use a solar-assisted heat pump, i.e., a geothermal heat pump system served by thermal solar collectors that plan to use the heat collected by the solar collectors to heat the ground during the summer season. This analysis is presented in Chapter 3 and involves performing dynamic analyses for 15 years in different system

configurations: with different solar collector areas, with 4 different total lengths of the geothermal probe field, and in the presence or absence of refill (i.e., heating the ground during the summer using heat taken from the solar collectors). The results obtained show that refilling the ground during the summer mitigates soil temperature drift (i.e., the year-on-year temperature decrease due to the imbalance between summer and winter loads); moreover, adopting the refill is useful because even in the presence of an undersized probe field, acceptable machine performance can be obtained [**15**].

While the initial costs related to installing a heat pump system are crucial, they are not the only financial aspect to consider. The operational costs, specifically the annual expenses associated with using the heat pump, are equally significant and can influence long-term economic decisions. Chapter 4 delves into this by presenting an economic comparison concerning the heating of a building using a gas boiler versus an air-water heat pump, especially in the context of the Russo-Ukrainian conflict. Various works in the literature primarily focus on the economic relevance of a heat pump as an alternative to a gas boiler for residential building heating. The study by Ruffino et al. [**16**] demonstrated that while heat pumps are competitive against gas boilers, they are heavily dependent on refurbishment incentives and are penalized by the high electricity prices in Italy. Ala et al., in [**17**], presented an energetic and economic analysis of using heat pumps instead of gas boilers in the south of Italy; the results indicated that the competitiveness of the heat pump relative to a gas boiler is mainly influenced by the amount of thermal energy demand of the building. In 2020, Barnes and Bhagavathy [**18**] asserted that in the UK context, there is weak economic competitiveness of the heat pump compared with the gas boiler due to the taxes and levies that are heavily applied to domestic electricity bills compared with gas bills. The analysis presented in Chapter 4, in addition to making a comparison similarly to others in the literature, considers the price increases that occurred in Italy following the outbreak of the conflict between Russia and Ukraine.

The economic analysis detailed in Chapter 4 assumes the same annual thermal demand of the building for the heating season, regardless of whether a heat pump or a gas boiler is utilized. Recognizing the importance of this assumption, it was deemed necessary to further explore its implications through dynamic analyses on an existing residential building. Simultaneously, an examination of the achievable comfort within the building was conducted. Pivoting from the economic perspective, the subsequent chapter is related to comfort indexes, comparing the effects of heating with heat pumps to those

of gas boilers. In a practical scenario, the comfort levels within a small apartment in Bologna were assessed under two distinct heating systems: one using a gas boiler paired with radiators and the other, an air-to-air heat pump. The computational and dynamic evaluations were complemented by experimental measurements taken within the considered building. Emphasis was placed on comfort metrics, notably the PMV (Predicted Mean Vote) and the associated PPD (Predicted Percentage of Dissatisfied). For context, the PMV, developed by Fanger [**19**], is a comfort index ranging between +3 and -3. A value of 0 indicates optimal comfort, while values below 0 suggest a sensation of cold and values above denote discomfort due to warmth.

Some environmental aspects related to heat pumps are presented in Chapter 6. Electric vapor compression heat pumps play a crucial role in the decarbonization process, as they can use electricity produced from renewable sources; however, if the heat pump is connected to the electrical power grid, it will cause the production of carbon dioxide emissions, and such emissions depend on the mix of sources that have been used to produce the electricity then consumed by the thermal machine. In this chapter will be quantified the emissions of a heat pump serving a residential building and powered with electricity from the Italian national electricity grid; two models will also be introduced that provide the hourly CO_2 emission factor for the Italian scenario, also considering the exchange of electrical energy with other countries with which the Italian electrical grid is connected [**20**]. Various works in the literature focus on determining carbon dioxide emissions [**21-23**]. The majority of the models found in the literature, used to determine hourly emission factors, refer to the electricity produced in a single country, neglecting electricity exchanges with other countries. Noussan et al. [**24**] determine the hourly emission factors considering the total energy produced in Italy, for 6 years (2012–2017). Marrasso et al. in [**25**] determine the hourly emission factors (for years 2016 and 2017), considering the electric energy produced in Italy and neglecting the energy exchanges with foreign countries to which the Italian power grid is connected. The model presented to determine the emission factors in Chapter 6, considers the import and export of electrical energy to other countries, also because Italy is a country that has a very high electricity import from abroad.

The environmental aspects related to the use of heat pumps are addressed also in Chapter 7, focusing on the themes of energy efficiency and circular economy. The first theme is addressed in the second section of the chapter primarily, where a dynamic analysis on an existing building located in Bialystok (Poland, PL) is shown before and

after an energy efficiency intervention (insulation of the building's external walls and replacement of windows). The theme of the circular economy and recycling is addressed in the first part of the chapter, where a dynamic and experimental analysis related to insulating panels to be used in building, created with reused materials, will be presented.

Finally, Chapter 8 reports the main activities carried out during the 3 years of the doctoral programme and presents a report of the published works.

The analyses presented in the following chapters are basically dynamic, CFD, and experimental. From a dynamic perspective, Trnsys software was primarily used, particularly versions 17 and 18 [**26**, **27**], in combination with the Tess libraries [**28**], and additional types [**29**] to model condensing boilers and radiators with thermostatic valves. Furthermore, since most of the analyses pertain to heat pump systems combined with buildings, these buildings were modeled using Google SketchUp [**30**] and later imported in Trnsys employing the Trnsys3D Plugin [**31**]. CFD analyses, on the other hand, were conducted using the commercial software STAR-CCM+ [**32**]. Experimental analyses carried out in the laboratory concerning heat pumps and reported in chapter 2 were performed using the test bench available at the laboratory for studying heat pumps. Experimental analyses to determine the thermal conductivity of insulating materials used in construction were carried out using a machine designed to determine thermal conductivity as prescribed by the standard [**33**].

Moreover, the experimental analyses presented in chapter 5, conducted in a residential building in Bologna to determine comfort and energy demand, were carried out using typical instrumentation to obtain the needed physical quantities (thermoresistances and thermocouples for temperature measurement, globe thermometer for measuring mean radiant temperature, anemometers to determine air velocity at various points in the room, and an infrared thermal camera to identify thermal bridges). In addition, the analyses presented in Chapter 7 concerning the public building located in Bialystok were supplemented with actual annual consumption measurements. Specifically, monthly consumption from bills was analyzed and compared with values obtained from dynamic simulation software.

References

[1]: European Commission. Renovation and decarbonisation of buildings https://ec.europa.eu/commission/presscorner/detail/en/IP_21_6683 (accessed on 4 October 2023).

[2]: Maghrabie HM, Elsaid K, Sayed ET, Abdelkareem MA, Wilberforce T, Olabi AG.Building-integrated photovoltaic/thermal (BIPVT) systems: applications andchallenges. Sustainable Energy Technol Assess 2021;45. https://doi.org/10.1016/j.seta.2021.101151.

[3]: Stepping up Europe's 2030 Climate Ambition Investing in a Climate-Neutral Future for the Benefit of Our People; European Commission: Brussels, Belgium, 2020.

[4]: European Commission. Climate Action Paris Agreement. Available online: https://unfccc.int/process-and-meetings/the-paris-agreement/the-paris-agreement (Accessed on 4 October 2023).

[5]: G. A. Mouzeviris, K. T. Papakostas, Air-to-water heat pumps: the impact of climate, compressor technology, water output temperature and sizing on the seasonal coefficient of performance for heating, IOP Conference Series: Materials Science and Engineering, Volume 997, 2020 https://doi.org/10.1088/1757-899X/997/1/012150.

[6]: G. A. Mouzeviris, K. T. Papakostas, Seasonal heat performances of air-to-water heat pumps in the Greek climate, IOP Conference Series: Earth and Environmental Science, Volume 410, 2019, https://doi.org/10.1088/1755-1315/410/1/012043.

[7]: C. Naldi, M. Dongellini, GL. Morini, Climate influence on seasonal performances of air-to-water heat pumps for heating, Energy Procedia, 2015 https://doi.org/10.1016/j.egypro.2015.12.064.

[8]: Dongellini, M.; Piazzi, A.; De Biagi, F.; Morini, G.L. The modelling of reverse defrosting cycles of air-to-water heat pumps with TRNSYS. E3S Web Conf. 2019, 111, 01063. https://doi.org/10.1051/e3sconf/201911101063.

[9]: Zhu, J.; Sun, Y.; Wang, W.; Deng, S.S.; Ge, Y.; Li, L. Developing a new frosting map to guide defrosting control for air-source heat pump units. Appl. Therm. Eng. 2015, 90, 782–791. https://doi.org/10.1016/j.applthermaleng.2015.06.076.

[10]: Wang,W.; Zhang, S.; Li, Z.; Sun, Y.; Deng, S.;Wu, X. Determination of the optimal defrosting initiating time point for an ASHP unit based on the minimum loss coefficient

in the nominal output heating energy. Energy 2020, 191, 116505. https://doi.org/10.1016/j.energy.2019.116505.

[11]: Huang, W.; Zhang, T.; Ji, J.; Xu, N. Numerical study and experimental validation of a direct-expansion solar-assisted heat pump for space heating under frosting conditions. Energy Build. 2019, 185, 224–238. https://doi.org/10.1016/j.enbuild.2018.12.033.

[12]: Mengjie, S.; Shengchun, L.; Shiming, D.; Zhili, S.; Huaxia, Y. Experimental investigation on reverse cycle defrosting perfor-mance improvementfor an ASHP unit evenly adjusting the refrigerant distribution in its outdoor coil. Appl. Therm. Eng. 2017, 114. https://doi.org/10.1016/j.applthermaleng.2016.11.206.

[13]: UNI EN 14511-3, Air Conditioners, Liquid Chilling Packages and Heat Pumps for Space Heating and Cooling and Process Chillers, with Electrically Driven Compressors - Part 3: Test Methods, 2018.

[14]: Dongellini, M.; Ballerini, V.; Morini, G.L.; Naldi, C.; Pulvirenti, B.; Rossi di Schio, E.; Valdiserri, P. A New Climate Chamber for Air-Source and Ground-Source Heat Pump Testing Based on the Hardware-in-the Loop Approach: Design and Cross Validation. Journal of Building Engineering 2023, 64, 105661, https://doi.org/10.1016/j.jobe.2022.105661.

[15]: Ballerini, V.; Rossi di Schio, E.; Valdiserri, P.; Naldi, C.; Dongellini, M. A Long-Term Dynamic Analysis of Heat Pumps Coupled to Ground Heated by Solar Collectors. Applied Sciences 2023, 13, 7651, http://www.doi.org/10.3390/app13137651.

[16]: Ruffino, E.; Piga, B.; Casasso, A.; Sethi, R. Heat Pumps, Wood Biomass and Fossil Fuel Solutions in the Renovation of Buildings: A Techno-Economic Analysis Applied to Piedmont Region (NW Italy). Energies 2022, 15, 2375. https://doi.org/10.3390/en15072375.

[17]: Ala, G.; Orioli, A.; Di Gangi, A. Energy and Economic Analysis of Air-to-Air Heat Pumps as an Alternative to Domestic Gas Boiler Heating Systems in the South of Italy. Energy 2019, 173, 59–74. https://doi.org/10.1016/j.energy.2019.02.011.

[18]: Barnes, J.; Bhagavathy, S.M. The Economics of Heat Pumps and the (Un)Intended Consequences of Government Policy. Energy Policy 2020, 138, 111198. https://doi.org/10.1016/j.enpol.2019.111198.

[19]: Fanger O. 1970. Thermal Comfort. Copenhagen.

[20]: Valdiserri, P.; Ballerini, V.; Rossi di Schio, E. Interpolating Functions for CO2 Emission Factors in Dynamic Simulations: The Special Case of a Heat Pump. Sustainable Energy Technologies and Assessments 2022, 53, 102725, https://doi.org/10.1016/j.seta.2022.102725.

[21]: Clauß J, Stinner S, Solli C, Lindberg K, Madsen H, Georges L. A Generic Methodology to Evaluate Hourly Average CO2eq. Intensities of the Electricity Mix to Deploy the Energy Flexibility Potential of Norwegian Buildings.; 10th International Conference on System Simulation in Buildings (Liege, December 2018).

[22]: Hamels S. CO2 intensities and primary energy factors in the future European electricity system. Energies 2021;14:2165. https://doi.org/10.3390/en14082165.

[23]: Neirotti F, Noussan M, Simonetti M. Towards the electrification of buildings heating - Real heat pumps electricity mixes based on high resolution operational profiles. Energy 2020;195:116974. https://doi.org/10.1016/j.energy.2020.116974.

[24]: Noussan M, Roberto R, Nastasi B. Performance indicators of electricity generation at country level—The case of Italy. Energies 2018;11:650. https://doi.org/10.3390/en11030650.

[25]: Marrasso E, Roselli C, Sasso M. Electric efficiency indicators and carbon dioxide emission factors for power generation by fossil and renewable energy sources on hourly basis. Energy Convers Manage 2019;196:1369–84. https://doi.org/10.1016/j.enconman.2019.06.079.

[26]: Marrasso 17. Klein, S.A.; Duffie, A.J.; Mitchell, J.C.; Kummer, J.P.; Thornton, J.W.; Bradley, D.E.; Arias, D.A.; Beckman, W.A.; Braun, J.E.; et al.; TRNSYS 17: A Transient System Simulation Program; University of Wisconsin: Madison, WI, USA, 2010.

[27]: Klein, S.A.; Beckman, W.A.; Mitchell, J.W.; Duffie, J.A.; Duffie, N.A.; Freeman, T.L.; Mitchell, J.C.; Braun, J.E.; Evans, B.L. (2018). TRNSYS Version 18: A Transient System Simulation Program.

[28]: Thornton, J.W.; Bradley, D.E.; McDowell, T.P.; Blair, N.J.; Duffy, M.J.; LaHam, N.D.; Naik, A.V. (2013). TessLibs 17 – Applications Library Mathematical Reference.

[29]: Holst, S. (2023). RNSYS-Models for Radiator Heating Systems. https://trnsys.de/static/641c965bac4f593c3b4cc569839a51c2/Type_361_362_320_en.pdf. (Accessed on 4 September 2023).

[30]: Trimble Inc. (2023). Google SketchUp Make 2015. https://www.sketchup.com. (Accessed on 4 September 2023).

[31]: Hiller, M.; Kendel, C. (2023). TRNSYS3D - Plugin for SketchUp. https://trnsys.de/static/deb3060a15c25a7ad170db124507ef37/T3d_Manual.pdf. (Accessed on 4 September 2023).

[32]: CD-adapco. STAR-CCM+ Version 15.04.010; CD-adapco (Siemens): Melville, NY, USA, 2022.

[33]: BSI, British Standard Institution., 2001., Thermal performance of building materials and products - Determination of thermal resistance by means of guarded hot plate and heat flow meter methods - Products of high and medium thermal resistance, (Standard No. 12667)

2 Performance analyses of air-to-water heat pumps

In this chapter, three distinct analyses of heat pump performance will be presented: the first two are dynamic analyses conducted using a dynamic simulation software, while the final section pertains to experimental analyses carried out on a dual-source heat pump.

2.1 Analysis of air-to-water heat pumps under variable climatic conditions

The first analyses conducted regarding heat pumps were aimed at determining the seasonal performance of thermal machines (particularly air-to-water machines), taking into account the actual operating conditions of the machine [**1**]. The analyses were carried out using dynamic simulation software. In this type of analysis, Test Reference Years (TRY) are typically used to determine the seasonal performance of machines. These typical climatic years provide hourly values of various climatic variables (dry bulb temperature, humidity, wind speed and direction, radiation) for a given location. Their use in climate simulation software not only allows for determining machine performance under conditions close to reality but also enables the accurate estimation of the thermal demand of a building in a given location. In the conducted analysis, the objective was to determine the difference in terms of building thermal demand and electrical energy required by the heat pump considering one Test Reference Years and using hourly weather data measured and obtained from meteorological stations in three Italian locations. Three different heat pump systems coupled with the same building, located in three different Italian cities were considered: S. Benedetto del Tronto (Central Italy, 42°58’ North, 13° 53’ East), Milan (North of Italy, 45°28’ North, 9° 10’ East) and Livigno (North of Italy, 46°28’ North, 10° 8’ East). Dynamic simulations have been carried out considering real weather data (i.e. outdoor air temperature, humidity and solar radiation) referred to the three abovementioned cities for a period of 8 years (2013-2020). The influence of the weather compensation of supply water temperature set-point on the heat pump seasonal performance was also analysed and the analyses were restricted to the heating season.

2.1.1. Building description

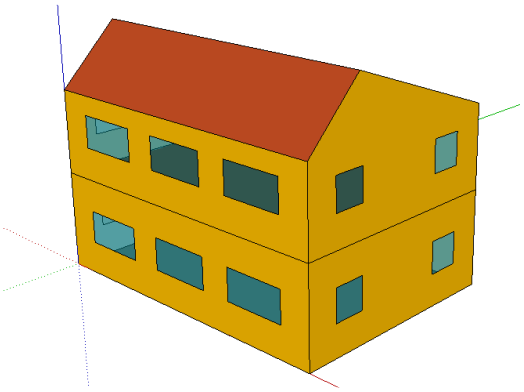

Figure 2.1 – 3D view of the building.

The building analysed in the tests refers to the residential building type proposed by IEA Task 44 [2] for conducting energy analyses using dynamic simulation software. More specifically, the building is a detached single-family villa arranged on two floors, with a total floor area of 360 m^2 (3D view in **Figure 2.1**) and an annual specific heating demand of 45 kWh/(m^2y) in the standard climate of Strasbourg, as established in [2]. The building was modelled in Trnsys [3] using Type 56 (multizone building) [4]. **Table 2.1** provides the transmittances and thicknesses of the main envelope components.

Table 2.1 – Thickness and U-value of the main envelope components.

Envelope component	**Thickness (m)**	**U-value (W/m^2K)**
External wall	0.318	0.364
Floor	0.185	0.235
Ground floor	0.385	0.241
Internal wall	0.200	0.885
Roof	0.285	0.694

2.1.2. Heat pumps and heating system layout

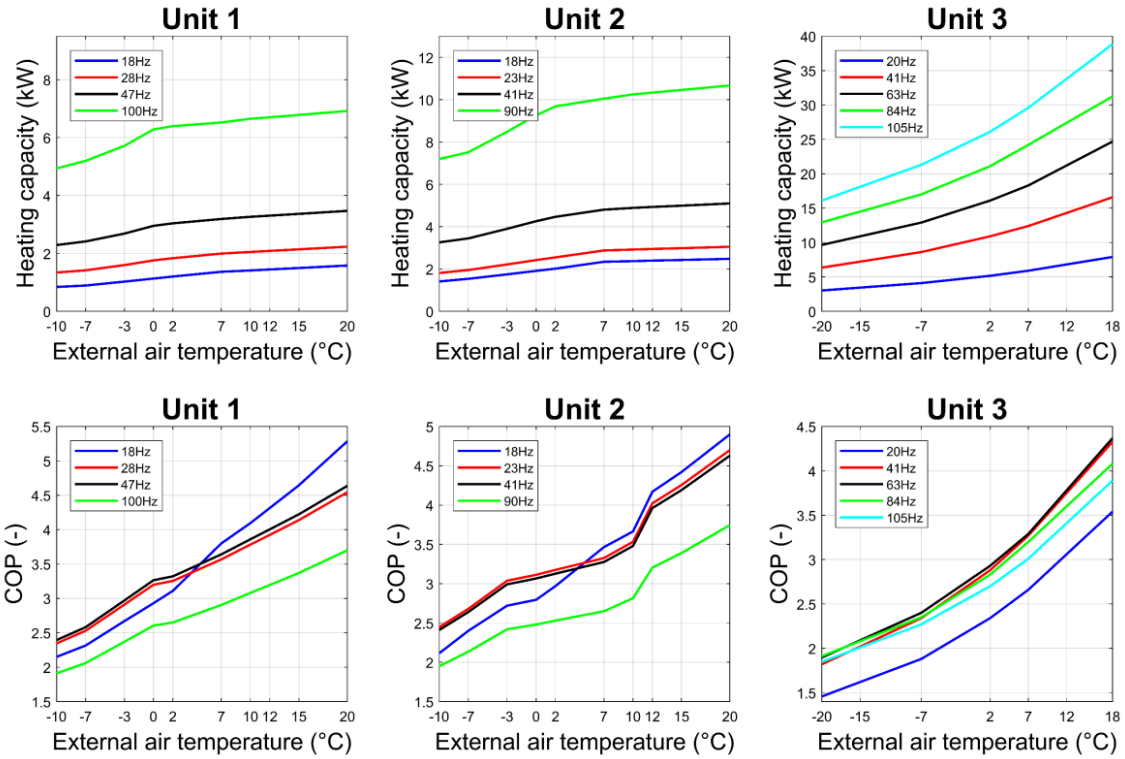

Figure 2.2 – Performance (heating capacity and COP) of the three heat pumps.

The analysis was conducted considering three different electric air-to-water heat pumps, whose performance (namely, the coefficient of performance COP and thermal power) is shown in Figure 2.2 for different compressor inverter frequencies. Unit 1 was paired with the building located in S. Benedetto del Tronto, Unit 2 was matched with the building located in Milan, and Unit 3 was associated with the building situated in Livigno. As illustrated in Figure 2, Units 1 and 2 exhibit similar thermal power and COP values, while Unit 3 demonstrates higher thermal power values. The selected heat pumps were chosen to fully meet the thermal energy demand of the building, i.e., to maintain the indoor air set-point temperature at 20°C when the outdoor ambient temperature reaches the winter design temperature.

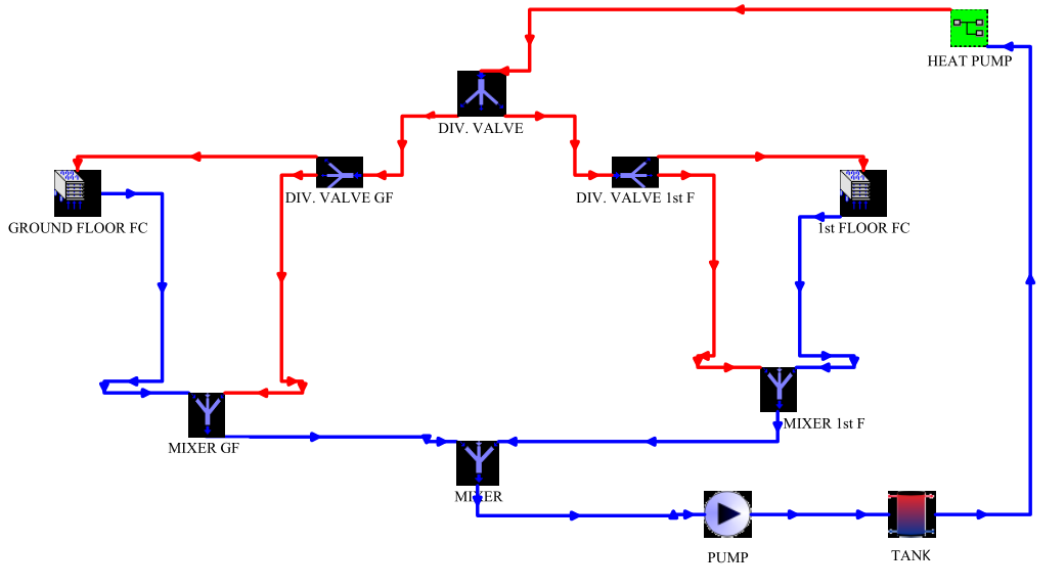

Figure 2.3 – Layout of the heating system as implemented in Trnsys.

Figure 2.3 illustrates the layout of the heating system, comprising the heat pump, the terminal units consisting of 2-pipe three-speed fan-coils, the circulation pump, and a 0.2 m^3 storage tank. The modelling includes only two heating zones, corresponding to the two floors of the building, with each thermal zone featuring a single fan-coil. The storage tank remains consistent across all considered scenarios, while the fan-coils have been dimensioned to meet the specific thermal power requirements of each building floor. To elaborate further, for the Milan building, the two fan-coils have nominal heating capacities of 10 kW and 7 kW, for the S. Benedetto building, each fan-coil boasts a nominal heating capacity of 5.5 kW, whereas, for Livigno, each unit's size increases to 12 kW and 10 kW, because of the higher thermal load.

2.1.3. Weather data

Table 2.2 – Winter design temperature, heating degree days (HDDs) and heating season for the three municipalities considered.

Municipality	Design temperature (°C)	HDDs	Heating season
Livigno	-19	4648	1 January – 31 December
Milan	-5	2404	15 October – 15 April
S. Benedetto del Tronto	-1	1533	1 November – 15 April

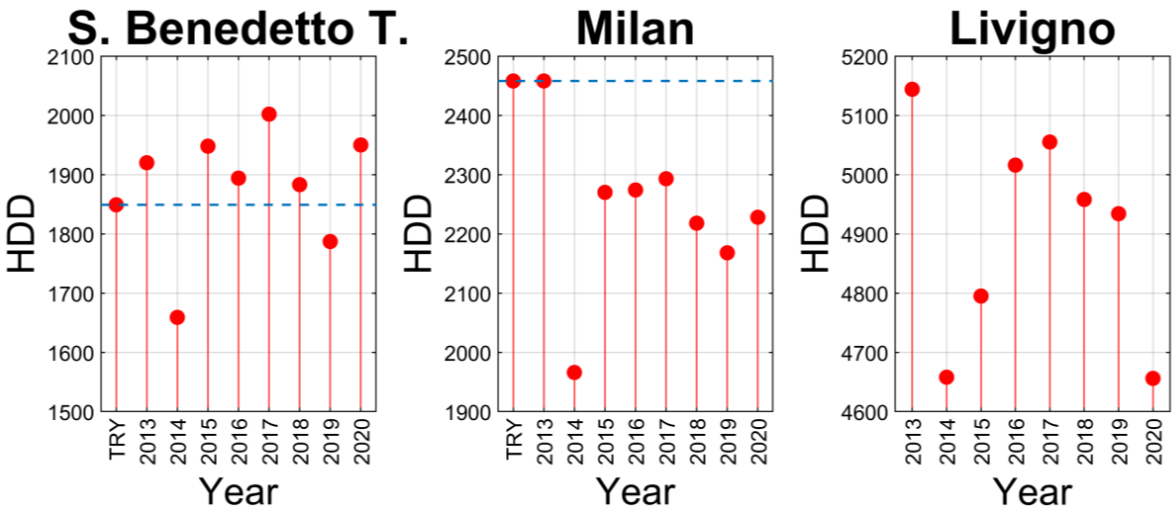

Figure 2.4 – Heating degree days (HDD) related to the three municipalities considered.

In the analysis, three Italian cities with different climates were considered: Livigno, a small town located in the Alps, S. Benedetto del Tronto, a coastal city in central Italy, and Milan, a metropolitan city in northern Italy's Po Valley. Specifically, Livigno experiences a very cold climate, requiring heating even during the summer period; in fact, the heating period extends throughout the year, with a winter design temperature of -19°C (**Table 2.2**). San Benedetto has a mild climate, with a winter design temperature of -1°C, while Milan is characterized by a design temperature of -5°C, and the heating system operates from October 15th to April 15th. Milan also has 2404 heating degree days, and according to Italian law (DPR 412/1993), it is classified as a municipality in "Zone E". This classification categorizes municipalities based on heating degree days, ranging from Zone A, where only 2 municipalities have fewer than 600 heating degree days, to Zone F. Milan's climate, however, represents a significant portion of Italian municipalities, as most of them fall into Zone E. Climate data for the three aforementioned municipalities are available on regional service websites: Arpa Lombardia [**5**] for Milan and Livigno and SIRMIP Marche [**6**] for San Benedetto del Tronto. In this analysis, due to data availability and quality, a focus is placed on 8 years (2013-2020). For all locations, external temperature, global radiation on a horizontal surface, and relative humidity data are obtained, as well as data on precipitation, wind direction, and speed for Livigno and Milan. Open data sources were utilized, through the Meteonorm software [**7**], to create climate files used as inputs for Trnsys. From the open data, the actual heating degree days (HDDs) value was derived for each location and year, considering a base temperature of 20°C, as depicted in Figure 2.4. The figure also includes HDD values for a Test Reference Year for Milan and S. Benedetto del Tronto.

It can be noticed that for all the three locations the HDDs varies significantly year by year, for example considering Milan, there is a minimum of the HDD for year 2014 (less that 2000 HDDs) and a maximum for year 2013 of about 2450, similar to the value of the TRY.

2.1.4. Dynamic analysis setup

The dynamic analyses conducted using Trnsys considered the same building in the three specified locations. Annual analyses were carried out, focusing exclusively on the heating season. In particular, the thermal demand satisfied by the heat pump (ET) and the electrical energy demand of the heat pump (EE) were determined for this season. Subsequently, the seasonal coefficient of performance (SCOP) value was calculated in various scenarios, defined as the ratio between ET and EE, considering values for the reference Test Reference Year (TRY) and for the eight years from 2013 to 2020. For these cases, a supply and return temperature from the heat pump of 45°C and 40°C, respectively, were assumed (which are typical temperatures for supplying the fan-coils).

Furthermore, the analyses were extended to all years and for the locations of San Benedetto del Tronto and Milan, considering a climatic compensation. This involved varying the heat pump's supply temperature based on the outdoor air temperature. Specifically, it was assumed that a supply temperature of 45°C would be maintained if the hourly outdoor air temperature was below 5°C, and a supply water temperature of 35°C would be used if the outdoor air temperature exceeded 15°C. In the temperature range of 5-15°C, the supply water temperature from the heat pump linearly varied from 45 to 35°C.

2.1.5. Results and discussion

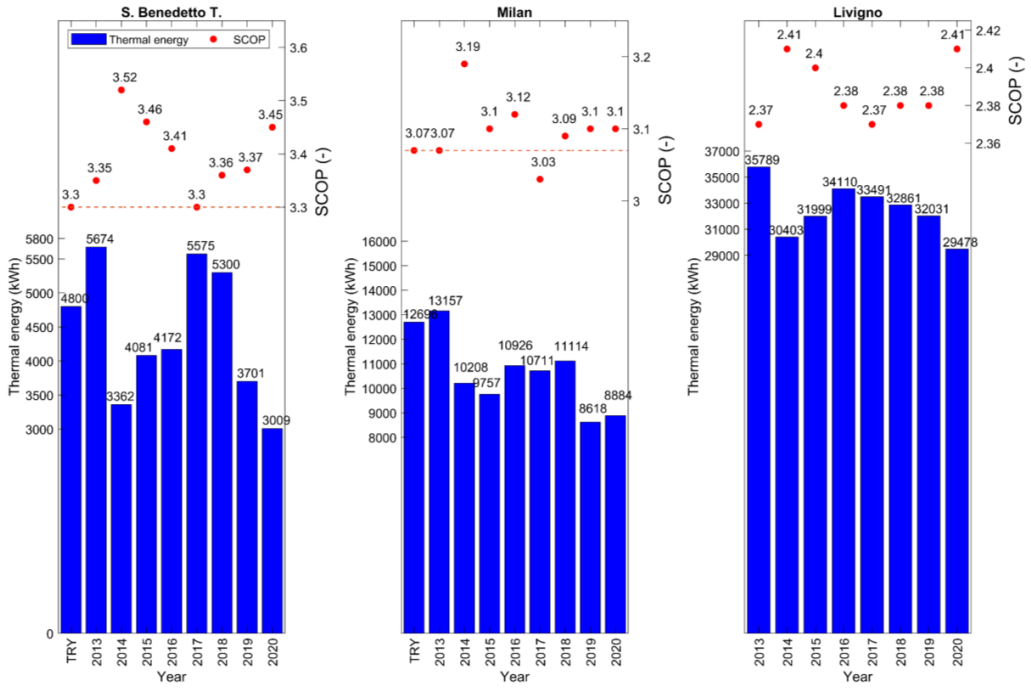

Figure 2.5 – Dynamic analysis results for the three municipalities considered.

Figure 2.5 presents the results obtained from the dynamic analysis considering the three locations. Specifically, the blue bars represent the thermal demand satisfied by the heat pump (ET) in kWh for the years 2013 to 2020, while the red dots indicate the SCOP values during the respective years. The dashed line represents the SCOP obtained in the case of the Test Reference Year (TRY) (which, as observed, is not available for Livigno). The results show that the variation in terms of thermal energy supplied by the heat pump varies significantly from year to year for all three locations. There is also year-to-year variation in SCOP, although this variation is relatively limited compared to what is observed for thermal energy. Additionally, SCOP tends to be higher than in cases considering the "standard" weather data provided by TRY.

Considering the results depicted in **Figure 2.5** and the HDDs shown in Figure 2.4, there is an absence of correlation between HDDs and SCOP, as well as between HDDs and thermal energy demand. Furthermore, there is not a strong correlation between SCOP and thermal energy. One possible explanation for the lack of correlation could be related to the number of hours during which the heat pump is active at specific outdoor air temperatures. In Figure 2.6, the number of hours when the outdoor air temperature falls within a range of $(tmean \pm 0.5)°C$ is reported for the years 2016 and 2017, referring to Milan. It can be observed that for several hours in 2017, the outdoor air temperature

is lower than 1°C. During these periods of lower outdoor air temperature, the heat pump's COP is lower than at higher outdoor air temperatures, which may have a significant impact on the SCOP, especially if is considered that lower outdoor temperatures usually result in a higher load demanded by the building.

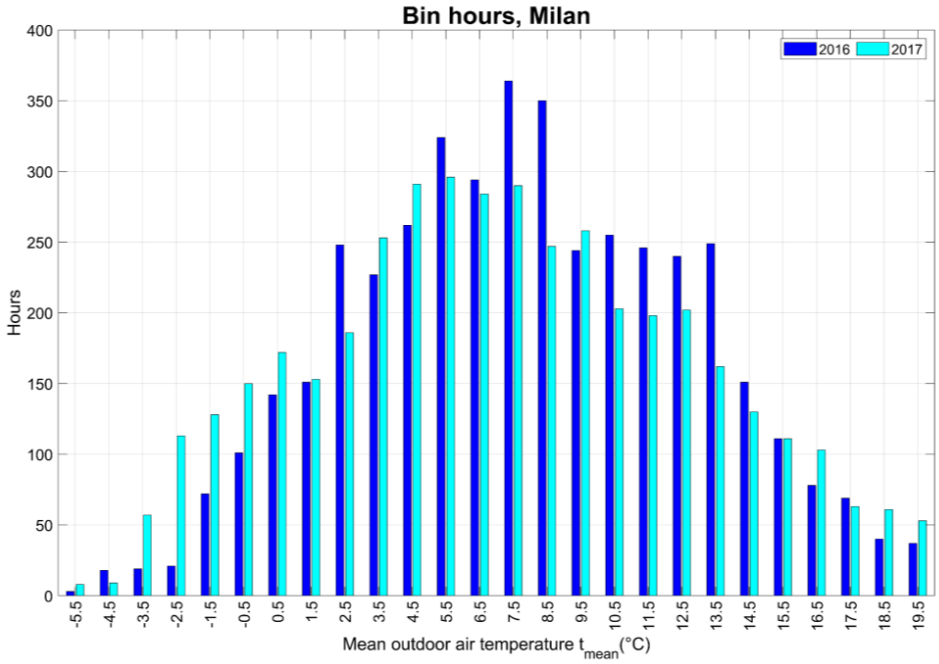

Figure 2.6 – Bin hours, Milan, years 2016 and 2017.

Finally, **Figure 2.7** presents a comparison between analyses that assume a fixed outlet water temperature from the heat pump (45°C) and the case where climatic compensation is considered. Only SCOP data is shown, as the influence of climatic compensation on the thermal demand satisfied by the heat pump is not appreciable. Some little differences in terms of SCOP can be observed, both for Milan and S. Benedetto del Tronto, especially for years characterized by higher outdoor air temperatures during the heating season.

The analysis has thus demonstrated that considering actual climatic data instead of typical climatic years for determining the performance of heat pumps in the considered cases has led to significant deviations in terms of thermal energy (up to 37%), but limited differences in SCOP (up to 7%). Furthermore, a possible correlation between SCOP/ET, between ET/HDDs and SCOP/HDDs has been excluded. Finally, the analysis considering climatic compensation has shown a slight increase in seasonal SCOP.

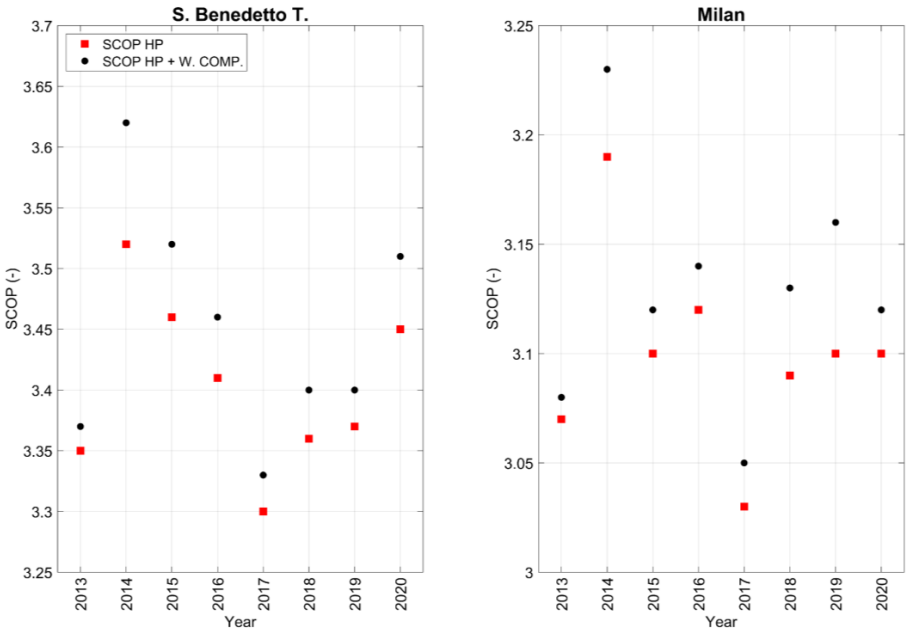

Figure 2.7 – SCOP for Milan and S. Benedetto del Tronto, with (black dots) and without (red squares) weather compensation.

2.2 Dynamic performance analysis considering the defrost effect

The analysis presented in the previous chapter does not account for the effects of defrosting on seasonal performance. As is well known, the performance of air heat pumps is significantly influenced by external climatic conditions. Specific temperature and humidity conditions can lead to ice formation on the external surface of the evaporator, subsequently reducing the machine's performance. This occurs mainly for two reasons: the ice formation limits the heat exchange between the refrigerant flowing in the evaporator and the external air, and the ice layer tends to obstruct the air's passage through the machine.

The frost build-up on the external evaporator is a dynamic phenomenon, which can be modelled in three phases, as proposed by Guo et al. [**8**]: the first phase sees a time-dependent growth; in the second phase, the growth of the ice layer decreases or stops; and in the last phase, there's a rapid increase in thickness. The formation and duration of these phases are influenced by the machine's operating conditions and especially by the specific conditions of the air passing through the evaporator. In this context, Zhu et al. [**9**] developed a map showing the ideal conditions for frosting based on external temperature and humidity. Frosting primarily occurs under high external relative humidity and temperatures above 0°C but still low. The maps by Zhu et al. define three potential frosting zones based on the severity of the phenomenon: severe, moderate, and mild frosting zones.

The frosting phenomenon related to air heat pumps was studied for several Italian locations by Vocale et al. [**10**]. The study focused on analysing the defrosting effect on machine performance across different Italian cities. Results showed that, for the same external air temperature, the main factor influencing the machine's necessary defrost cycles during the heating season, and ultimately its performance, was the external humidity of the location. However, this study used standard climatic data for its analysis. The analysis reported in this chapter, published in [**11**], considers real climatic data and pertains to the three previously analysed locations: S. Benedetto del Tronto, Milan, and Livigno.

2.2.1 Weather data

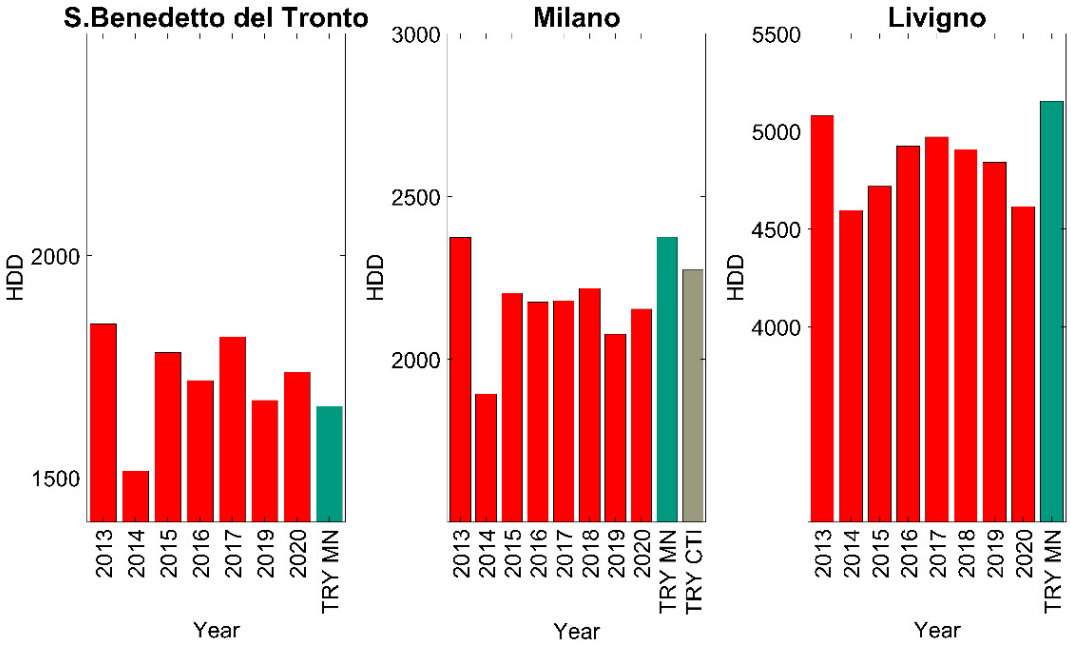

Figure 2.8 – HDDs for the three locations analysed and HDDs of the TRY from CTI and obtained from Meteonorm.

The climatic data used are the same as those presented in Section 2.1.3 and are again shown in **Figure 2.8**. Using the Meteonorm software, a TRY (Test Reference Year) was determined for Livigno. For Milan, the analyses also utilized a TRY defined by the CTI, the Italian Thermotechnical Committee [**12**]. As can be observed from **Figure 2.8**, the TRY tends to underestimate the Heating Degree Days (HDDs) for S. Benedetto del Tronto and overestimates the HDDs for Milan and Livigno. Additionally, the figure reveals significant variations in HDDs from one year to the next for all the towns under consideration. For instance, focusing on San Benedetto del Tronto, the maximum value is 1846 for the year 2013, and the minimum is 1515 for the year 2014. This corresponds to an increase of 11% and a decrease of 9% compared to the standard TRY value, respectively.

2.2.2 Building description

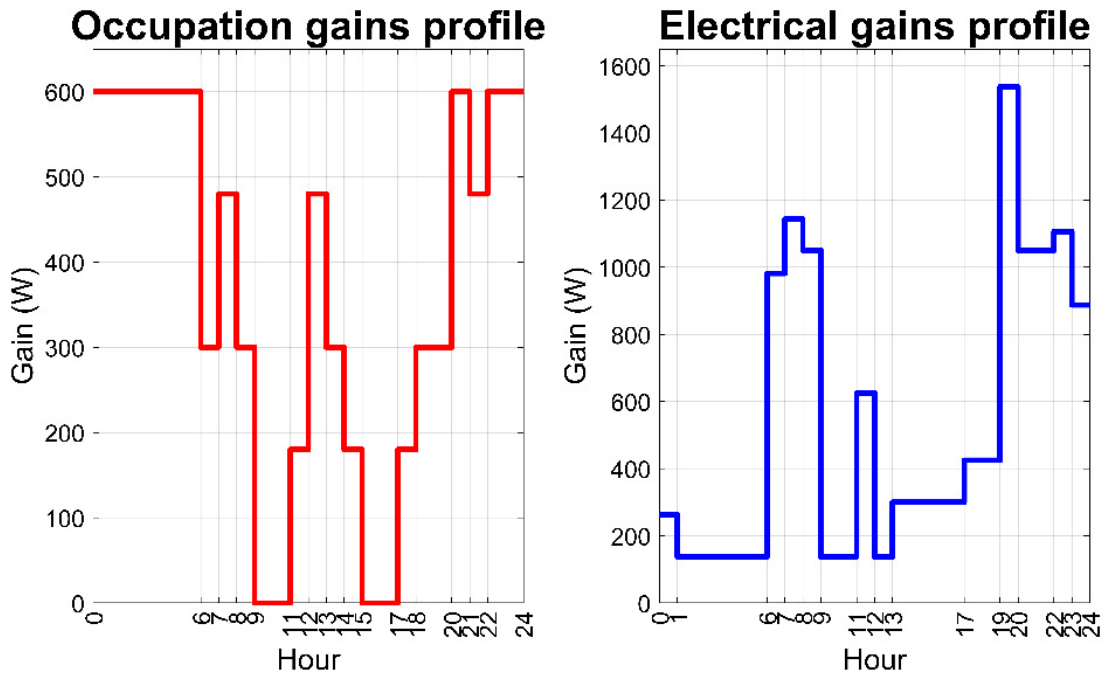

Figura 2.9 – Hourly gains due to inhabitants and to electric equipment

The building used in the dynamic analysis is the same as described in Section 2.1.1, in terms of geometry, intended use of the property, and thermophysical characteristics of the building envelope elements. Additionally, the overall transmittance of the windows is 1.5 W/(m^{2}K). They are of the 4-16-4 mm type with Argon gas in the cavity. Air exchanges are considered to be 0.3h^{-1}, and hourly occupancy profiles and internal contributions from equipment are shown in **Figure 2.9**. The contribution from the presence of people is quantified at 60 W, split between 20 W for internal convective gain and 40 W for radiative gain, as prescribed by the IEA Task 44 [**2**]. Given these conditions, the building has a peak thermal power for winter heating of 6.2 kW for S. Benedetto del Tronto, 7.9 kW for Milan, and 13.9 kW for Livigno, respectively (considering the respective design minimum external temperatures of -1°C, -5°C, and -19°C).

2.2.3 Heating system

The characteristics of the heat pumps considered are the same as indicated in the previous analysis and shown in **Figure 2.2**. The heat pumps were chosen to fully meet the winter thermal load under design conditions, in all three cases. The pairing between the heat pumps and the thermal demand of the building is shown in **Figure 2.10**. This figure displays the building signature, considering a thermal demand of the building that

decreases linearly with the increase in the dry bulb temperature of the external air (represented by the black line), and the power supplied by the three heat pumps at maximum frequency, relative to the different external air temperatures.

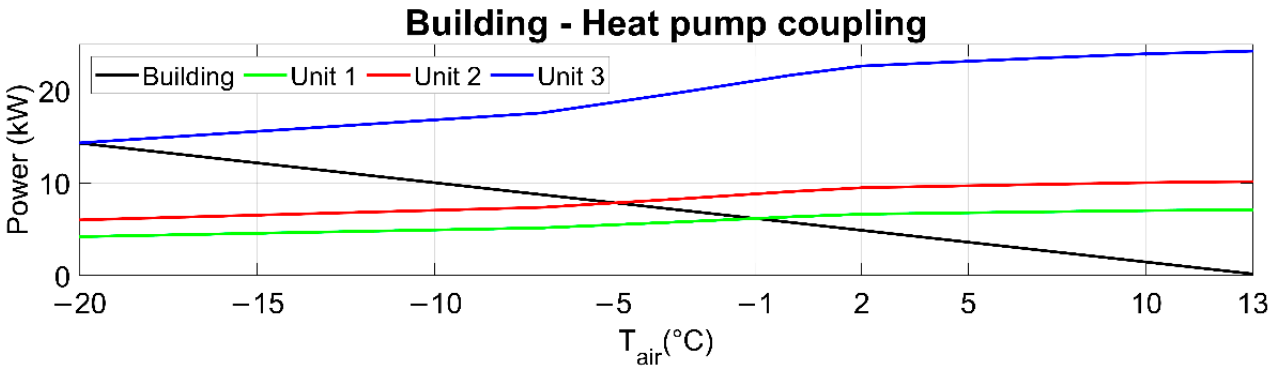

Figure 2.10 – Building signature and thermal power delivered by the three heat pumps at maximum inverter frequency.

The layout is the one proposed in **Figure 2.3** and presents the same characteristics and technical feature described in section 2.1.2.

2.2.4 Heating system

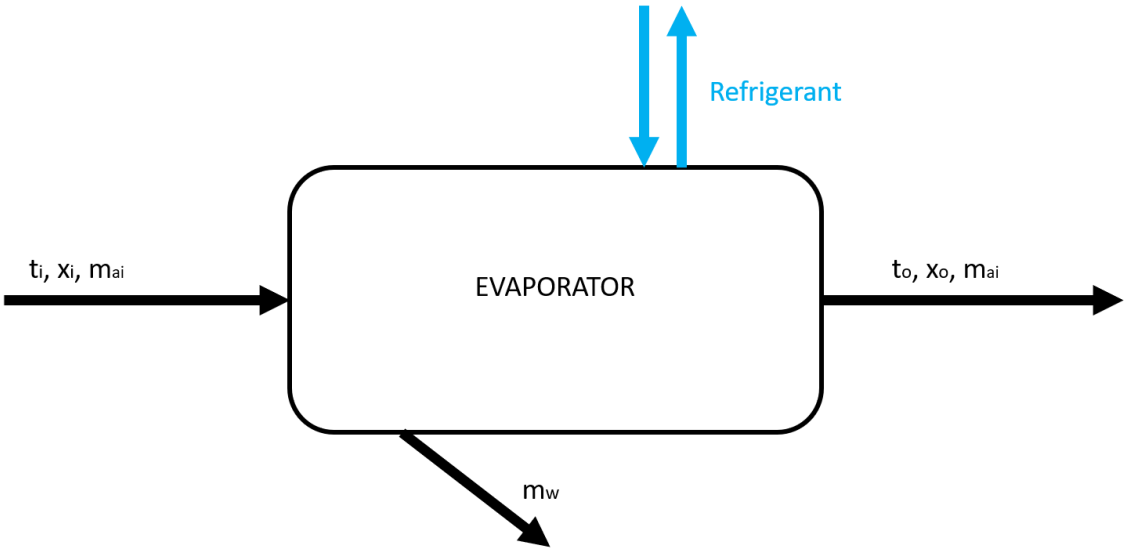

Figure 2.11 – Evaporator of the heat pump considered as a black box; m_w represents the water condensate on the evaporator.

Among the various possible methods to defrost the machine's evaporator, the RCD (reverse cycle defrosting) was considered, which is a known method that involves reversing the machine's cycle. During an RCD cycle, the compressor of the heat pump is activated, reversing the cycle through the 4-way valve, so that the evaporator becomes the condenser and vice versa, the condenser becomes the evaporator. In this way, the heat extracted from the internal environment (or from the machine's load) is used to heat the evaporator and melt the ice deposited on it. In literature, the effect of defrost has been analysed (see e.g. [**9, 13- 14**]), and different control logics can be adopted to manage the RCD cycle performed by the machine. In this analysis, it was decided to consider defrost cycles of constant duration, equal to 5 minutes, with constant electrical power absorbed by the heat pump throughout the entire RCD cycle. A simple model to determine when defrosting was necessary was introduced, and the machine's evaporator was schematized as a black box (an open thermodynamic system) represented in **Figure 2.11**. The introduced model requires knowledge of the following quantities at the evaporator's inlet: air mass (m_{ai}), air temperature (t_i), and air title (x_i); it is possible to derive the enthalpy h_i through the approximate psychrometric formula:

$$h_i = 1.006\, t_i + x_i(2501 + 1.84 t_i) \tag{1}$$

And also the dew point temperature t_{DP}, which is the temperature at which, given the input conditions, water would start to condense on the coil:

$$t_{DP} = \frac{4030.183}{16.6536 - \ln\left(\frac{P_{sat}}{1000}\right)} \tag{2}$$

$$P_{sat} = 1000 \cdot \exp\left(16.6536 - \frac{4030.183}{235 + t_i}\right) \tag{3}$$

Using formula (4) (where P_{tot} (Pa) indicates atmospheric pressure), it is also possible to determine the title under saturation conditions and subsequently the enthalpy at the dew point h_{DP} (5):

$$x_{DP} = 0.622 \frac{P_{sat}}{P_{tot} - P_{sat}} \tag{4}$$

$$h_{DP} = 1.006\, t_{DP} + x_{DP}(2501 + 1.84 t_{DP}) \tag{5}$$

Knowing the thermal power extracted from the evaporator Q_{evap} (kW) (formula (6), in which P_{th} is the thermal power output of the heat pump) of the machine, using formula (7) it is possible to obtain the value of the air enthalpy at the exit from the evaporator:

$$Q_{evap} = P_{th}\left(1 - \frac{1}{COP}\right) \tag{6}$$

$$h_o = h_i - \frac{Q_{evap}}{m_{ai}}. \quad (7)$$

By comparing the specific enthalpy value h_o (kJ/kg) of the outgoing stream with the enthalpy that would be present under dew point conditions h_{DP}, it can be determined if ice formation is possible. If it is observed that the enthalpy at the exit is lower than the dew point enthalpy for a continuous period of about 50 minutes, the defrost cycle begins.

This simple defrost cycle has the advantage that it can be easily implemented in Trnsys, and its implementation does not require additional technical information beyond what is typically provided on the heat pump's datasheet (COP curves, thermal power, and airflow processed by the evaporator fan).

In [**15**], Dongellini et al. simulated the RCD using time-dependent functions for electric and thermal power during the defrosting phase. Specifically, the thermal power trend is modeled with two parabolic branches, while the electric power is modeled with two linear functions.

An analysis as reported in [**15**] can only be conducted if a vast amount of data is available from the manufacturer or if long-term experiments are performed on a specific heat pump. For the heat pumps investigated here, the electric power input $P_{el,D}$ (kW) of the heat pump and the thermal power provided to the evaporator during the RCD cycle $P_{th,D}$ (kW) are considered constant and listed in **Table 2.5**.

Table 2.5 – Constant thermal and electric power of the heat pump during the defrost cycles.

Heat pump	$P_{th,D}$ **(kW)**	$P_{el,D}$ **(kW)**
Unit 1	4.6	1.2
Unit 2	5.7	1.7
Unit 3	15.7	4

2.2.4 Dynamic analysis results

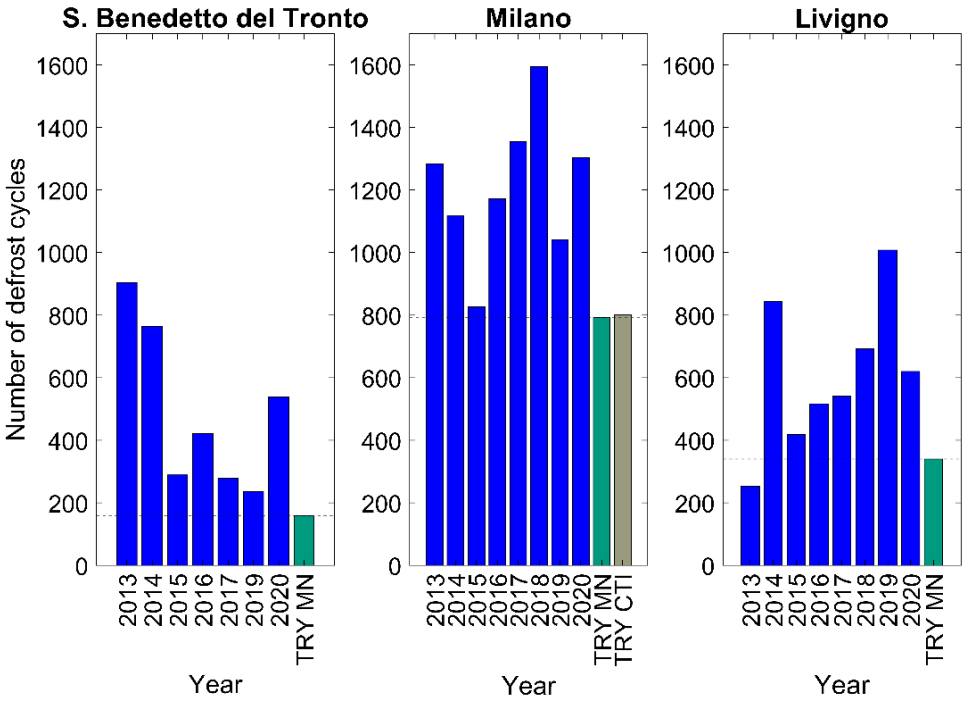

Figure 2.12 – Number of RCD cycles performed by the three heat pumps.

Annual simulations were conducted to determine the performance of the 3 heat pumps, considering different climatic data (real for the period from 2013 to 2020) and those determined by the test reference year. Analyses were carried out for each year, both considering and not considering the defrost cycles. All dynamic simulations were performed using the Trnsys software, and the simulation time-step is fixed at 30 seconds. For each simulation year, the electrical energy used for the defrost cycles and the total number of defrost cycles were also determined. **Figure 2.12** graphically displays the number of defrost cycles carried out by the heat pumps in the different climates considered. There is a significant variability in the number of defrost cycles from year to year for each location (the maximum and minimum numbers are also listed in **Table 2.6**).

Table 2.6 – Minimum and maximum number of defrost cycles for the three heat pumps.

Heat pump and location	TRY	Minimum	Maximum
Unit 1 (S. Benedetto del Tronto)	158	235	904
Unit 2 (Milan)	802	827	1595
Unit 3 (Livigno)	340	254	1008

From the data reported in the previous table, it is observed that the Test Reference Year tends to underestimate the number of defrosting cycles required for all 3 locations. It can also be seen that the number of defrosting cycles required in Milan is generally higher than the number required in Livigno. This is because frosting occurs if the air humidity is sufficiently high. In contrast, a very cold climate like Livigno's has a lower amount of water vapor in the air compared to a climate like Milan's, typical of the Po Valley. This climate is generally characterized by temperatures above 0°C but with a higher content of water vapor in the air.

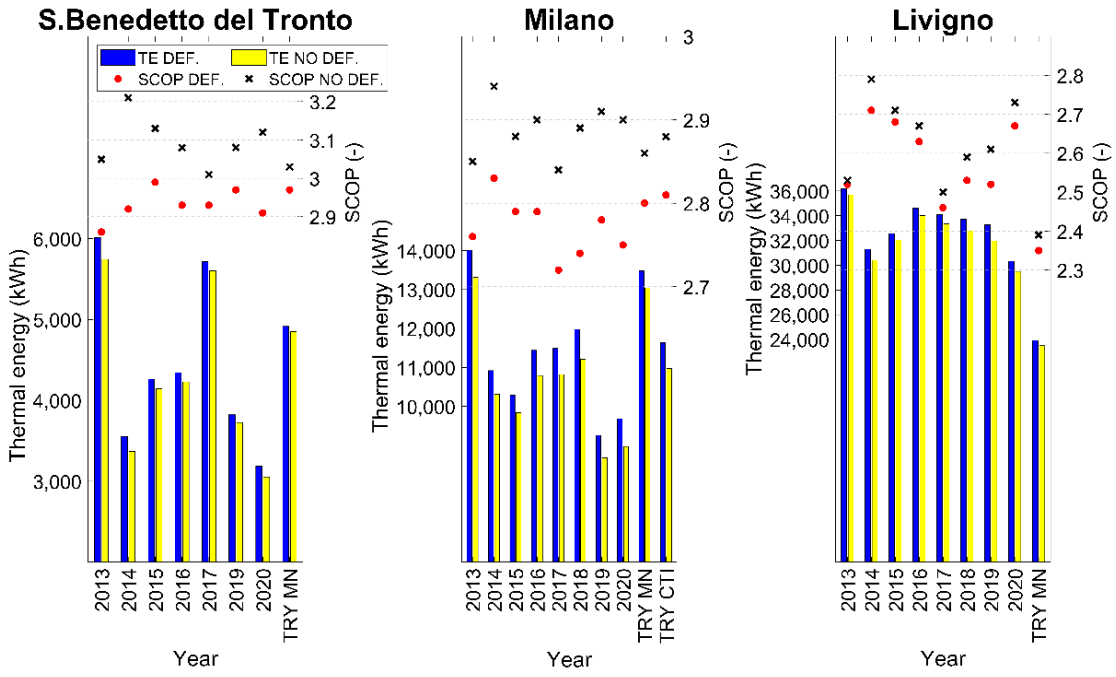

Figure 2.13 – Thermal energy supplied by the heat pump to the building with and without defrost (blue e yellow lines respectively); SCOP considering defrost (red dots) and neglecting defrost cycles (black crosses).

In **Figure 2.13**, the results obtained from the simulations are shown, considering and not considering the defrost cycles, in terms of thermal energy provided by the heat pump to the building and the seasonal performance coefficient of the heat pump for the heating season. It is observed that the thermal energy provided by the heat pump to the building is always greater when the defrost cycles are considered. This is because the thermal power provided to the evaporator during the defrost cycle is the sum of the thermal energy subtracted from the hot storage and the power supplied to the compressor; however, when the cycle is reversed and the machine operates normally,

it will also supply the hot storage with the thermal energy subtracted during the defrost cycle. It is also visually noticeable that in all cases where the effect of defrost is considered, the SCOP is lower.

In Milan, there's a notable yearly fluctuation in thermal energy demand. For 2019, the demand ranged from 8,676 kWh (without defrost) to 9,257 kWh (with defrost). In 2013, it was between 13,316 kWh and 14,009 kWh. The SCOP value shows minor fluctuations, less pronounced than in San Benedetto del Tronto, where the SCOP ranged from 2.72–2.94 depending on defrost consideration. Livigno also displayed significant yearly variations in thermal energy from the heat pump, with ranges from 29,496 kWh to 36,183 kWh. **Figure 2.13** indicates that the Meteonorm TRY for Livigno underestimates both thermal energy demand and SCOP. Conversely, for Milan, it tends to overestimate thermal energy, but SCOP values align with real weather data. Notably, CTI TRY appears more accurate for Milan than Meteonorm. Another observation from **Figure 2.13** is the increased thermal energy demand when considering defrost. Milan's demand can surge by up to 7.9% (in 2020), more than San Benedetto del Tronto's 5.5% (in 2014) and Livigno's 4% (in 2019). This aligns with findings from other studies [**10**], highlighting the impact of defrost cycles on heat pump SCOP. **Figure 2.14** presents the electrical energy used by heat pumps across all simulations. It reveals that the energy consumption increase due to defrost is highest in Milan (average of 10.7%), followed by San Benedetto del Tronto (9.5%) and then Livigno (4.6%).

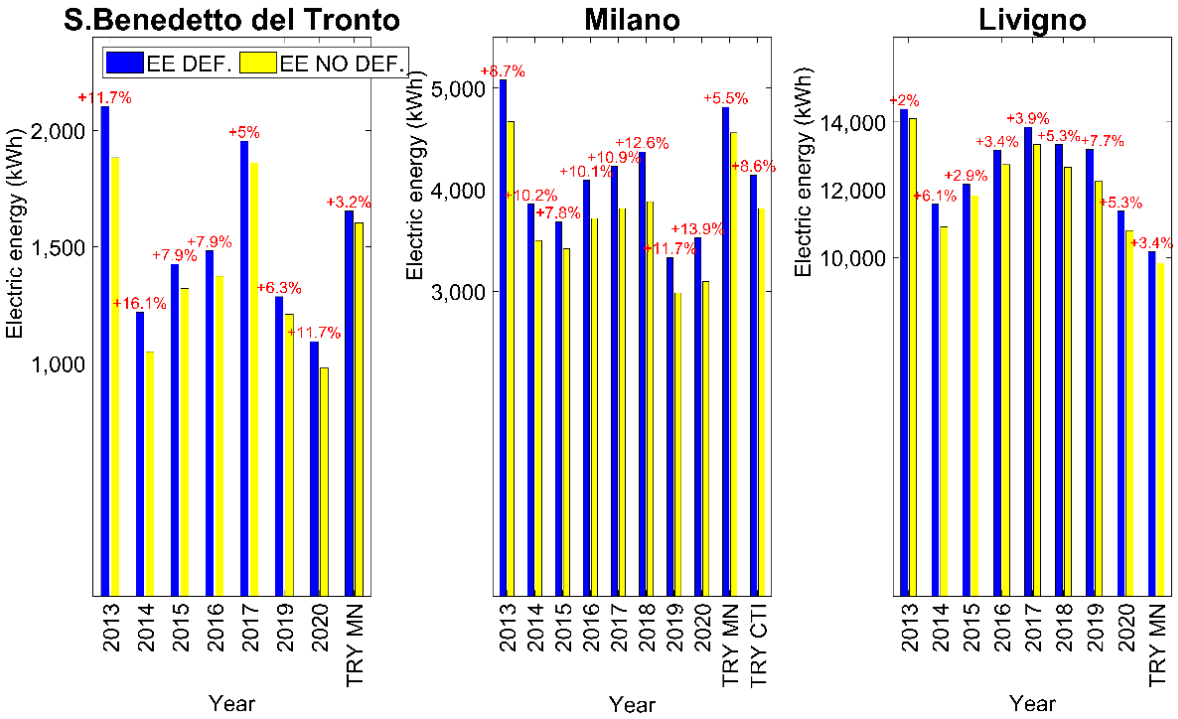

Figure 2.14 – Electricity demand considering and neglecting defrost (blue and yellow bar respectively) and percentage increase in defrost case.

The main findings of this analysis are the following:

- Correct evaluation of defrosting cycles is crucial for determining the Seasonal Coefficient of Performance (SCOP) of Air-Source Heat Pumps (ASHPs).
- Dynamic simulations revealed that while thermal energy demand can vary significantly across different years and locations, the effective SCOP remains relatively consistent, with notable variations observed for Livigno.
- Frost build-up on the external heat exchanger of ASHPs during winter can degrade the unit's performance due to reduced heat transfer efficiency.
- Real climate data, as opposed to standard Test Reference Year (TRY) data, is essential for accurately evaluating the occurrence of defrosting cycles in ASHPs.
- Variations in Heating Degree Days (HDD) across different years and locations, such as the differences observed for San Benedetto del Tronto between 2013 and 2014, highlight the importance of considering real climate data.

2.3 Experimental analyses conducted in the Technical Physics Laboratory at the University of Bologna on a dual – source heat pump

In Sections 2.1 and 2.2, analyses conducted using dynamic simulation software were presented. In this chapter, experimental analyses carried out at the Technical Physics Laboratory of the University of Bologna will be introduced, to determine the performance of the heat pumps. The experimental apparatus used in the laboratory for the tests will also be presented. The heat pump tested is a dual-source heat pump, i.e., a machine that can use both the ground and the air as a thermal source from which heat is drawn. The results of performance analysis according to international standards have been published also in [**16**].

2.3.1 Experimental test ring

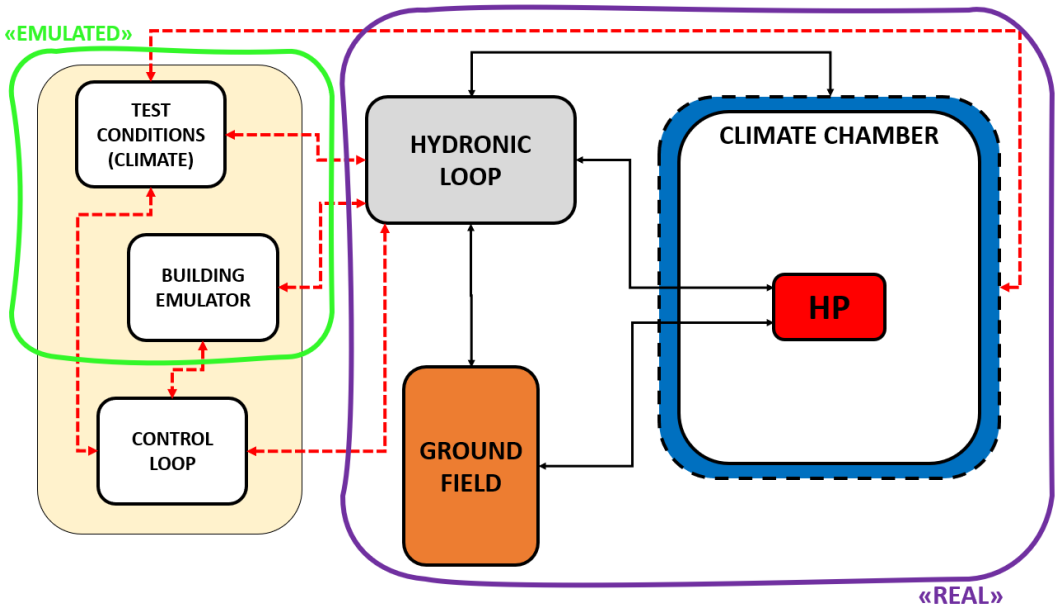

Figure 2.15 – Hardware-in-the-loop approach.

The test facility located within the laboratory was specifically designed and built to experimentally assess the energy performance of various heat pump types under dynamic operating conditions. Given that in-situ monitoring of heat pump systems in occupied residential and commercial buildings can be costly and requires strict permissions from the occupants, the test bench discussed in this article serves as an optimal solution for evaluating the real-world behavior of such systems. Indeed, establishing lab-based testing facilities is crucial for both industry and academic entities to gather trustworthy data. The test setup has been designed to control the heat pump under test using a "Hardware-in-the-Loop" (HiL) method [**17-20**]. The HiL approach is

an advanced and precise technique for analyzing the performance of heat pumps when integrated with buildings.

The hardware-in-the-loop (HiL) approach (**Figure 2.15**) employs a unique hybrid method for analyzing the performance of heat pumps. This hybrid methodology combines experimental and dynamic simulation techniques. Using dynamic simulation software (i.e. building emulator), one can determine the building's temporal thermal demand profile. The derived thermal demand data can then be relayed to the test system, translating into different water temperatures and potentially flow rates at the heat pump's inlet. This methodology enables an in-depth study of the machine's performance in conditions closely mirroring real-world scenarios. Furthermore, if the pump is positioned inside a climate chamber (a defined space where specific temperature and humidity levels can be achieved) it is feasible to vary the chamber's conditions, thereby emulating the external environmental conditions the heat pump's external unit would face in real-world operations. The essence of the HiL approach is its capacity to experimentally analyze systems, which might be overly intricate for complete laboratory replication, by leveraging this 'hybrid' strategy of both experimental and dynamic simulation methods.

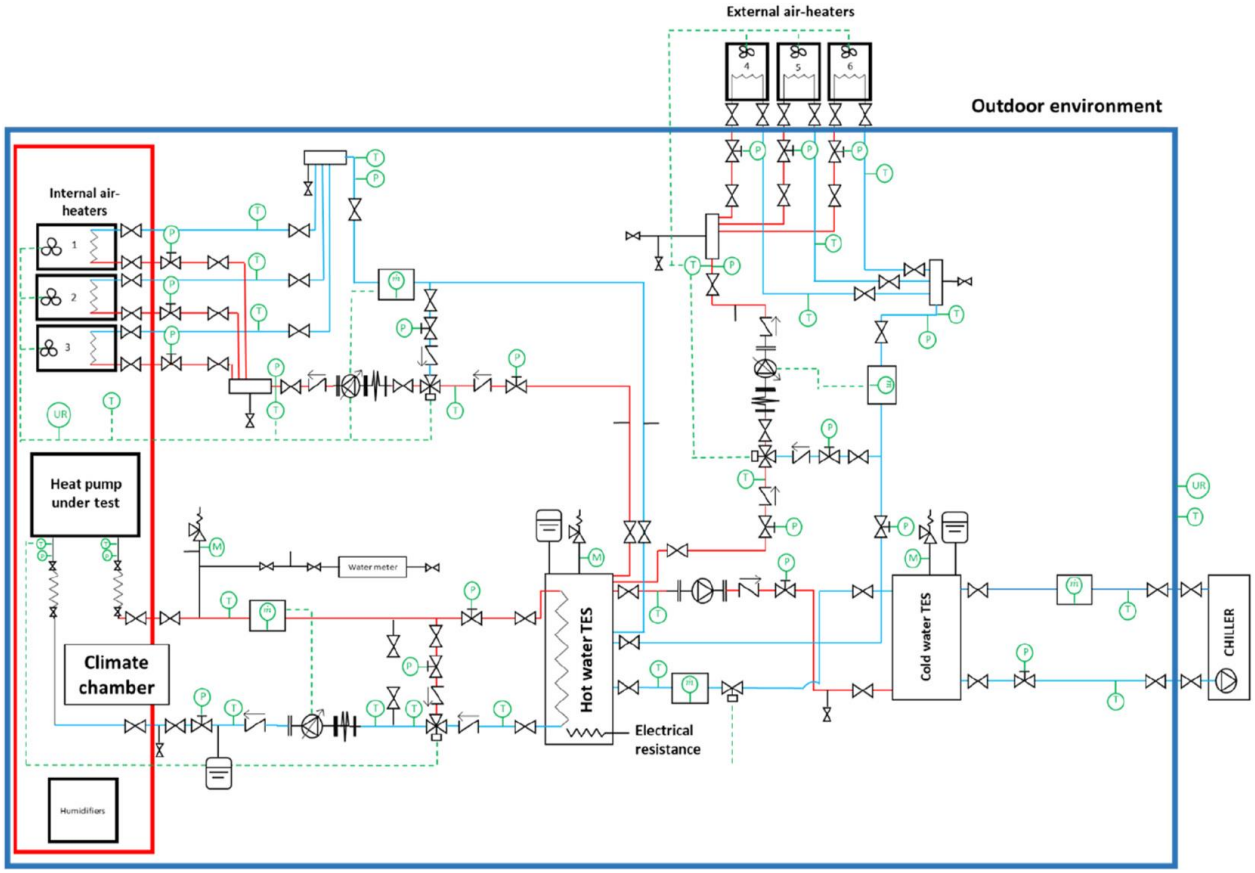

Figure 2.16 – Hardware-in-the-loop approach.

The experimental test rig is composed of a climate chamber, a building emulator and a hydronic loop, coupled to a borehole heat exchanger field; the hydronic loop is presented in **Figure 2.16** (In this figure the ground field loop scheme is not reported).

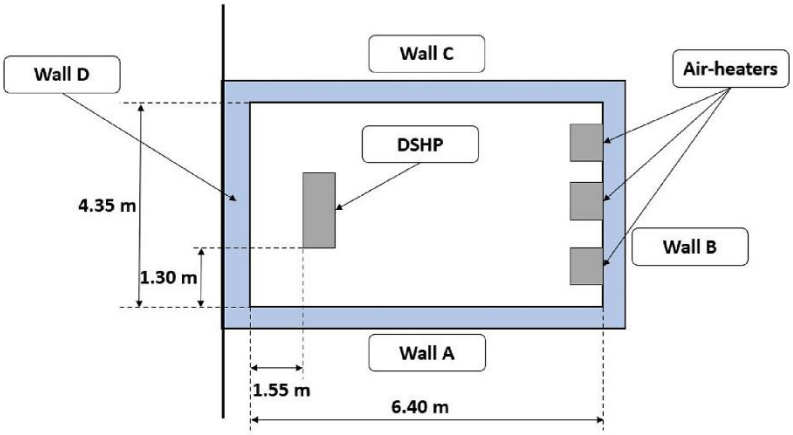

Figure 2.17 – Layout of the climate chamber; DSHP (Dual – source heat pump) refers to the heat pump placed in the climate chamber and under test.

The climate chamber encompasses an internal net volume of 78 m^3, with measurements of 6.40 m in length, 4.35 m in width, and 2.80 m in height, resulting in a net floor area of 27.8 m^2. **Figure 2.17** provides a streamlined layout of the climate chamber. The side walls and ceiling feature robust insulation, utilizing a 0.30 m of polystyrene layer, minimizing heat transfer with neighbouring areas (boasting a U-value for the vertical walls around 0.1 $W/(m^2K)$). Only one wall, denoted as 'Wall D' in **Figure 2.17**, is exposed to the external environment. The remaining three walls, along with the ceiling, border other internal sections of the laboratory, and the floor rests directly on the ground. The ceiling's U-value mirrors that of the vertical walls, whereas the floor's transmittance is approximately 2.3 $W/(m^2K)$. Within the chamber, three distinct air-heaters, labeled as components 1, 2, and 3 in **Figure 2.16**, are strategically placed. These air-heaters vary in their heating capacities and are each fitted with an inverter-driven fan, handling air flow rates from 150 up to 12,100 m^3/h.

The climate chamber serves as a pivotal platform, meticulously designed with its core application centered around probing the intricate dynamics of heat pumps under varied operational conditions. This specificity underscores the importance of strict ambient control, especially during tests involving an Air Source Heat Pump (ASHP). As such, a

synergistic blend of air heaters and humidifiers are employed to ensure this equilibrium. Interestingly, when an ASHP is propelled into its heating phase, a noticeable dip in the chamber's air temperature ensues, a consequence of the refrigerant fluid's evaporation. This presents a unique challenge, one that's adeptly managed by harnessing the heat emanating from the heat pump's condenser. The resultant hot water powers the internal air heaters, which are seamlessly integrated into the hydronic loop, a system vividly detailed in **Figure 2.16**. This equilibrium between the heat absorbed and reintroduced ensures optimal air temperature control, further fine-tuned by modulating the fan speeds of the air heaters. To enhance stability and enhance operational consistency, the system is fortified with a water thermal energy storage (TES) tank, prominently depicted as the 'hot water TES' in **Figure 2.16**.

Figure 2.18 – View of the test ring inside the laboratory.

This tank, with its voluminous 0.5 m^3 capacity as showcased in **Figure 2.18**, utilizes the hot water from the heat pump. The water courses through a coiled heat exchanger submerged within the tank. With a sprawling external surface of 6 m^2 and an impressive length of 60 m, this heat exchanger stands out. Furthermore, the tank houses an electric resistance with a robust heating capacity of 6 kW, stepping in when the heat output from the pump falls short, ensuring the chamber's temperature remains consistent. This resistance proves invaluable, especially during system warm-ups and other nuanced operational phases. The design is so intricate that during instances necessitating a temperature drop within the chamber, the fan speeds of the internal air-heaters are

dialed down. Subsequently, the heat from the tested pump is vented out, by means of three external air-heaters, labeled as components 4, 5, and 6 in **Figure 2.26**.

Figure 2.19 – View of the test three air -heaters placed inside the climatic chamber.

Table 2.7 – Technical data about the six air – heaters present in the test ring.

Air heater	**Rated heating capacity (kW)**	**Maximum absorbed power (kW)**	**Location**
Air – heater 1	11.2	0.08	Climate chamber
Air – heater 2	18.7	0.14	Climate chamber
Air – heater 3	67.0	0.84	Climate chamber
Air – heater 4	11.2	0.08	Outside
Air – heater 5	18.7	0.14	Outside
Air – heater 6	67.0	0.84	Outside

In **Table 2.7** technical information about the three air – heaters installed inside the climate chamber (**Figure 2.19**) and related to the ones placed outside the laboratory are reported. Occasionally, when external ambient conditions prove challenging, the system deftly activates an air-to-water inverter-driven chiller. This unit is tethered to another 0.5 m³ thermal energy storage tank, known as the 'cold water TES' in **Figure 2.16**. This secondary tank ensures system steadiness, even during the chiller's sporadic on-off sequences. Notably, the chiller, a product of Galletti, boasts a nominal power of 18.2 kW under stipulated conditions, specifically when outdoor temperatures peak at 35°C and water temperatures oscillate between 12°C (inlet) and 7°C (outlet). Temperature sensors and state-of-the-art electromagnetic flow meters (Siemens, SITRANS F M MAG 1100) monitor system operations, ensuring optimal performance of the tested heat pump. Supplementing this is a power meter (Fluke 1735 three-phase

power quality logger) installed in the laboratory, tasked with analyzing the electric power input of the heat pump undergoing tests. Moreover, T-type thermocouples and calibrated RTD Pt100 sensors are placed within the test bench. Moreover, when the system tests a ground-coupled heat pump or a DSHP in ground mode, there is no need to control the conditions inside the climate chamber. In **Figure 2.20** is shown the borehole field, composed of 4 vertical heat exchangers of different depths, which is placed next to the laboratory.

This setup offers flexibility, allowing different combinations of borehole lengths to study the impact of borehole field sizes on pump performance. Lastly, enhancing there is a Distributed Temperature Sensing (DTS) system embedded within the borehole field. This system, utilizing fiber optic cables, provides real-time insights into fluid thermal progression along different boreholes. Two such boreholes, one spanning 100 m and the other 60 m, present these optical fibers, capturing the dynamic fluid temperature variations during ground-source mode tests.

Figure 2.20 – View of the top of the borehole heat exchanges installed outside the laboratory.

2.3.2 Tests on the dual – source heat pump in air-source mode

(**a**) (**b**)

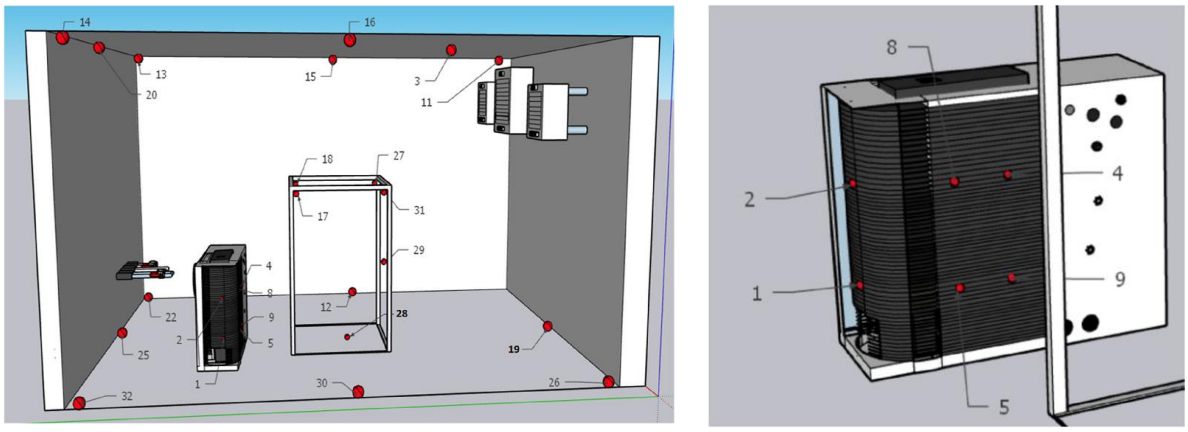

Figure 2.21 – Position of temperature sensors inside the climate chamber (**a**) and in proximity of the evaporator (**b**).

Tests were conducted on a dual-source heat pump operating in air-source mode to obtain data on machine performance, specifically focusing on the thermal power output and the Coefficient of Performance (COP). These evaluations adhered to the European standard UNI EN 14511-3 [**21**]. Alongside these primary tests, data related to the climate chamber's temperature distribution was also collected. For accurate temperature readings, several T-type thermocouples were strategically placed within the chamber, as depicted in **Figure 2.21**. However, for evaluations in line with the [**21**] standard, readings from thermocouples 1, 2, 4, 5, 8, and 9 were considered essential. These particular thermocouples are situated close to the evaporator of the heat pump under test. Data from the remaining thermocouples, while not directly influencing the test outcomes, provides insight into the chamber's temperature distribution.

The heat pump, illustrated in **Figure 2.22**, is a prototype of an air-source variant. It features an inverter-driven compressor and utilizes the R-410A refrigerant. The pump's nominal thermal power is rated at 11.4 kW, measured under specific conditions: an air-dry bulb temperature of 7°C, wet bulb temperature of 6°C, and water temperatures from an inlet of 40°C to an outlet of 45°C. As prescribed by the [**21**] standard, the heat pump's heating capacity (P_{th}) on the water side is deduced by measuring the water temperature difference (ΔT) and assessing the water mass flow rate ($\dot{m}$) at the pump's condenser:

$$P_{th} = \dot{m} c_p \Delta T \tag{8}$$

where in Eq. (8), c_p is the specific heat capacity at constant pressure of the water flowing in the condenser, assumed constant during tests (4186 J/(kgK)). Water temperature measurements have been collected employing RTD sensors at the inlet and outlet of the machine, while the mass flow rate sensor is placed between the heat pump and the hot thermal storage.

Figure 2.22 – DSHP under investigation placed inside the climate chamber.

The standard prescribes the test procedure, the specifications of the climate room and the admitted tolerances of the measuring equipment. An important aspect related to the climate chamber refers to the internal air flow distribution. The heat pump must be located away from the walls, with a minimum distance of 1 m, the air speed must be lower than 1.5 m/s and the air-heaters must not be placed close to the temperature sensors. The allowed measure uncertainties are specified in **Table 2.8**.

Table 2.8 – Maximum uncertainties admitted as prescribed by European standard.

Quantity	**Maximum uncertainty**
Air dry bulb temperature	± 0.20 K
Electric power	± 1 %
Liquid inlet/outlet temperature	± 0.15 K

Liquid volume flow	± 1 %

The testing protocol requires a minimum of four air temperature measuring points, positioned strategically close to the evaporator of the heat pump under examination. These sensors should be within a distance of 0.25 m from the evaporator and be evenly distributed. Steady-state condition tests ran for a duration of 70 minutes, with data being collected at intervals of every 30 seconds. To ensure the conditions remain stationary during testing, the procedure as outlined in the standard mandates that temperature readings have minimal fluctuations throughout the test. The specific amplitude of acceptable fluctuations is detailed in **Table 2.9**. Delving further into the specifics, the standard sets two distinct benchmarks: Firstly, individual measurements must fall within a defined range. Secondly, the average fluctuation across the test's duration should not exceed the average limit presented in **Table 2.9**.

Table 2.9 – Admitted fluctuation during tests according to European standard.

	Mean	**Punctual**
Air dry bulb temperature	± 0.3 K	± 1.0 K
Inlet water temperature	± 0.2 K	± 0.5 K
Outlet water temperature	± 0.6 K	± 0.3 K

In addition, the standard prescribes to determine the temperature difference between the water outlet and inlet of the heat pump every 5 min during the test. The mean temperature differences, measured every 5 min as well, are employed to determine the percentage temperature difference with respect to the first mean temperature difference, using Eq. (9), where ΔT_0 refers to the mean value of the first 5 min and $\Delta T_i(\tau)$ refers to the mean temperature difference of the following intervals of the entire test,

$$\Delta T_{i,\%} = 100 \cdot \frac{\Delta T_0 - \Delta T_i(\tau)}{\Delta T_0} \tag{9}$$

EN 14511-3 mandates that the percentage temperature disparities, $\Delta T_{i,\%}$, should not exceed 2.5%. Two evaluations were conducted on the ASHP to assess the heat pump's efficiency, specifically its heating capacity and *COP* under full load conditions. For the first evaluation, the water flowed in at 30°C and out at 35°C, with the air's dry bulb temperature being 7°C. In the second test, the air temperature was 12°C, and the water

had an inlet/outlet temperature of 40°C/45°C, respectively. During both tests, the standards set by the norm were adhered to. **Table 2.10** showcases the results, comparing the *COP* and heat pump's thermal output to the manufacturer's provided data. The data reveals that the heat pump's experimental performance is slightly below the manufacturer's claims. However, considering typical uncertainty values, these results remain within an acceptable range. It's important to mention that often, manufacturers do not specify the accuracy range for the primary parameters listed in their datasheets.

Table 2.10 – Performance values declared by manufacturer and obtained during tests.

	Test 1		**Test 2**	
	Experimental	**Declared**	**Experimental**	**Declared**
COP (-)	3.48 ± 0.52	3.98	3.16 ± 0.46	3.55
P_{th} (kW)	10.75 ± 1.37	11.3	11.66 ± 1.45	12.3

2.3.3 CFD analysis of the temperature and velocity inside the climate chamber

(**a**) (**b**)

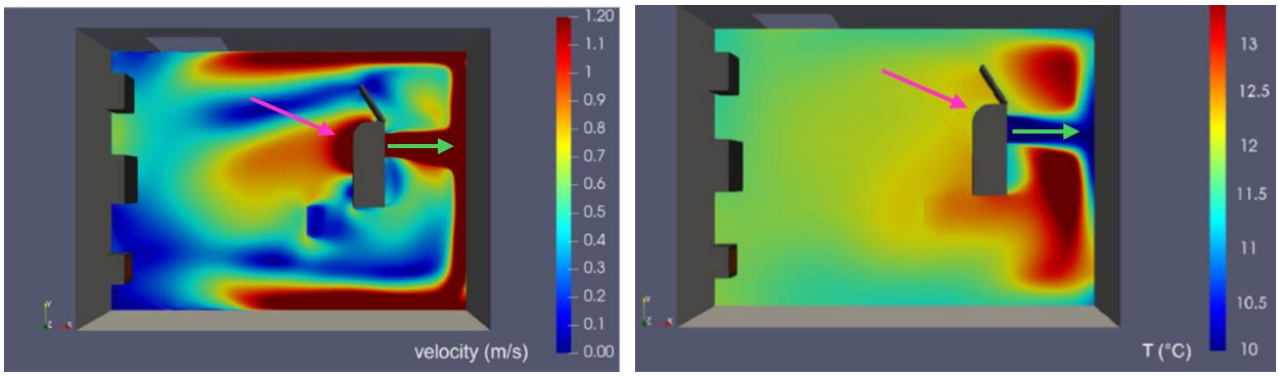

Figure 2.223 – Air velocity (**a**) and temperature (**b**) at z = 1 m inside the climate chamber obtained by CFD analysis. The pink and green arrows represents the evaporator inlet and outlet respectively.

A CFD analysis was also conducted to determine the proper positioning of the heat pump during the test phase in the climatic chamber. This was done to comply with the standards regarding the maximum velocity entering the evaporator and the uniformity of the temperature entering the evaporator. The analysis was performed using the STAR-CCM+ software, and the main results in terms of air velocity and temperature are shown in **Figure 2.23**. From the figure, it can be seen that at a height of 1 m from the floor,

the air velocity entering the machine remains below 1.5 m/s, and the temperature entering the evaporator is uniform. The temperature data also aligns with those obtained from thermocouples placed at various points in the climatic chamber. It was observed that the lower temperatures are found between the heat pump and the rear wall, close to the machine's evaporator outlet during testing. In contrast, higher temperatures were observed near the heaters' outlet and on the sides of the evaporator exit (**Figure 2.23b**).

2.3.4 Discussion of the results and procedure

The analyses presented in the previous sections have demonstrated the feasibility of using the HiL approach to experimentally determine the performance of a heat pump. Specifically, the performance was determined according to European standards, and the results obtained are consistent with those declared by the manufacturer when considering the uncertainty ranges related to the measurements made.

References

[1]: Ballerini, V.; Dongellini, M.; Schio, E.R. di; Valdiserri, P. Effect of Real Temperature Data on the Seasonal Coefficient of Performance of Air Source Heat Pumps. *J. Phys.: Conf. Ser.* **2022**, *2177*, 012025, doi:10.1088/1742-6596/2177/1/012025.

[2]: Dott, R.; Haller, M.; Ruschenburg, J.; Ochs, F.; Bony, J. IEA-SHC Task 44 Subtask C Technical Report: The Reference Framework for System Simulations of the IEA SHC Task 44/HPP Annex 38: Part B: Buildings and Space Heat Load. IEA-SHC.; 2013

[3]: Klein, S.A.; Duffie, A.J.; Mitchell, J.C.; Kummer, J.P.; Thornton, J.W.; Bradley, D.E.; Arias, D.A.; Beckman, W.A.;Braun, J.E.; et al. ; TRNSYS 17: A Transient System Simulation Program; University of Wisconsin: Madison, WI, USA, 2010

[4]: Klein, S.A.; Duffie, A.J.; Mitchell, J.C.; Kummer, J.P.; Thornton, J.W.; Bradley, D.E.; Arias, D.A.; Beckman, W.A.; TRNSYS 17—A TRaNsient SYstem Simulation Program, User Manual. Multizone Building Modeling with Type 56 and TRNBuild. Version 17.1; University of Wisconsin: Madison, WI, USA, 2010

[5] Arpa Lombardia, https://www.arpalombardia.it/Pages/Meteorologia/Richiesta-dati-misurati.aspx

[6] Sirmip Marche, http://app.protezionecivile.marche.it/sol/indexjs.sol?lang=it

[7] Meteotest: J. Remund, S. Müller, M. Schmutz, D. Barsotti, C. Studer, R. Cattin. Meteonorm Handbook part I-II, 2020

[8]: Guo, X.-M.; Chen, Y.-G.;Wang,W.-H.; Chen, C.-Z. Experimental study on frost growth and dynamic performance of air source heat pump system. Appl. Therm. Eng. 2008, 28, 2267–2278. https://doi.org/10.1016/j.applthermaleng.2008.01.007

[9]: Zhu, J.; Sun, Y.; Wang, W.; Deng, S.S.; Ge, Y.; Li, L. Developing a new frosting map to guide defrosting control for air-source heat pump units. Appl. Therm. Eng. 2015, 90, 782–791. https://doi.org/10.1016/j.applthermaleng.2015.06.076

[10]: Vocale, P.; Morini, G.L.; Spiga, M. Influence of Outdoor Air Conditions on the Air Source Heat Pumps Performance. Energy Procedia 2014, 45, 653–662. https://doi.org/10.1016/j.egypro.2014.01.070

[11]: Rossi di Schio, E.; Ballerini, V.; Dongellini, M.; Valdiserri, P. Defrosting of Air-Source Heat Pumps: Effect of Real Temperature Data on Seasonal Energy Performance for Different Locations in Italy. Applied Sciences 2021, 11, 8003, https://doi.org/10.3390/app11178003.

[12]: Italian Thermotecnical Committee. Available online: http://try.cti2000.it/ (Accessed on 25 August 2023).

[13]: Song, M.; Deng, S.S.; Dang, C.; Mao, N.;Wang, Z. Review on improvement for air source heat pump units during frosting and defrosting. Appl. Energy 2018, 211, 1150–1170. https://doi.org/10.1016/j.apenergy.2017.12.022

[14]: Buick, T.R.; McMullan, J.T.; Morgan, R.; Murray, R.B. Ice detection in heat pumps and coolers. Int. J. Energy Res. 1978, 2, 85–98. https://doi.org/10.1002/er.4440020109

[15]: Dongellini, M.; Piazzi, A.; De Biagi, F.; Morini, G.L. The modelling of reverse defrosting cycles of air-to-water heat pumps with TRNSYS. E3S Web Conf. 2019, 111, 01063. https://doi.org/10.1051/e3sconf/201911101063

[16]: Dongellini, M.; Ballerini, V.; Morini, G.L.; Naldi, C.; Pulvirenti, B.; Rossi di Schio, E.; Valdiserri, P. A New Climate Chamber for Air-Source and Ground-Source Heat Pump Testing Based on the Hardware-in-the Loop Approach: Design and Cross Validation. Journal of Building Engineering 2023, 64, 105661, https://doi.org/10.1016/j.jobe.2022.105661.

[17]: A.T. De La Cruz, P. Riviere, D. Marchio, O. Cauret, A. Milu, Hardware in the loop test bench using Modelica: a platform to test and improve the control of heating systems, Appl. Energy 188 (2017) 107–120. https://doi.org/10.1016/j.apenergy.2016.11.092.

[18]: M. Anderson, M. Buehner, P. Young, D. Hittle, C. Anderson, J. Tu, D. Hodgson, An experimental system for advanced heating, ventilating and air conditioning (HVAC) control, Energy Build. 39 (2007) 136–147. https://doi.org/10.1016/j.enbuild.2006.05.003.

[19]: R. Lahrech, P. Gruber, P. Riederer, P. Tessier, J.C. Visier, Development of a testing method for control HVAC systems by emulation, Energy Build. 34 (2002) 909–916. https://doi.org/10.1016/S0378-7788(02)00067-1.

[20]: P. Haves, A. Dexter, D.R. Jorgensen, K.V. Ling, G. Geng, Use of a building emulator to develop techniques for improved commissioning and control of HVAC system, ASHRAE Transaction 97 (1991) 684–688.

[21]: UNI EN 14511-3, Air Conditioners, Liquid Chilling Packages and Heat Pumps for Space Heating and Cooling and Process Chillers, with Electrically Driven Compressors - Part 3: Test Methods, 2018.

3 Dynamic analysis of solar – assisted heat pumps coupled to ground heated by solar collectors

In this chapter, a dynamic analysis related to geothermal heat pumps serving a school virtually located in Milan [**1**] will be presented. The analyzed system includes the presence of solar thermal collectors: during the winter, the solar collectors provide heat to the building, while during the summer and mid-seasons, when the building's thermal demand is null, the heat extracted from the solar collectors is supplied to the field of geothermal probes to which the two heat pumps are coupled. The goal is to limit soil temperature drift and stabilize the machine's *SCOP* value. The dynamic analysis, conducted with the Trnsys software [**2-3**], was carried out considering a time horizon of 15 years (thus, we can speak of long-term dynamic analysis) and different scenarios were considered, taking into account different lengths of the geothermal probe field and different surface areas of the solar collectors. Additionally, long-term dynamic simulations are a crucial tool for determining whether the heat pump tends to lose efficiency over the years due to an improperly sized probe field. The analyses conducted were carried out for all 15 years, considering the same climatic conditions, highlighting the importance of accurately sizing the geothermal probe field to maintain efficiency and prevent performance degradation over time.

3.1 Building analyzed

The school being studied is depicted in **Figure 3.1**. It's a two-story structure ideally situated in Milan (45° 27’ 39.24” N, 9° 16’ 48” E), characterized by 2404 degree-days and an annual heating period from October 15 to April 14. Beneath the ground floor of the building is an unheated basement. As detailed in **Table 3.1**, the combined floor area of both levels is approximately 2300 m^2, with a total volume nearing 8400 m^3. The gymnasium and stairwell feature a ceiling height of 6 meters, while the remaining thermal zones have a height of 3 meters.

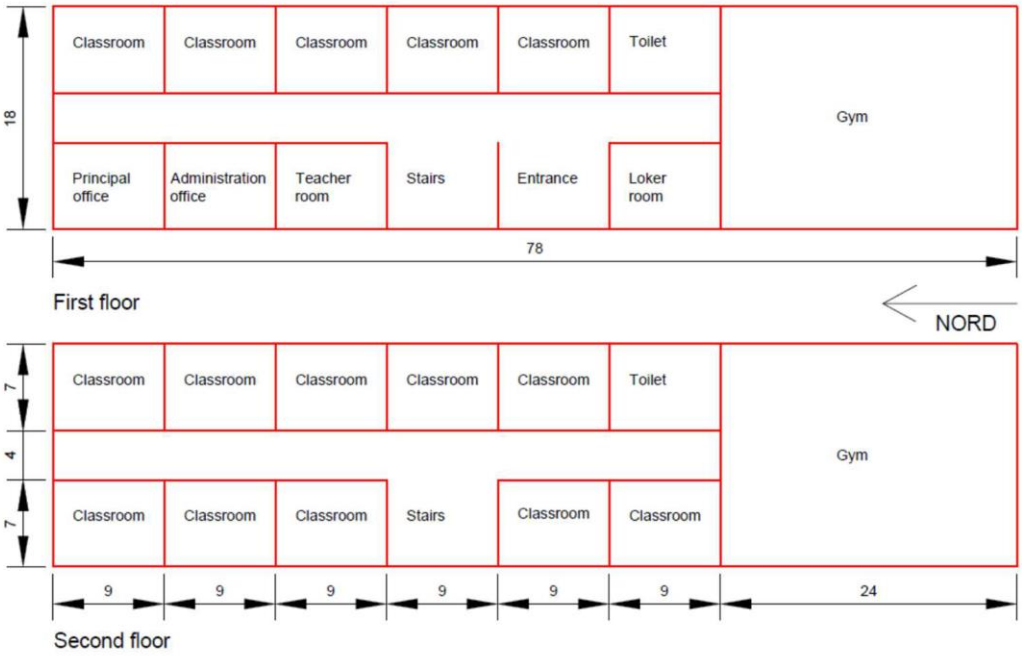

(**a**)

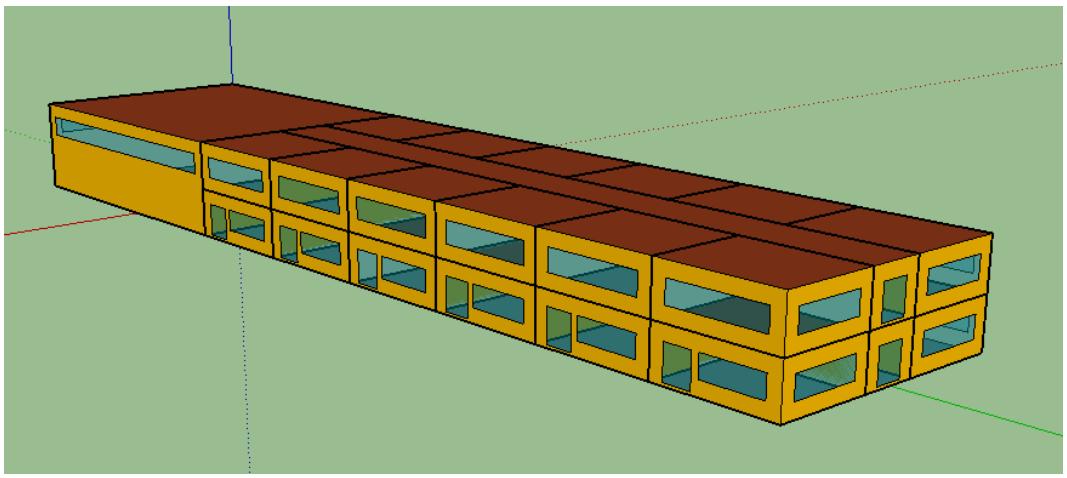

(**b**)

Figure 3.1 – layout of the school (**a**); 3D view of the building analyzed (**b**).

Table 3.1 – Floor area of the thermal zones.

Zone	**Floor area (m^2)**
Classrooms	945
Corridors	432
Entrance	63
Gymnasium	432
Locker room	63

Presidency	63
Secretariat	63
Stairwell	63
Teachers' offices	63
Toilets	126
Total	2313

Table 3.2 provides the thermal transmittance values for the primary building components. The windows are designed with double glazing (4/12/4 mm), enhanced with a low-emission treatment and filled with argon, set within a wooden frame, resulting in a total transmittance of U = 1.69 W/(m^2K). Additionally, with a 10 cm insulation thickness in the external walls, the building is considered to be well-insulated for Milan's climatic conditions.

Table 3.2 – Thermal transmittance *U* of the main elements.

Element	**Transmittance W/(m^2K)**
external walls	0.292
Ceiling	0.287
Floor	0.342
Partitions	1.098
Windows	1.690

The set points are reported in **Table 3.3** and are applied valid every day of the heating season from Monday to Saturday; on Sunday and when there are no activities in the school the heating is turned off. Public holidays have not been considered in analysis.

Table 3.3 – Set points of the different thermal zones.

Zone	**$t_{set-point}$ (°C) (7:00-17:30)**	**$t_{set-point}$ (°C) (17:00-7:00)**	**Floor area (m^2)**
Classrooms, toilets, secretariat, Presidency, teachers' offices	20	-	1260
Corridors, stairwell, entrance	18	-	558

Gymnasium	18	-	432
Locker room	22	-	63

3.2 Heating system

The heating system uses fan-coils as the delivery mechanisms, which are simulated in Trnsys using a fan and a heating coil (type 744 and 753d, respectively). Each zone's temperature is regulated individually, with a thermostat that provides three stages corresponding to fan speeds (0.6/0.75/1 P_{max}). The fan-coils were designed based on an exterior benchmark temperature of -5°C, aiming to achieve a set-point temperature of 20°C within roughly an hour. The airflow and water flow rates for the fan-coils were estimated in relation to the thermal power of the emitters at rated conditions, referencing a commercial model: 140 kg/(kW) for water flow rate and 150 kg/(kW) for air flow rate (these values are related to a unitary thermal power of the emitters at rated conditions). Specific details about the fan-coils for each heating zone can be found in **Table 3.4**, while a Trnsys diagram of the delivery system is illustrated in **Figure 3.2**.

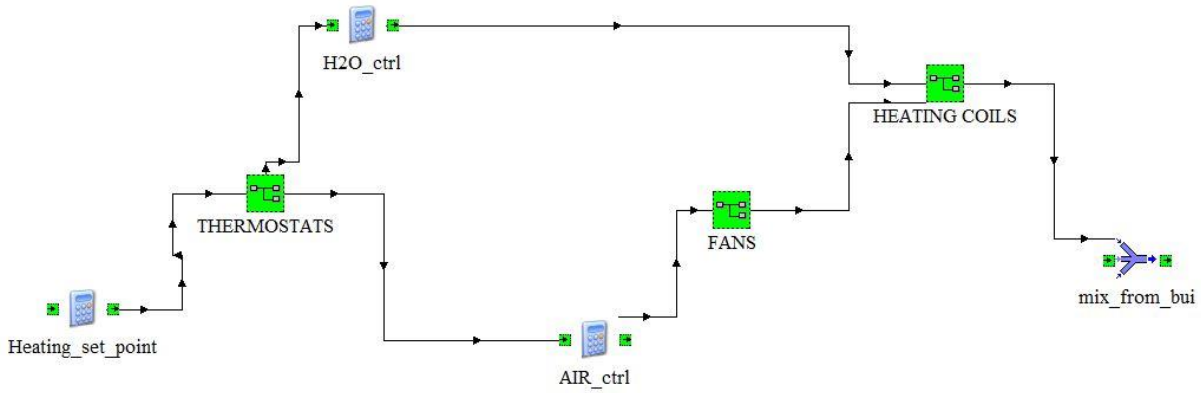

Figure 3.2 – Sketch of the emission system, as built in Trnsys.

Table 3.4 – Technical data related to the terminal emitters placed in the thermal zones.

Zone	Thermal power (kW)	Water flow rate (kg/h)	Air flow rate (kg/h)
Classrooms (each)	4.5	630	675
Corridor first floor	10.5	1100	1575

Corridor ground floor	9.35	1000	1403
Entrance	3.0	300	450
Gymnasium	44.0	4600	6600
Locker room	5.0	700	750
Presidency	4.5	630	675
Secretariat	4.5	630	675
Stairwell	4.3	600	645
Teachers' offices	4.5	630	675
Toilet first floor	4.5	630	675
Toilet ground floor	4.5	630	675

In terms of the generation system, it operates under the assumption of having two water-to-water heat pumps, each with a capacity of 40 kW. These can function independently or concurrently. These heat pumps were modeled with thermal power and *COP* maps shown in **Figure 3.3**.

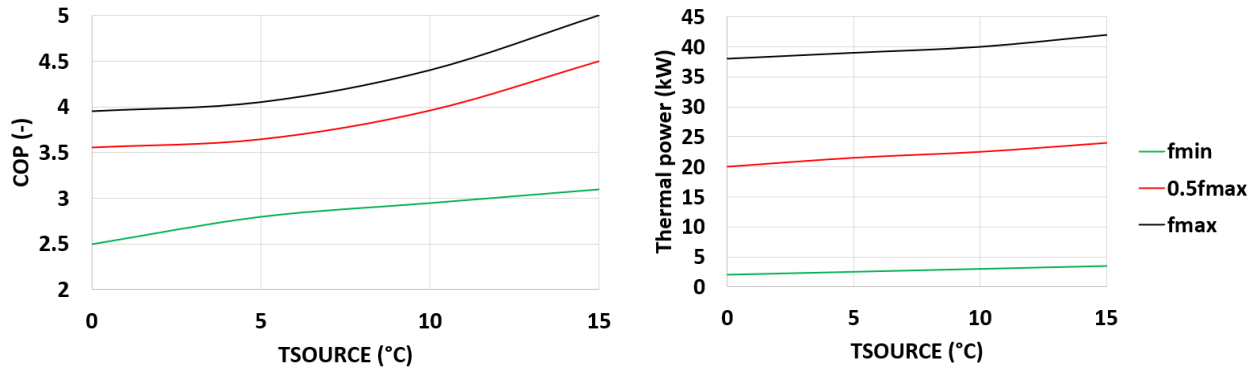

(**a**) (**b**)

Figure 3.3 – *COP* (**a**) and thermal power output (**b**) of the geothermal heat pumps for fixed inlet/outlet water temperature of 40°C and 45 °C, for different inverter frequency. T_{SOURCE} (°C) represents the water temperature flowing between the heat pumps and the geothermal field.

The system incorporates a 2000 l storage tank (Type 156), equating to 50 l/kW based on the power of the generators. Positioned in the building's basement, this tank features an internal coil (heat exchanger) dedicated to solar loop. The specifications for the coil include an internal and external diameter of the pipes at 0.020 m and 0.022 m respectively, a coil length of 200 m, and a thermal conductivity of 400 W/(mK). The storage tank connects both to the emission devices (with a maximum flow rate of 22,000 kg/h) and the heat pump. Depending on the simulation scenario, the flow rate for the solar collectors is set between 1500 - 3000 kg/h. All pumps operate with variable speed (Type 110).

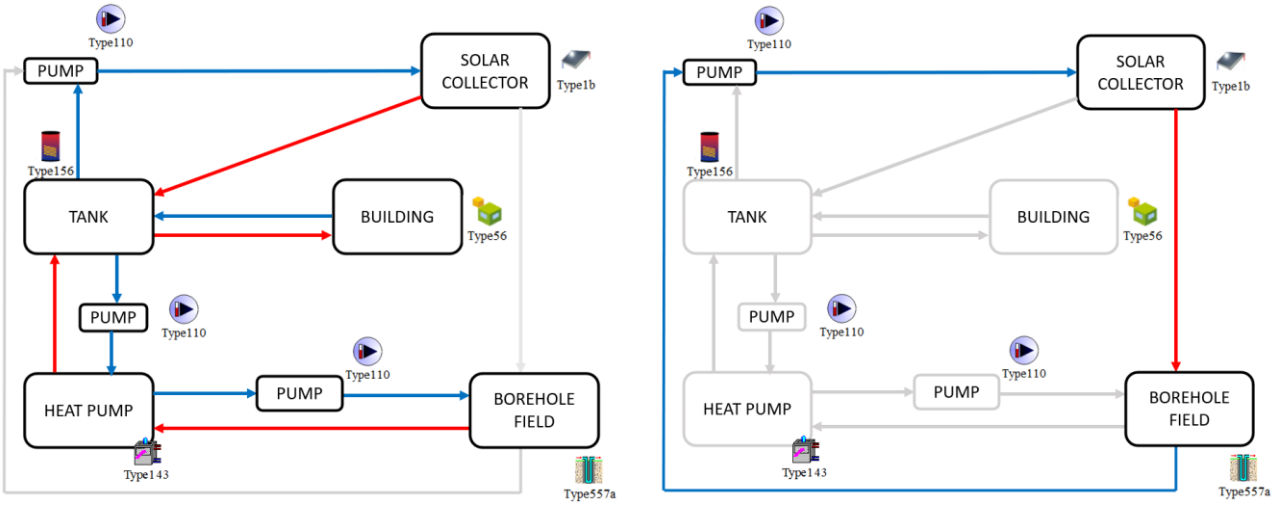

(**a**) (**b**)

Figure 3.4 – Plant working conditions in winter (**a**) and in summer (**b**); the grey lines represent non-active connections during the specific season.

The operational conditions for the plant during winter and summer are illustrated in **Figure 3.4**. Specifically, during winter, water from the solar collector is channeled into the heat exchanger within the storage tank. The warmed water from the storage then travels to the emission devices, providing heated air to the building's individual rooms. The heat pump's operation involves two circuits: one between the heat pumps and the tank, and the other between the heat pumps and the geothermal borehole field. In the summer, as is assumed to be no demand for cooling, the water from the solar collector is directed to the geothermal probes.

For the Trnsys simulations, certain assumptions were made. Air exchanges are set at 0.5 h^{-1} when the building is unoccupied and increase to 0.9 h^{-1} during occupation (Monday to Saturday, 7:00 to 17:30). The assumed occupancy is 25 individuals in the classrooms and gym, 2 in restrooms, offices, and locker rooms, and 5 in corridors, faculty offices, and the administration office. The sensible heat load per individual is calculated at 60 W (with 40 W as radiative and 20 W as convective gain [**4**]). For latent heat, vapor production is set at 0.065 kg/h per person in all rooms, except in the gym where it's elevated to 0.45 kg/h per individual.

The solar control system activates the solar pump when the collector's outlet temperature surpasses the tank temperature by more than 10 K during winter. In summer, the system only activates if the inlet temperature to the probes exceeds the probe exit water temperature by more than 10 K. In these situations, the pump operates with variable speed control.

To numerically simulate the ground probes, the soil was assumed to have a density of 2800 kg/m³, a conductivity of 1.8 W/(mK), and a thermal capacity of 0.85 kJ/(kgK). The probes are single U-tube designs with an outer diameter of 0.2 m, a pipe center distance of 0.1 m, and an outer pipe diameter of 33 mm. The probes extend to a depth of 100 m. The pipe's conductivity is 0.4 W/(mK), while the sealing mortar has a conductivity of 1.6 W/(mK). An initial soil temperature of 14°C is estimated, and Type 557a is used in the modeling. Approximate sizing, based on the ASHRAE method, suggests a probe field of 2.7 km, assuming solar energy input is excluded. For simulating the behavior of the solar collectors, the Trnsys Type 1b was utilized. The parameters considered include an intercept efficiency of 0.807, an efficiency slope of 3.766 W/(m²K), a curvature efficiency of 0.0059 W/(m²K²), and a collector slope of 35° facing the south direction. The total surface area of the collectors varies based on different simulation groups, which will be detailed in the subsequent chapter.

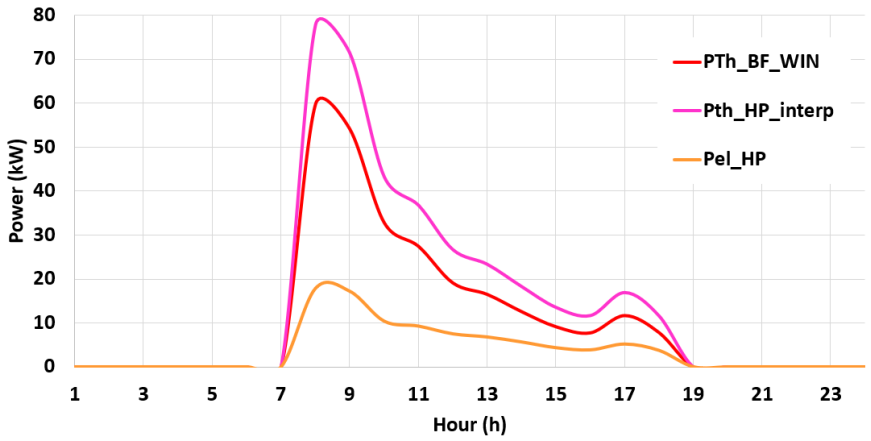

(**a**)

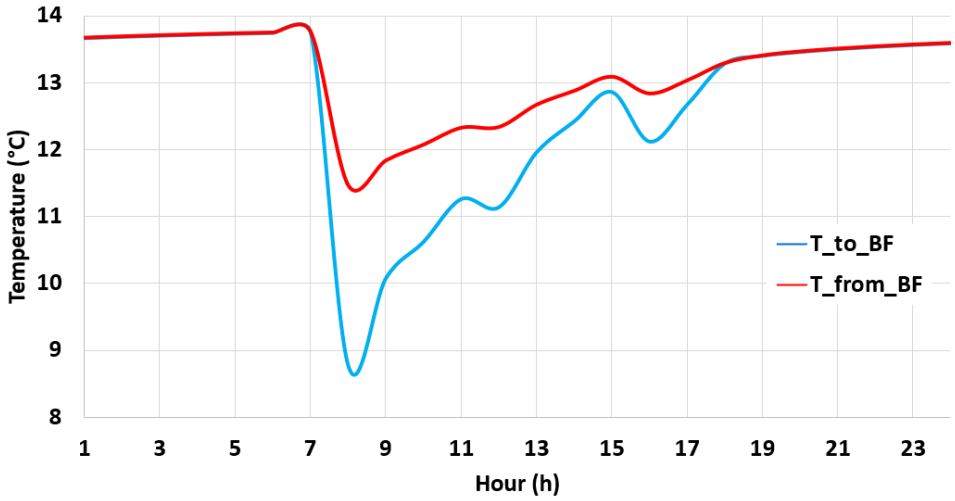

(**b**)

Figure 3.5 – Plant operation conditions during a typical day of the heating season for a well-sized ground borehole field: trends of thermal power delivered (Pth_HP_interp), electricity demand (Pel_HP) of the heat pumps and thermal power taken from the ground field (Pth_BF_WIN) in (**a**); water inlet/outlet temperature (T_to_BF and T_from_BF respectively) to the boreholes (**b**).

The dynamic analyses conducted will be elaborated on in the following section. However, it's noteworthy to highlight the plant's operational conditions during a typical heating season day here. A scenario where the ground field is sized accurately, based on the ASHRAE dimensioning method, was considered. **Figure 3.5** illustrates the water

temperature trends at the inlet and outlet of the borehole fields during a typical heating season day, along with the typical power dynamics of the two heat pumps. This encompasses electricity demand, power directed to the hot tank, and power extracted from the borehole field.

Focusing on **Figure 3.5(a)**, we notice that the largest temperature difference between the borehole field's inlet and outlet occurs in the morning. This coincides with the building's peak thermal demand and the maximum power provided by the heat pumps, resulting in a temperature difference of 3 K and a minimum temperature of 8.5°C.

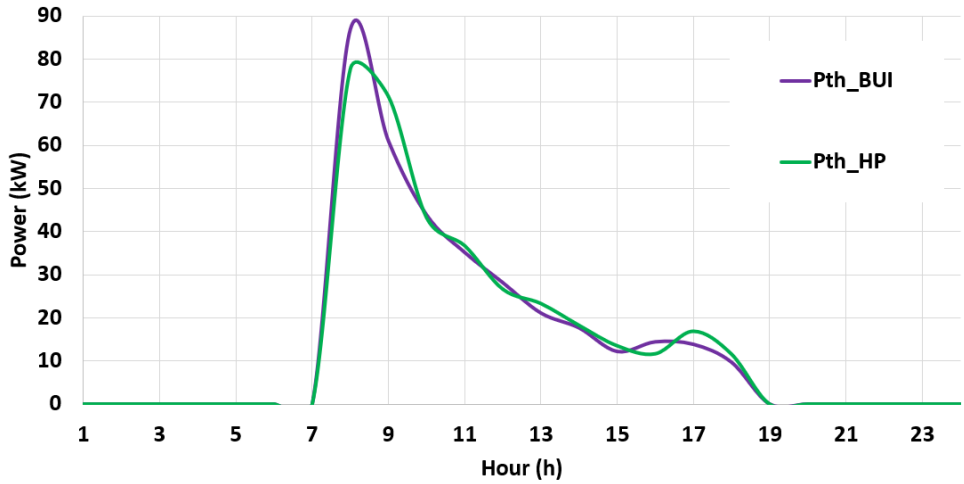

Figure 3.6 – Trends of the power given by the two heat pumps to the hot tank (Pth_HP) and power delivered from the hot tank to the building (Pth_BUI) during a typical day of the heating season.

Furthermore, **Figure 3.6** presents the power provided by the heat pumps to the hot tank and the power delivered to the building's fan coils. A morning peak is evident, immediately following the reactivation of the heating after the nighttime pause. The introduction of storage is also clearly seen, with its effect of reducing peak thermal power (with the building demanding roughly 90 kW and the total maximum power provided by the two heat pumps around 80 kW) and distributing it over time. Throughout the day, the power required to maintain the set-point temperatures in the building decreases, stabilizing between 2:00 pm and 6:00 pm at values close to 15 kW.

3.1.3 Dynamic analyses performed and results

Table 3.5 – Dynamic analyses performed.

Case	Number of probes	Solar panels (m^2)
A1	25	0
A2	20	0
A3	15	0
A4	10	0
A5	25	30
A6	20	30
A7	15	30
A8	10	30
A9	25	40
A10	20	40
A11	15	40
A12	10	40

12 different simulations have been performed, adjusting the number of probes and the area of the solar collectors, with the goal of determining the soil temperature over a 15-year period. The specifics of these simulations are detailed in **Table 3.5**. Three distinct simulation groups can be identified: From A1 to A4, the simulations do not include solar collectors; from A5 to A8, the simulations incorporate solar collectors with a total area of 30 m^2; and the final four simulations account for solar collectors with an area of 40 m^2. Within each group, different lengths of the field have been considered, with each probe being 100 m in length. Fields properly sized according to the ASHRAE method (comprising 25 probes) have been examined, as well as undersized fields of 20, 15, and 10 probes.

Table 3.6 – Annual electricity demand (EE) and thermal power output (ET) of the heat pump averaged over the 15 year of simulation.

Case	***EE*** **(MWh)**	***ET*** **(MWh)**

A1	12.37	46.35
A2	12.51	46.30
A3	12.68	46.24
A4	12.97	46.03
A5	11.26	43.10
A6	11.33	42.79
A7	11.56	43.00
A8	11.86	43.02
A9	10.98	42.32
A10	11.11	42.29
A11	11.28	42.22
A12	11.53	42.07

In **Table 3.6**, the average annual thermal energy (averaged over the 15 years of simulations conducted) and the electricity demand associated with the geothermal heat pumps are presented for each simulation. For instance, when examining cases A1 – A4 in **Table 3.6** (scenarios without solar collectors), there is a noticeable 5% increase in electricity demand for case A4 (with a total ground probe length of 1 km) compared to case A1 (with a total length of 2.5 km). Additionally, in simulations from A1 to A4, the thermal energy delivered to the storage is greater than in the subsequent simulations, averaging 46.23 MWh for cases A1 to A4, compared to an average of 42.65 MWh for simulations A5 to A12. There's also an increasing trend in the electricity demand for each simulation group as previously indicated. As the total length of the field decreases, the total annual electricity required by the heat pump increases, all other conditions being equal.

In **Table 3.7**, the thermal energy required and injected into the borehole field is detailed for each simulation. Additionally, the table displays the thermal energy provided by the solar collector (if included in the analysis) to the hot water tank during winter and the energy directed to the borehole field during summer. Upon examining **Table 3.7**, it's evident that the energy extracted from the ground consistently surpasses the energy reintroduced, even in scenarios A9 – A12 (which consider a collector surface area of 40 m^2). The net energy imbalance for the ground spans from -33.99 MWh in scenario A1 to -2.15 MWh in scenario A12. Focusing on the energy contributions from the solar collectors for simulation sets with identical collection areas, specifically A5-A8 (30 m^2)

and A9-A12 (40 m^2), it's notable that an approximate 33.3% boost in collection area corresponds to a nearly 31.7% uptick in thermal energy harnessed by the collectors during summer. Conversely, during the heating season, the escalation is more subdued, shifting from an average of 3.72 MWh in scenarios A5-A8 to an average of 4.63 MWh in scenarios A9-A12, marking a 24.5% increase. The modest winter-time enhancement in solar collector output with increased surface area doesn't seem to substantially influence the thermal energy drawn from the geothermal probes. When comparing the two simulation sets, A5-A8 averages 31.48 MWh and A9-A12 averages 30.75 MWh. However, when gauging the yearly difference between the thermal energy extracted from the geothermal field in winter and the energy supplied in summer for the identical simulation set, the A9-A12 scenarios exhibit an average yearly thermal energy extraction of 2.39 MWh in contrast to 9.97 MWh for the A5-A8 set, indicating an approximate 76% drop in energy extraction.

Table 3.7 – Annual thermal energy taken from the borehole field ($ET_{BF,TOT}$), sum of the thermal energy taken by the heat pump during winter season ($ET_{BF,winter}$) and thermal energy given to the ground by the solar collector during summer ($ET_{BF,summer}$). Yearly thermal energy given by the solar collectors ($ET_{SC,TOT}$), sum of solar energy given during winter ($ET_{SC,winter}$) and summer ($ET_{SC,summer}$). The values reported are the mean average during the 15 years of Trnsys simulations.

CASE	$ET_{BF,summer}$ (MWh)	$ET_{BF,winter}$ (MWh)	$ET_{BF,TOT}$ (MWh)	$ET_{SC,winter}$ (MWh)	$ET_{SC,summer}$ (MWh)	$ET_{SC,TOT}$ (MWh)
A1	0	-33.99	-33.99	0	0	0
A2	0	-33.8	-33.80	0	0	0
A3	0	-33.55	-33.55	0	0	0
A4	0	-33.07	-33.07	0	0	0
A5	21.69	-31.85	-10.16	3.69	25.38	21.69
A6	20.89	-31.47	-10.58	3.99	24.88	20.89
A7	21.66	-31.44	-9.78	3.69	25.35	21.66
A8	21.80	-31.16	-9.36	3.49	25.29	21.80
A9	28.75	-31.35	-2.60	4.63	33.38	28.75
A10	28.70	-31.18	-2.48	4.63	33.33	28.70
A11	28.61	-30.94	-2.33	4.63	33.24	28.61
A12	28.40	-30.55	-2.15	4.64	33.04	28.40

In **Figure 3.7**, the progression of ground temperature across all considered scenarios is illustrated. Specifically, **Figures 3.7a**, **b**, and **c** display the ground temperature trends over the 15-year span, revealing the characteristic annual periodic fluctuations (with lower ground temperatures in winter and higher ones in summer). **Figure 3.8** presents the average seasonal *COP* of the two heat pumps throughout the 15 years of simulation.

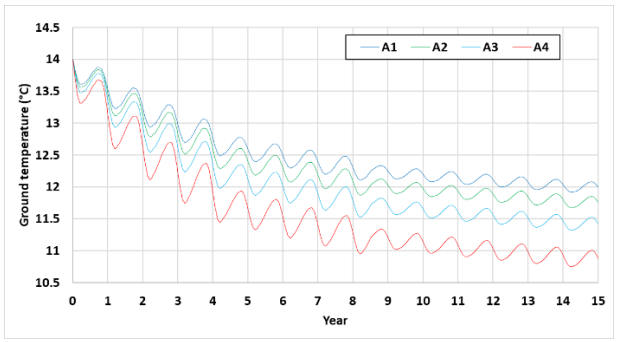

a

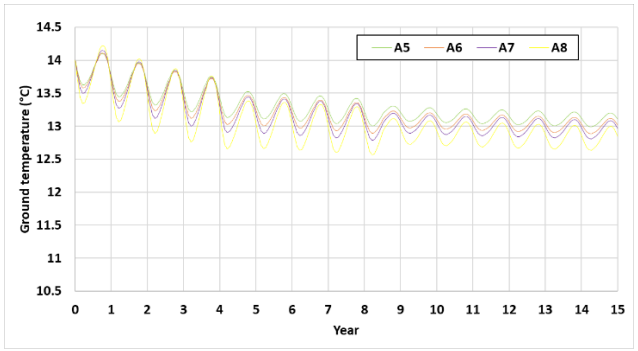

b

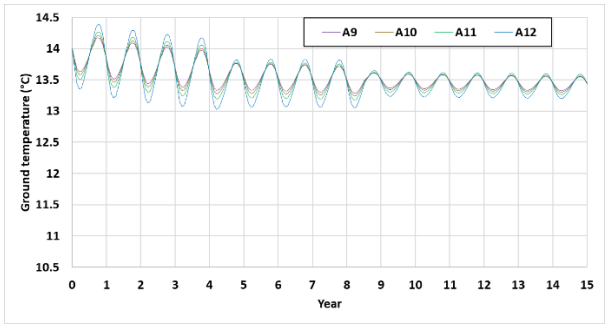

c

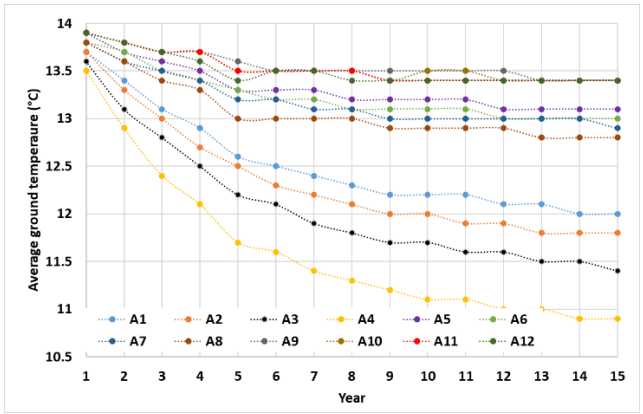

d

Figure 3.7 – Ground temperature around the ground field during the 15 years of simulation (**a, b, c**); mean annual ground temperature around the field for the 12 simulations (**d**).

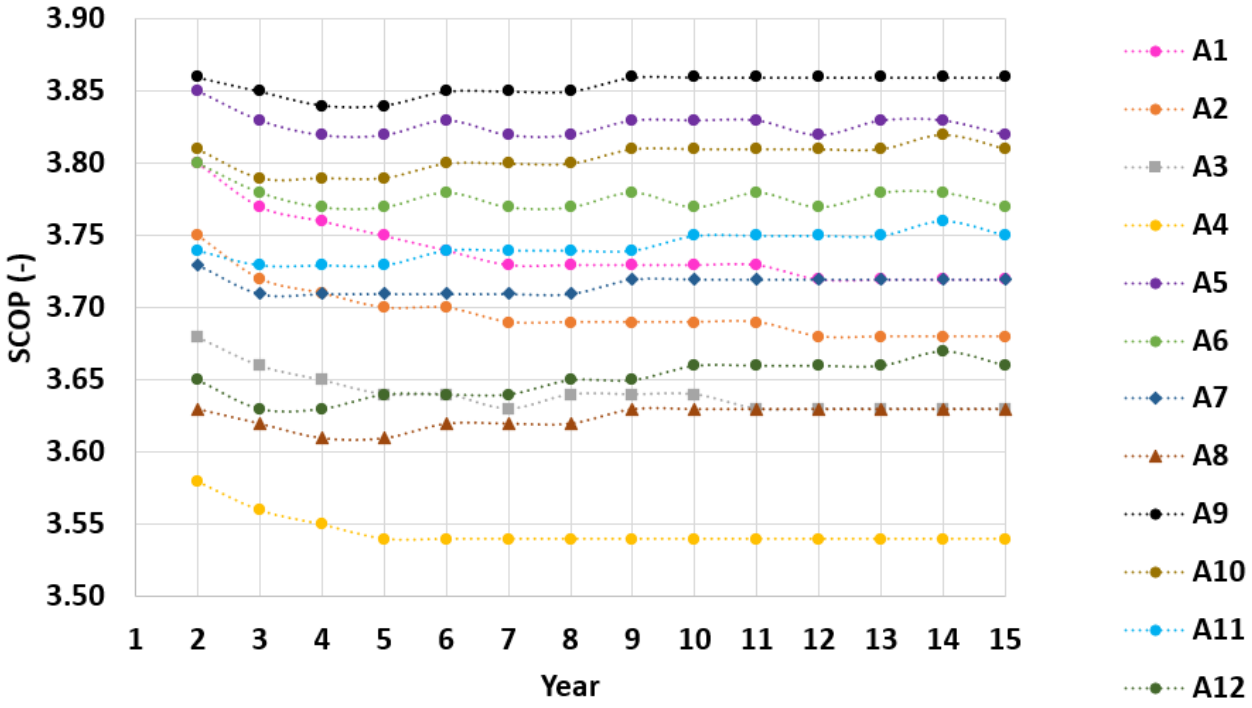

Figure 3.8 – Mean annual seasonal coefficient of performance of the two heat pumps along the 15 years of dynamic simulation.

For scenarios A1 – A4, as discernible from **Figures 3.7** and **3.8**, there is a decline in both the ground temperature and the *SCOP* (for A1 and A4, the ground temperatures are 12 °C and 10.9 °C respectively by the fifteenth year; *SCOP* in the final year stands at 3.72 for A1 and 3.54 for A4). One noteworthy observation about A4's *SCOP* and ground temperature is that while the *SCOP* remains relatively stable from the fifth year onward, the ground temperature continues its downward trajectory even in the later simulation years.

The decreased thermal energy demand from the ground field in scenarios A5 – A12, attributed to the incorporation of solar collectors, results in a stabilization of the ground temperature after five years, fluctuating between 12.8 °C and 13.4 °C. Specifically, 13.4 °C is observed in simulations A9 – A12, which account for a collector area of 40m^2. The integration of solar collectors not only stabilizes the SCOP but also elevates it (as seen in **Figure 3.8**) compared to cases A1 – A4.

Moreover, **Figure 3.7** reveals that as the simulation progresses over the years, the amplitude of temperature variations lessens compared to the initial years. This stabilization is especially pronounced in scenarios with undersized borehole fields

relative to those with adequately sized borehole fields, even when solar thermal panels are integrated. Concurrently, the *SCOP* also tends to find a steady state in the concluding simulation years.

Another observation gleaned from **Figure 3.8** concerns the *SCOP* enhancement in scenarios with an identical ground field but augmented by solar collectors. For instance, comparing a field comprised of 25 boreholes without solar collectors (A1) to scenarios where the field integrates solar collectors (A5 and A9), the *SCOP* increase by the fifteenth year is 2.7% and 3.8% respectively for A5 and A9 relative to A1. When examining the *SCOP* for the undersized field made up of 10 boreholes, the rise is 2.5% and 3.7% respectively for A8 and A12 in comparison to A4.

3.4 Main findings of the analysis

From the comprehensive dynamic analysis conducted, several pivotal insights emerge:

- Solar collectors, when paired with geothermal heat pumps, present a promising solution for mitigating soil temperature drift and countering the degradation in heat pump performance over time. This is particularly evident in scenarios like the one analyzed here, where the load demands on the borehole field are imbalanced across heating and cooling seasons.
- The Seasonal Coefficient of Performance (*SCOP*) recorded in the final year of the simulation demonstrates that opting for a solar collector area of 40 m^2 over 30 m^2 yields marginally improved results. However, the overall influence of the solar collector's dimension on the *SCOP* is somewhat restrained. For instance, comparing case A9 to case A5, there's a mere 1% increase in *SCOP*. Yet, when analyzing scenarios with identical collector areas, such as cases A9 through A12, the decrease in *SCOP* due to an undersized ground field is as pronounced as 5% by the end of the fifteenth simulation year.
- Employing an undersized borehole field invariably results in a decline in the *SCOP* of geothermal heat pumps over the years. Nonetheless, this decline can be somewhat offset if the soil undergoes a refill during the summer months. This consideration is paramount during the design phase since it might be economically prudent to scale down the borehole field size and contemplate pairing the heat pump with solar collectors, thereby facilitating ground-refill during the summer.

References

[1]: Ballerini, V.; Rossi di Schio, E.; Valdiserri, P.; Naldi, C.; Dongellini, M. A Long-Term Dynamic Analysis of Heat Pumps Coupled to Ground Heated by Solar Collectors. Applied Sciences 2023, 13, 7651, http://www.doi.org/10.3390/app13137651.

[2]: A: Klein, S.A. et al, 2017, TRNSYS 18: A Transient System Simulation Program, Solar Energy Laboratory, University of Wisconsin, Madison, USA, http://sel.me.wisc.edu/trnsys (Accessed 24 February 2023).

[3]: Klein, S.A.; Duffie, A.J.; Mitchell, J.C.; Kummer, J.P.; Thornton, J.W.; Bradley, D.E.; Arias, D.A.; Beckman, W.A.; TRNSYS 17—A TRaNsient SYstem Simulation Program, User Manual. Multizone Building Modeling with Type 56 and TRNBuild. Version 17.1; University of Wisconsin: Madison, WI, USA, 2010.

[4]: Dott, R.; Haller, M.; Ruschenburg, J.; Ochs, F.; Bony, J. IEA-SHC Task 44 Subtask C Technical Report: The Reference Framework for System Simulations of the IEA SHC Task 44/HPP Annex 38: Part B: Buildings and Space Heat Load. IEA-SHC. 2013. http://www.taskx.iea-shc.org/data/sites/1/publications/T44A38_Rep_C1_B_ReferenceBuildingDescription_Final__Revised_130906.pdf (Accessed online 29 September 2023).

4. Comparison between air-source heat pumps and gas boilers as heating generator: energy and economic analysis in Italy in the framework of Russo – Ukrainian conflict

In the previous chapters, the analyses of heat pumps were explored, involving dynamic and experimental studies. This chapter, however, will introduce economic and efficiency analyses, comparing the use of an electric heat pump to a condensing gas boiler. This analysis was conducted during a significant increase in energy prices (2021-2022). Accompanying this analysis will be a dynamic study to determine the savings attainable from reducing the winter heating set-point temperature by 1°C, in accordance with Italian regulations at the time to counteract high costs and potential energy shortages. All analyses were conducted with reference to Italy and involved using Trnsys to analyze a residential building (a small independent house of 80 m^2) located in different municipalities of Italy (Rome, Milan, and Naples). In more detail, the thermal demand of a residential building in three different climates (zone C, D, and E, according to the Italian classification of climates based on climate bands) was analyzed, considering three different types of building envelopes for each location, in order to best represent the majority of constructions found across Italy. The thermal demand obtained for each considered scenario was then used to determine the actual operating costs of a heating system featuring an air-water heat pump and, alternatively, a condensing boiler paired with the same terminal emitters. The prices of electricity and gas were obtained from the website of the Italian Regulatory Authority for Energy, Networks, and Environment (ARERA) [**1**], pertaining to the years 2019-2022. The analyses reported in this study were published in [**2**].

4.1 Building analyzed

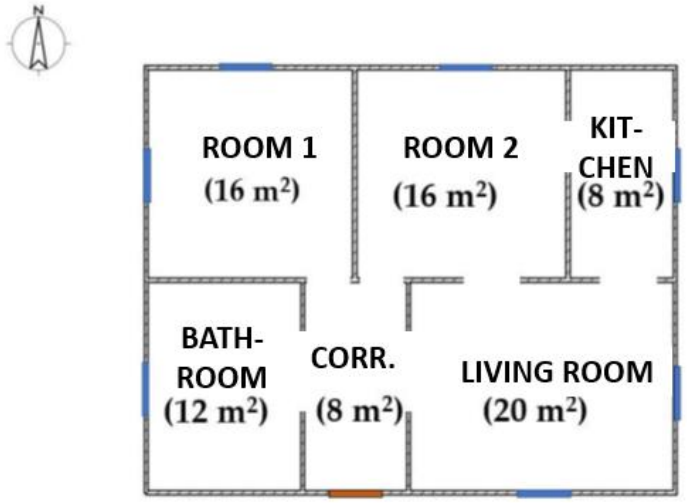

Figure 4.1 - Layout of the residential building.

Table 4.1 - Transmittance values of principal building envelope elements for buildings RB1, RB2 and RB3.

Envelope element	RB1 (W/m²K)	RB2 (W/m²K)	RB3 (W/m²K)
External walls	1.16	0.62	0.28
Floor	1.23	0.55	0.26
Internal walls	1.20	1.20	1.20
Roof	1.37	0.55	0.28
Windows	1.62	1.62	0.50

In **Figure 4.1**, the layout of the considered residential building is illustrated. A single-family house was investigated, boasting a floor area of 80 m² and a volume of 240 m³. The considered building encompasses six distinct thermal zones: two rooms (R1 and R2), a living room (LR), a kitchen (K), a bathroom (BA), and a corridor (CO). Three distinct sets of building envelope components, whose transmittances are documented in **Table 4.1**, were examined to closely align with the actual characteristics of a significant portion of buildings constructed in Italy in recent decades. The envelope elements of building RB1, as detailed in **Table 4.1**, are typical of Italian buildings erected between 1970 and 1990. In contrast, the envelope components of buildings RB2 and RB3 are indicative of more contemporary Italian residential constructions. More specifically, considering the external vertical walls, building RB1 is insulated solely

with an air layer of 0.08 m, while the more recently constructed buildings RB2 and RB3 feature a rock wool insulation layer with a conductivity of 0.04 W/(mK) and thicknesses of 0.04 m and 0.12 m, respectively. From the transmittance values listed in **Table 4.1**, it can be inferred that buildings RB1 and RB2 incorporate a double-glazed window, while the windows of building RB3 are distinguished by their triple glazing with a low-emissive surface treatment.

Figure 4.2 – Municipalities analyzed in Italy.

The behavior of the three buildings (RB1, RB2, and RB3) was assessed by virtually situating them in three different Italian municipalities: Milan (45°28' N, 9°11' E), Rome (41°54' N, 12°29' E), and Naples (40°21' N, 14°15' E), as depicted in **Figure 4.2**. Each municipality is characterized by its unique climate, resulting in varied winter design temperatures, heating degree days (HDD), and standard heating system operation periods, all of which are outlined in **Table 4.2**. Additionally, **Table 4.2** provides the thermal power demanded by the three buildings at the respective winter design temperatures of each municipality.

From the data outlined in the table, it is observable that Milan is the coldest of the considered municipalities, while Naples is the mildest. There is a notable reduction,

approximately 50%, in the peak winter power required by building RB3 compared to RB1 (55% in Milan, 54% in Rome, and 52% in Naples).

Table 4.2 - HDDs, winter design temperature, period of the heating season and design thermal load of the building for the tree buildings located in the three virtual localities.

Municipality	HDDs	Heating period	Winter design temperature (°C)	Winter thermal load (kW)		
				RB1	RB2	RB3
Milan	2404	15 October – 15 April	-5	10	6.6	4.5
Naples	1034	15 November – 31 March	2	7.5	5	3.6
Rome	1415	1 November – 15 April	0	8.2	5.5	3.8

4.2 Heating system

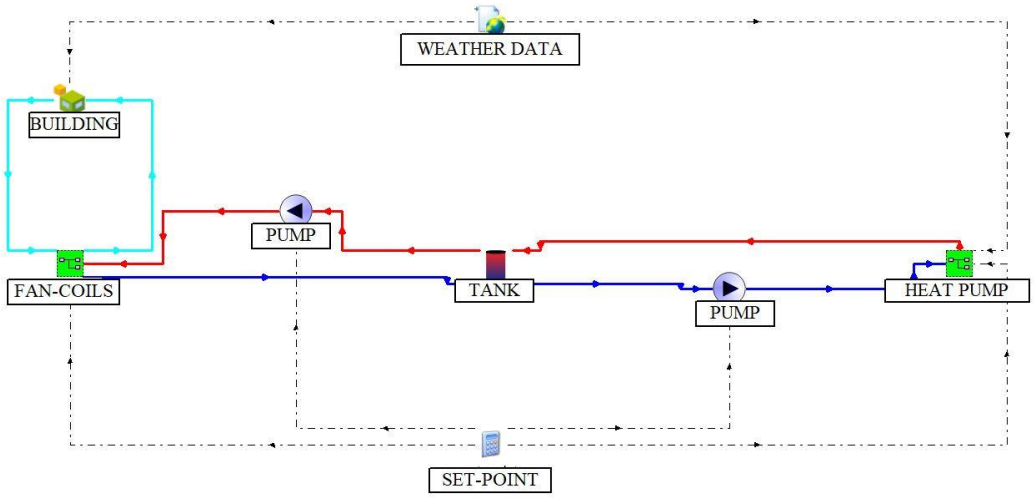

Figure 4.3 – Layout of the heating system (considering the heat pump as generation system).

The structure was equipped with five fan-coils designated for the aforementioned thermal zones: LR, K, R1, R2, and BA, with the corridor (CO) lacking any terminal emitter. **Figure 4.3** illustrates the heating system's layout, showcasing a 0.1 m³

thermal storage tank linked to both the fan-coils and the generator—an electric air-to-water inverter heat pump. The heat pump's size, in every dynamic simulation, was determined to meet the building's thermal power needs under design winter conditions, as outlined in **Table 4.2**. Nine distinct heat pumps were evaluated to accommodate the thermal requirements of the nine buildings under consideration. **Figure 4.4** delineates the thermal power output and the coefficient of performance (COP) of the heat pump for building RB1 in Milan, recorded at various inverter frequencies. Although other heat pumps exhibited identical COP, their thermal output differed, adjusted by a specific scaling factor. For clarity, the heat pump designated for building RB1 in Milan delivered a peak thermal power of 10 kW at an ambient outdoor temperature of -5°C. In contrast, the heat pump assigned to building RB1 in Naples provided a maximum thermal power of 7.5 kW, with the external temperature at 2°C.

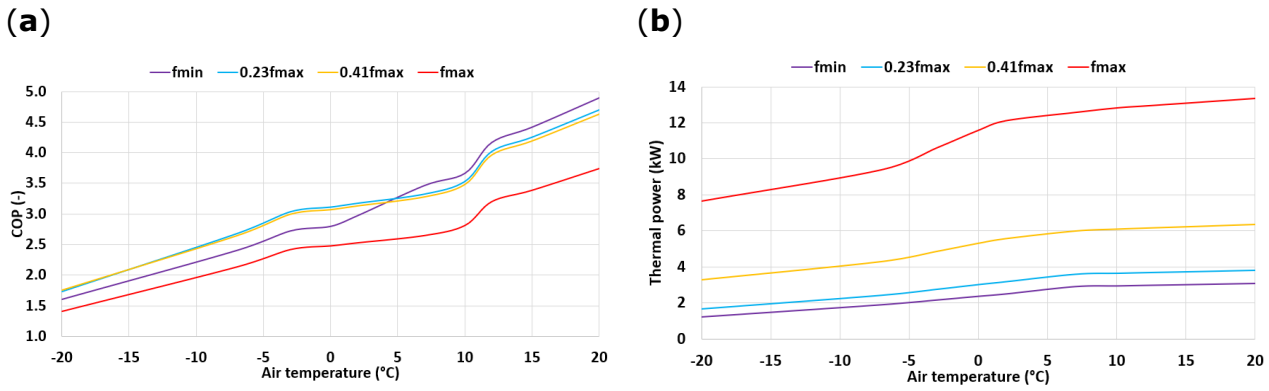

Figure 4.4 – COP (**a**) and thermal power output (**b**) of the heat pump coupled with building RB1 in Milan.

4.3 Dynamic analysis set-up

Dynamic simulations were conducted utilizing Trnsys software, version 17, [3], and Meteonorm database for weather data, with the objective of ascertaining the thermal and electric energy demands of the heat pump throughout the heating season. The structure was replicated using the type 56 multizone building model [4]. In contrast, the heat pump was represented utilizing models that allow for interpolations between provided values of COP and thermal power.

Table 4.3 – Temperature set-point of the thermal zones considered in dynamic simulations.

Case	Bathroom (°C)	Other zones (°C)

SP1	21	20
SP2	19	19
SP3	18	18

The simulations were structured with a timestep of 30 seconds, culminating in a total of 27 dynamic simulations. These assessments encompassed the three distinct buildings located in three separate municipalities, each subjected to varying set-point temperatures for their thermal zones, as detailed in **Table 4.3**. The set-point temperatures examined were 20°C, 19°C, and 18°C, with the exception of the bathroom, where the temperature was fixed at 21°C in scenario S1. This analytical approach, deviating from the conventional 20°C set-point typically adopted in Italian residential sectors, was prompted by recent mandates from the Italian government. These directives, outlined in [**5**], necessitate a reduction in indoor temperatures in residential edifices as a countermeasure to the prevailing energy crisis. The insights gleaned from these dynamic simulations are instrumental in quantifying the decrease in thermal energy demand for the three evaluated buildings situated in the respective municipalities. The findings and their implications are elaborated upon in the ensuing sections.

4.1.4 Data for economic analysis

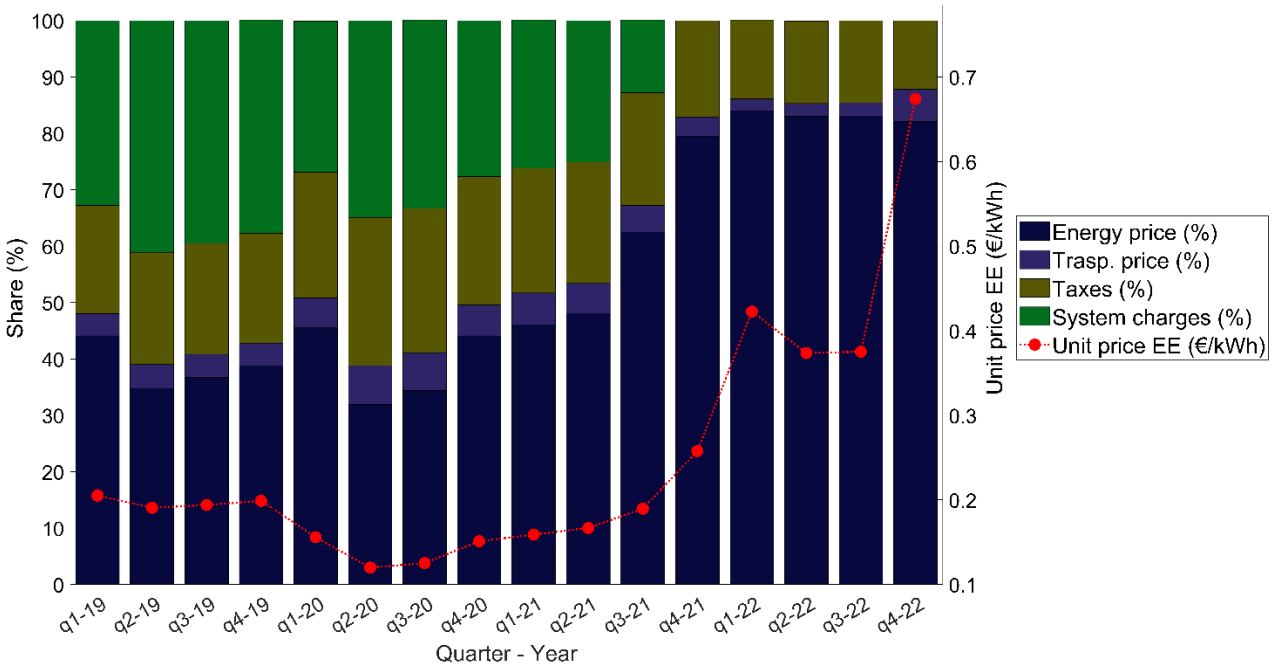

Figure 4.5 - Trends of the unit electricity price (€/kWh) and price components share as stated by the authority from first quarter of 2019 to the last quarter of 2022.

Information regarding electricity and gas pricing was sourced from the Italian Regulatory Authority for Energy, Networks, and Environment (ARERA) [**6, 7**]. In Italy, domestic consumers have the option to select between market offers and the standard-offer market for both electricity and gas supplies. With the former, the gas/electricity rate is determined by the contract agreed upon between the consumer and the energy provider. This price per unit (EUR/kWh for electricity or EUR/Sm³ for natural gas) can either be locked in for a specific duration or be subject to fluctuation. In the context of the standard-offer market, both electricity and gas prices are variable and are revised by ARERA on a quarterly basis. As indicated in the ARERA report [**8**], in 2021, 41.5% of domestic consumers were aligned with the standard-offer market for electricity, and 34.6% for natural gas.

Owing to the pronounced variability in electricity and gas prices within market offers, this study assessed prices set by the Italian Regulatory Authority spanning 2019 to 2022. Thus, the results of the analysis pertain primarily to "standard-offer market" rates. However, as highlighted earlier, these rates encapsulate the energy costs incurred by a significant segment of Italian domestic consumers.

For this study, "fixed costs" (namely, those unrelated to energy units, such as the annual fees for gas or electricity meters) were excluded. Delving deeper, the unit prices for both electricity and natural gas were broken down into four distinct components, as defined by ARERA: energy price, transportation and meter-management charges, system fees, and taxes (including excise duties and VAT).

Zooming in on electricity costs, **Figure 4.5** illustrates a substantial surge in electricity prices, particularly from the last quarter of 2021 to the end of 2022, with rates escalating from 0.190 €/kWh to 0.674 €/kWh. Across the entire evaluation period (2019–2022), significant shifts in the composition of price components were also evident. In 2019, energy prices and system charges each constituted between 30% and 45% of the final electricity price. However, in the subsequent year, the energy component dominated, accounting for as much as 84% of the unit price for electricity. Additionally, from the last quarter of 2021, system charges were completely eliminated by the Italian government to curb rising electricity costs.

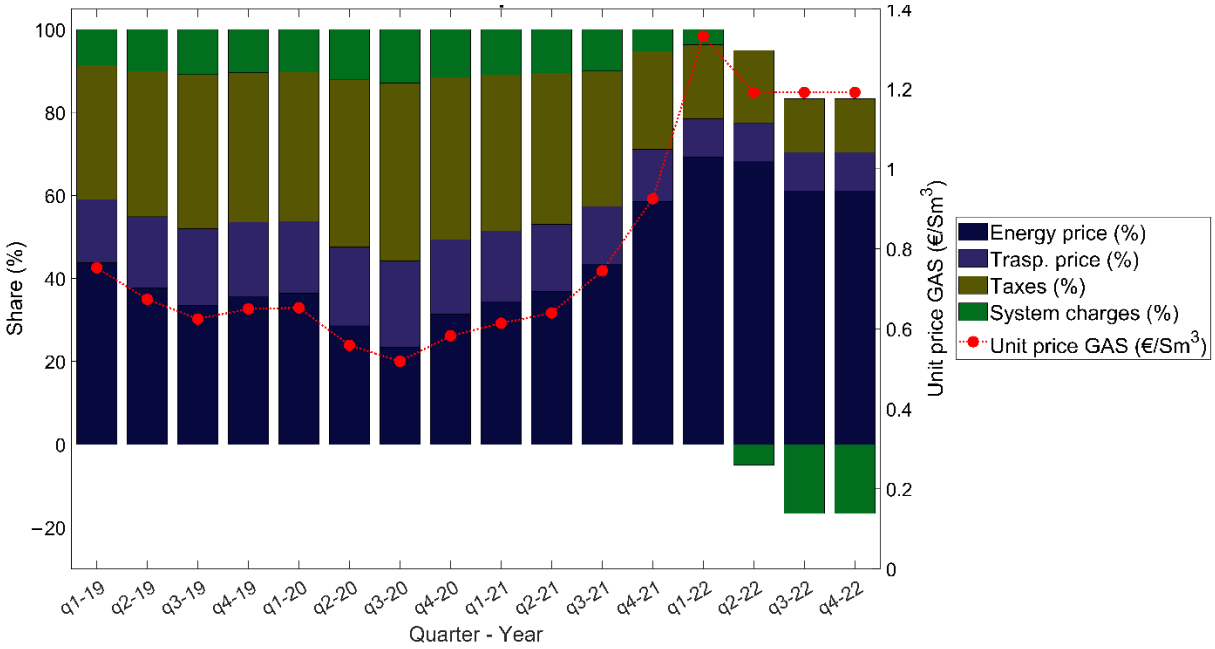

Figure 4.6 - Trends of the unit gas price (€/Sm³) and price components share as stated by the authority from first quarter of 2019 to the last quarter of 2022.

Turning attention to the unit price of natural gas over the past three years, **Figure 4.6** reveals a similar upward trend as witnessed with electricity, notably from the last quarter of 2021 through 2022, with prices rising from 0.745 €/Sm³ to 1.191 €/Sm³. For natural gas, the energy component and taxes were primary contributors to the overall cost until the third quarter of 2021. Subsequently, the energy component became the predominant factor. In response to escalating gas prices, the Italian government introduced two measures in the last quarter of 2021: a reduction in VAT on gas from 22% to 5% and the removal of system charges, at times even attributing them negative values as showcased in **Figure 4.6**.

Three pivotal aspects were taken into account when assessing unit gas prices and warrant brief elucidation:

- From October 2022, ARERA transitioned to a monthly review of gas prices for the standard-offer market to reflect market dynamics more accurately, particularly in light of the 2021 global energy crisis. For the economic assessment of the final two months of 2022, gas prices from October 2022 were used as a reference.
- The unit price of gas under the standard-offer market is contingent on the annual consumption volume by domestic consumers. ARERA has defined incremental consumption bands (with the 1st band for consumption up to 120 Sm³/year, the

2nd band from 121 to 480 Sm³/year, and the 3rd band from 481 to 1560 Sm³/year), which were incorporated into the economic analysis.

- In contrast to the uniform electricity pricing across Italy, the unit price for gas varies regionally due to divergent local taxations on natural gas. Typically, gas tends to be more affordable in northern Italy and pricier in the central and southern regions. This study took these regional price variances into account, with **Figure 4.7** depicting the distinct unit gas prices for Milan, Rome, and Naples.

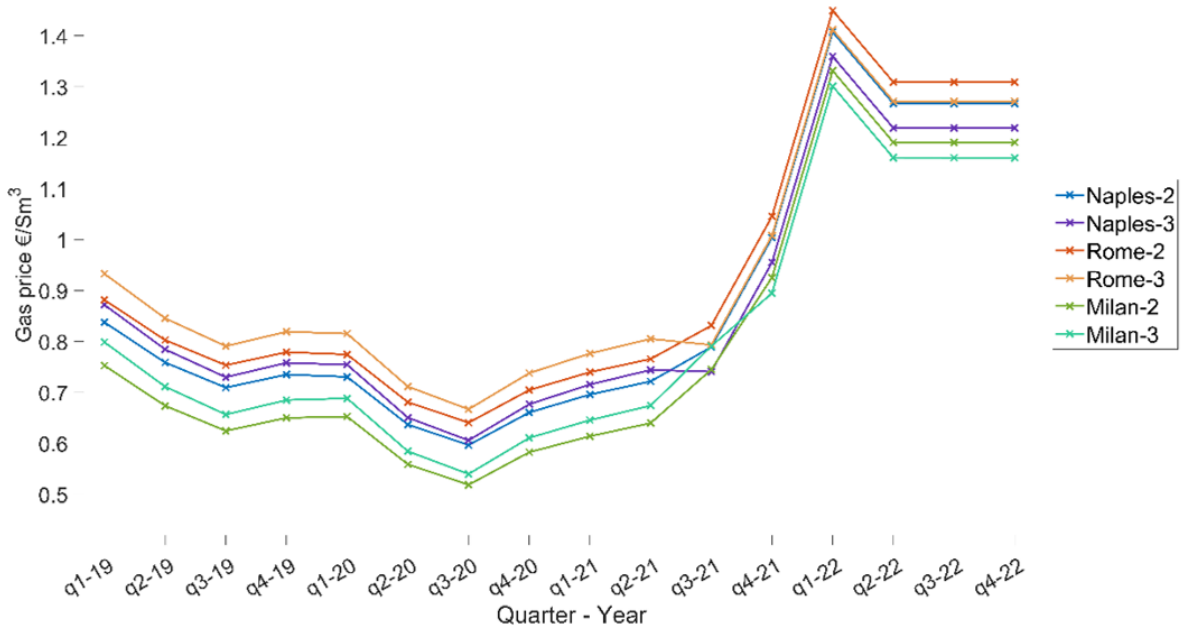

Figure 4.7 - Trends of unit gas price (€/Sm³) for Milan, Rome and Naples for the second and third consumption band (i.e for consumption between 121 and 480 Sm³ and 481 to 1560 Sm³ respectively).

4.5 Results and discussion

Table 4.4 - Results obtained by dynamic simulation.

Municipality	Building	Set Point	*ET* (kWh)	*EE* (kWh)	*SCOP* (-)	V_{gas} (Sm³)
Milan	RB1	SP1	11,045	3334	3.31	1321
		SP2	9741	2941	3.31	1165
		SP3	8844	2676	3.30	1058
	RB2	SP1	5977	1807	3.31	715

		SP2	5138	1569	3.27	615
		SP3	4599	1418	3.24	550
		SP1	2797	855	3.27	335
	RB3	SP2	2251	699	3.22	269
		SP3	1945	621	3.13	233
		SP1	6417	1786	3.59	739
	RB1	SP2	5208	1454	3.58	609
		SP3	4450	1251	3.56	523
		SP1	3052	857	3.56	358
Naples	RB2	SP2	2286	648	3.53	270
		SP3	1849	531	3.48	219
		SP1	1123	319	3.52	132
	RB3	SP2	739	213	3.46	86
		SP3	547	161	3.40	63
		SP1	6430	1796	3.58	752
	RB1	SP2	5232	1470	3.56	617
		SP3	4482	1269	3.53	530
		SP1	3014	850	3.55	356
Rome	RB2	SP2	2275	650	3.50	270
		SP3	1855	540	3.44	220
		SP1	1104	317	3.49	131
	RB3	SP2	725	212	3.42	85
		SP3	541	161	3.35	63

In **Table 4.4**, the results from the 27 simulations conducted are presented. Specifically, the table illustrates the thermal energy demand for heating (ET), the electrical energy needs of the heat pump (EE), and the amount of gas required if, instead of the heat pump, a gas boiler is used with an average seasonal efficiency of 0.88 and a lower heating value of 9.5 kWh/Sm^3 of gas.

Focusing on data from **Table 4.4**, is clear that a reduction of 1 K in the indoor temperature (comparing scenarios in SP2 to those in SP1) resulted in a decreased thermal energy demand for the building in all instances. Notably, the percentage reduction was more pronounced for buildings RB2 and RB3. For instance, the percentage decrease for RB1 in Milan was 12%, while it was 14% for RB2, and 20% for RB3. This

suggests that the most significant reductions were observed for buildings with a lower *EP* value (defined as the ratio between the annual thermal energy demand of the building and the building's reference floor area). Additionally, for the same building type, the reduction was more significant in milder climates (Rome and Naples) compared to Milan. For example, for building RB1 in Milan, the thermal energy demand reduction was 12%, but for Rome and Naples, it was 19%. A similar trend was observed for buildings RB2 and RB3 across the three climates.

When considering a 2 K reduction in the indoor set-point temperature, there was another notable decrease in thermal energy demand, especially for buildings RB2 and RB3 in milder climates. The percentage reduction for B1 in Milan was 20%, with the highest reduction seen for building RB3 in Rome and Naples, reaching up to 51%. Furthermore, when comparing the absolute difference in thermal energy between scenarios SP1 and SP2, building RB1 exhibited a larger reduction compared to buildings RB2 and RB3. For instance, the thermal energy demand for building RB1 in Milan under scenario SP1 was 1304 kWh/year less than under scenario SP2. In Rome, this reduction for RB1 was 1198 kWh/year, and in Naples, it was 1209 kWh/year. Hence, it can be inferred that the energy demand reduction in absolute terms was more pronounced for building RB1 in all the examined municipalities compared to buildings RB2 and RB3. Turning our attention to the SCOP of the heat pump, as expected, the SCOP was higher for heat pumps installed in milder climates (Rome and Naples) than in colder ones (Milan). SCOP values for Milan ranged between 3.13 and 3.31, while for Naples, they ranged from 3.40 to 3.59. Moreover, within the same municipality, the SCOP typically decreased for buildings with a lower EP and reduced thermal energy demand (B2 and B3). This trend may be attributed to the decreased efficiency of the heat pump, which undergoes on-off cycles due to the building's minimal energy demand.

Table 4.5 - Results obtained by economic analysis; yearly cost employing gas boiler (C_{GAS}) end employing heat pump (C_{HP}).

			2019		**2020**		**2021**		**2022**	
Municipality	**Building**	**Set Point**	***C*$_{GAS}$ (€/y)**	***C*$_{HP}$ (€/y)**	***C*$_{GAS}$ (€/y)**	***C*$_{HP}$ (€/y)**	***C*$_{GAS}$ (€/y)**	***C*$_{HP}$ (€/y)**	***C*$_{GAS}$ (€/y)**	***C*$_{HP}$ (€/y)**
Milan	RB1	SP1	979	674	854	510	986	661	1646	1735
		SP2	864	595	754	450	868	582	1454	1528

		SP3	784	541	684	410	787	529	1322	1390
		SP1	526	366	460	277	532	357	895	938
	RB2	SP2	452	318	395	241	457	309	771	814
		SP3	404	287	353	218	408	279	692	735
		SP1	242	173	212	131	248	168	423	443
	RB3	SP2	193	141	170	107	199	138	342	363
		SP3	166	126	146	96	172	123	296	323
		SP1	603	350	529	266	605	343	974	904
	RB1	SP2	495	288	435	219	499	283	804	746
		SP3	425	250	373	190	429	245	693	645
		SP1	288	171	254	130	294	167	477	440
Naples	RB2	SP2	216	130	191	99	223	127	363	335
		SP3	175	107	154	81	179	104	295	275
		SP1	105	64	93	48	108	62	178	163
	RB3	SP2	69	42	60	32	70	41	116	108
		SP3	50	32	44	24	51	31	85	81
		SP1	654	357	579	270	655	351	1026	923
	RB1	SP2	534	294	473	223	538	289	843	762
		SP3	458	255	406	193	463	251	726	661
		SP1	304	170	270	129	311	168	491	441
Rome	RB2	SP2	228	131	203	99	236	129	374	340
		SP3	185	109	164	83	192	107	306	282
		SP1	110	64	97	48	113	62	182	164
	RB3	SP2	72	42	64	32	74	41	119	109
		SP3	53	32	47	24	55	31	88	83

In **Table 4.5**, the annual costs for the two different heat generation systems are presented for the years 2019–2022. The data in this table was determined by multiplying the demand for electrical energy/natural gas by the corresponding unit value related to the location where the building was situated.

From an economic perspective, the heat pump was, in almost all scenarios, the more cost-effective generation system compared to the gas boiler. However, it's noteworthy that over time, especially in the last two quarters, there was a diminished economic advantage in using a heat pump instead of gas boiler.

References

[1]: ARERA Italian Regulatory Authority for Energy Networks and Environment. Prices and Rates in the Stand-ard-Offer Market (Electricity). Available online: https://www.arera.it/it/prezzi.htm (accessed on 28 September 2023).

[2]: Ballerini, V.; Rossi di Schio, E.; Valdiserri, P. How the Energy Price Variability in Italy Affects the Cost of Building Heating: A Trnsys-Guided Comparison between Air-Source Heat Pumps and Gas Boilers. Buildings 2022, 12, 1936, https://doi.org/10.3390/buildings12111936.

[3]: Klein, S.A.; Duffie, A.J.; Mitchell, J.C.; Kummer, J.P.; Thornton, J.W.; Bradley, D.E.; Arias, D.A.; Beckman, W.A.; Braun, J.E.; Urban, R.E.; et al. TRNSYS 17: A Transient System Simulation Program; University of Wisconsin: Madison, WI, USA, 2010.

[4]: Klein, S.A.; Duffie, A.J.; Mitchell, J.C.; Kummer, J.P.; Thornton, J.W.; Bradley, D.E.; Arias, D.A.; Beckman, W.A. TRNSYS 17—A TRaNsient SYstem Simulation Program, User Manual. Multizone Building Modeling with Type 56 and TRNBuild. Version 17.1; Uni-versity of Wisconsin: Madison, WI, USA, 2010.

[5]: Decree of Ministry of Ecological Transition n. 383 (Signed 6 October 2022). Available online: https://www.mite.gov.it/sites/default/files/archivio/comunicati/DM%20383%20del%206.10.2022%20-%20Riduzione%20riscaldamento.pdf (accessed on 28 September 2023).

[6]: ARERA Italian Regulatory Authority for Energy Networks and Environment. Prices and Rates in the Stand-ard-Offer Market (Electricity). Available online: https://www.arera.it/it/prezzi.htm (accessed on 28 September 2023).

[7]: ARERA Italian Regulatory Authority for Energy Networks and Environment. Prices and Rates in the Standard-Offer Market (Gas). Available online: https://www.arera.it/it/prezzi.htm (accessed on 28 September 2023).

[8]: ARERA Italian Regulatory Authority for Energy Networks and Environment. Annual Report on the State of Services and Regulatory Activity 2021 (Summary). 2021. Available online: https://www.arera.it/allegati/relaz_ann/21/Summary2021.pdf (accessed on 28 September 2023).

5 Influence of different heating system on thermal comfort perception: a dynamic, CFD and experimental analysis on a residential building.

In previous chapters, analyses were presented on heat pumps (air-sourced and geothermal), but the focus was never squarely on the comfort within buildings when using heat pumps for heating. This chapter introduces an analysis [1] concerning comfort in a residential building located in Bologna. The aim is to determine comfort indices (primarily the Predicted Mean Vote, *PMV*, and Predicted Percentage of Dissatisfied, *PPD*) and to discern the differences between using a gas boiler paired with cast iron radiators and an air-to-air heat pump. The study was conducted by determining the comfort indices using Trnsys and STAR-CCM+. The values obtained from the CFD simulations were validated by experimental measurements carried out in the analyzed apartment in Bologna.

5.1 Building analyzed

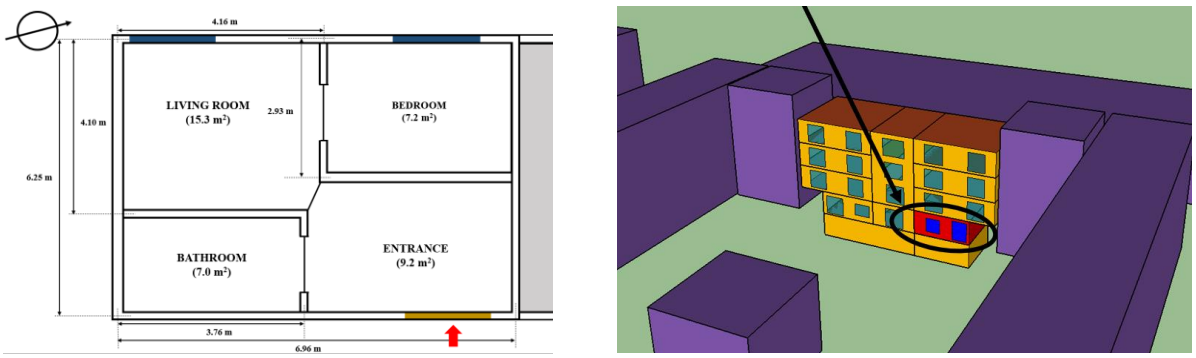

(a) **(b)**

Figure 5.1 – (**a**) Layout of the apartment (height: 3 m); (**b**) 3D view of the modelized building: the black arrow indicates the apartment analyzed, while the purple objects are nearby buildings and objects that shade the apartment.

The analysis focuses on an existing apartment situated on the ground floor of a four-story building located in the outskirts of Bologna. **Figure 5.1(a)** displays the apartment's layout, which spans an area of approximately 40 m^2, while **Figure 5.1(b)** provides a 3D representation of the modeled building used for dynamic simulations. As illustrated in **Figure 5.1(a)**, the apartment is divided into three distinct thermal zones: a combined kitchen-living room, a bedroom, and a bathroom. The unit has three external-facing walls, with the fourth wall adjoining the building's stairwell. The apartment's floor is positioned above garages, and its ceiling is directly below another residence.

Table 5.1 – Transmittance *U* and dimensions (thickness/area) of apartment envelope components.

Component	Thickness (m)	Area (m^2)	*U* ($W/(m^2K)$)
External walls	0.30	-	0.667
Dividing walls	0.10	-	2.047
Inter-floor	0.42	-	0.595
Entrance door	-	2.43	5.54
Window (bedroom)	-	1.89	1.69
Window (living room)	-	5.94	1.69

Table 5.1 lists the thickness and estimated transmittances of the walls surrounding the designated areas, as well as the dimensions and features of the windows and entrance door. The vertical external walls' structure comprises a 0.04 m layer of rockwool insulation sandwiched between two layers of hollow bricks. This configuration is typical of buildings constructed in the 1990s in Northern Italy, like the one in focus. A broader view of the building block housing the apartment can be seen in **Figure 5.2**, which also offers an aerial perspective of a section of the neighborhood. From the photos, other buildings surrounding the apartment are evident. These were modeled using Google SketchUp [**2**] to account for the shadows cast on the primary building. Within the entire building block, only the adjacent apartments and garages were modeled as thermal zones for the energy analysis. This is because they are the ones that can directly influence the targeted apartment. All other apartments or thermal zones were represented as extensions.

(a)

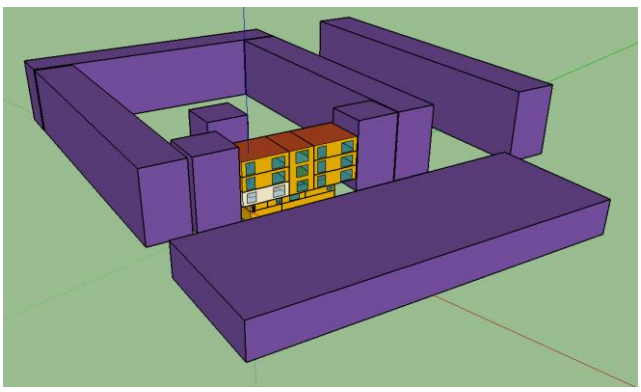

(b)

Figure 5.2 – (**a**) Aerial view of the building block analyzed and of surroundings; (**b**) extended view of the building block and shadings modelized for dynamic analysis.

5.2 Heating system

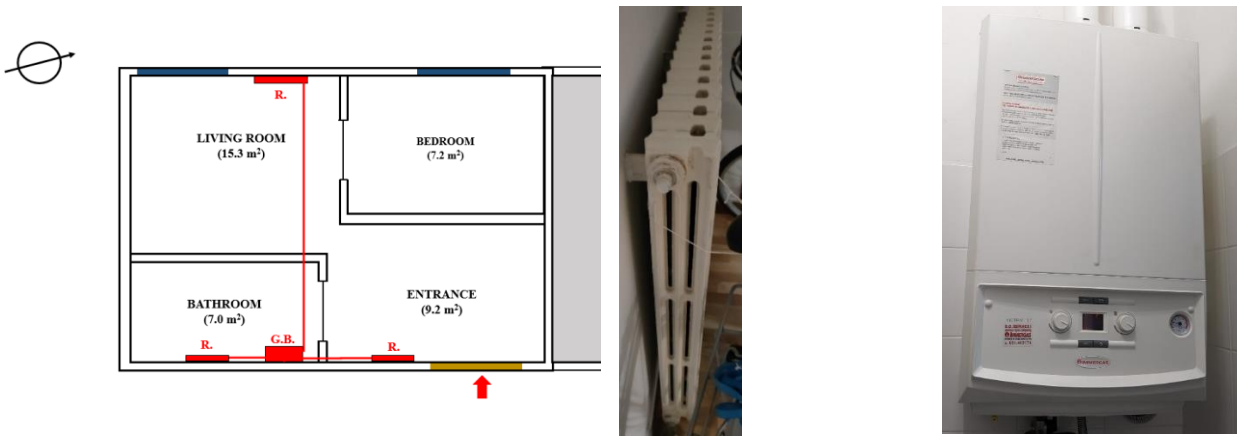

(a) **(b)** **(c)**

Figure 5.3 – Position of radiators (R.) and the gas boiler (G.B.) in the apartment (**a**); radiator positioned in the entrance (**b**) and gas boiler (**c**).

The initial heating system of the apartment features a gas boiler coupled with radiators (as seen in **Figure 5.3(b), (c)**) as the primary heat emitters. The apartment houses three radiators: one in the bathroom and two in the living room, located near the entrance door and the window, respectively. The positioning of these radiators within the apartment is illustrated in **Figure 5.3(a)**. While the gas boiler also facilitates domestic hot water production, its primary attribute is its 24 kW nominal power and a combined seasonal efficiency (for both heating and hot water) of 0.80. However, for the purposes of this analysis, the thermal energy demand for domestic hot water has been excluded.

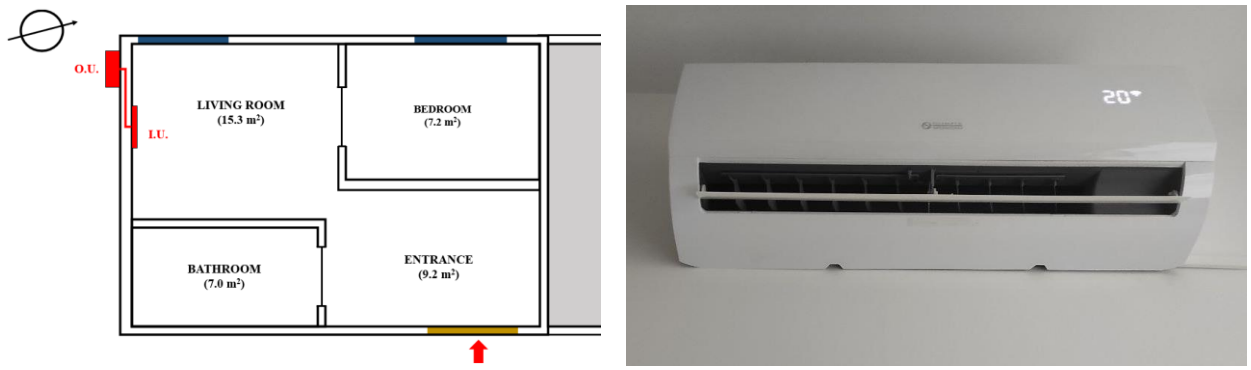

(a) **(b)**

Figure 5.4 – Position of the heat pump internal unit (I.U.) and external unit (O.U.) within the apartment (**a**); view of the heat pump internal unit (**b**).

In addition to the gas boiler, the apartment is equipped with an inverter air-to-air heat pump (shown in **Figure 5.4**), which has a singular internal unit stationed in the living room. Under rated conditions (internal air temperature of 20 °C and external temperature of 7 °C), the heat pump can achieve a maximum thermal power output of 3.5 kW. Its Coefficient of Performance (*COP*) and thermal power output (P_{th}) trends are depicted in **Figure 5.5**.

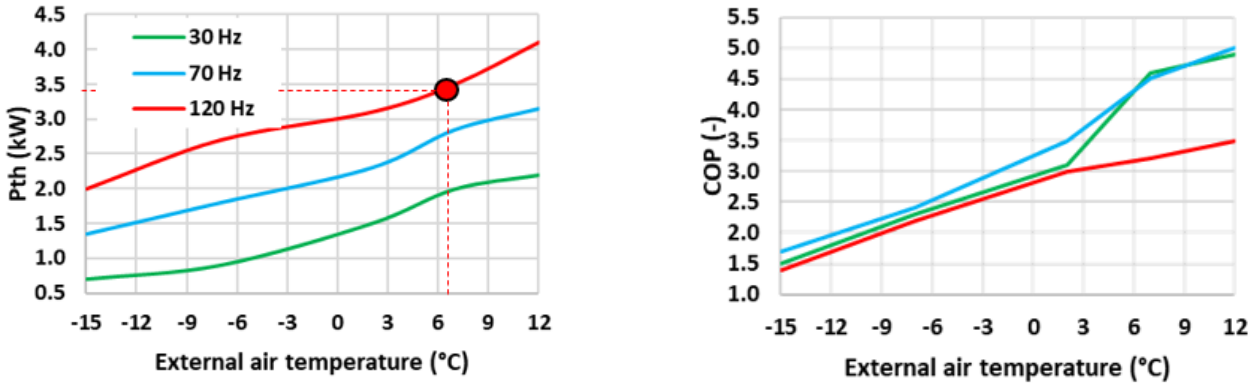

(a) **(b)**

Figure 5.5 – Thermal power output P_{th} (**a**) and *COP* (**b**) of the heat pump considered, for three different inverter frequencies and for a fixed indoor air temperature of 20 °C. The red dot indicates the thermal power output at rated conditions.

5.3 Dynamic analysis

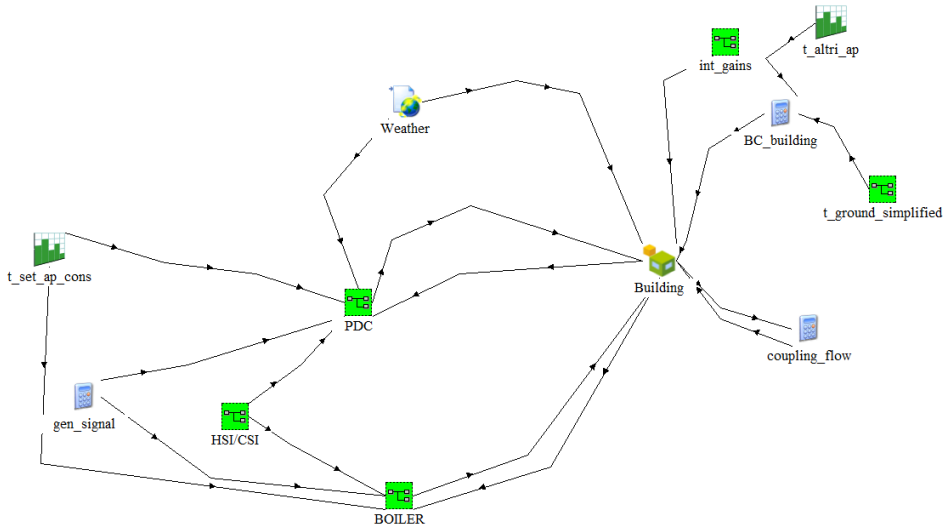

Figure 5.6 – Trnsys layout of the heating system as sketched in Trnsys.

Table 5.2 – Dynamic simulations performed. In case DS1 the emitters are the radiators, while in case DS2, DS3 and DS4 the emitter is the internal unit of the air-to-air heat pump.

Case	Heating generation system	Daily set-point, 6:00 am – 11:00 pm (°C)	Night set-point, 6:00 am – 11:00 pm (°C)
DS1	Gas boiler	20.5	17.5
DS2	Air-to-air heat pump	20.5	17.5
DS3	Air-to-air heat pump	21.5	17.5
DS4	Air-to-air heat pump	22.5	17.5

4 different dynamic simulations have been performed, as reported in **Table 5.2**. For all the simulations carried out, the same boundary conditions, have been considered. In particular, the air change rate of the thermal zones is reported in **Table 5.3**.

Table 5.3 – Air change rate of the zone.

Zone	Air change rate (h^{-1})
Kitchen, living room, bedroom (considered apartment)	0.6
Bathroom (considered apartment)	0.8
Other apartments	0.6
Garages	2

It can be noticed that the garages have a higher air change rate compared to other areas due to their large external openings. Similarly, the bathroom exhibits a greater air change rate than other sections of the apartment, attributed to its extractor fan. The temperature for the upper apartment, which is the only heated area adjacent to the apartment under consideration, is set at 20 °C during daytime hours (6:00 am – 11:00 pm) and drops to 17 °C at night (11:00 pm – 6:00 am). The temperatures for both the garage and stairwells are determined by the dynamic simulation software, as these zones are unheated. For garages on the ground floor, the ground temperature is gauged using typical thermophysical properties of the Bologna soil (with a conductivity of 1.8 W/(mK), density of 2800 kg/m^3, and thermal capacity of 0.85 kJ/(kgK)) [**3**]. Internal gains, related to electrical equipment and occupancy, are based on the standards set by IEA Task 44 [**4**], factoring in a single occupant. Latent internal gains, sourced from occupancy, cooking, equipment, and wet surfaces, are taken to be 0.25 kg/h, as specified by the UNI-TS 11300-1 standard [**5**] for residential structures. The apartment was modeled using Google Sketch-up and subsequently imported into Trnsys [**6, 7**] using the Trnsys3d plugin [**8**]. It's divided into 4 thermal zones (**Figure 5.1a**) instead of its actual three. Specifically, the kitchen-living room was divided into two distinct zones to facilitate a detailed calculation of the mean radiant temperature, considering view factors for each zone. For accuracy, all thermal zones should be convex; therefore, a virtual wall was implemented in Trnsys to separate the living/kitchen area from the entrance. Airflow coupling between the four zones (entrance, living room, bedroom, and bathroom) was ascertained using CONTAM [**9**], contingent on air density variations between zones. Radiators were represented in Trnsys using types 320 and 362 [**10**]. The simulation adopted a time-step of 15 seconds, and the analysis is confined to Bologna's standard heating period (15 October – 14 April).

Table 5.4 – Results obtained from the performed dynamic simulations: *ET* (kWh) refers to the thermal energy demand of the building, *EE* (kWh) is the electric energy demand of the heat pump and *SCOP* (-) is the Seasonal Coefficient of Performance of the heat pump.

Case	***ET* (kWh)**	***EE* (kWh)**	***SCOP* (-)**
DS1	3486	-	-
DS2	2669	872	3.03
DS3	2983	997	2.95
DS4	3303	1133	2.88

In **Table 5.4** are reported the results obtained from dynamic simulations for cases DS1 – DS4. Can be clearly observed the difference in thermal energy demand of the building in the case of radiators and heat pump. In **Figure 5.7** are shown the *PMV* and *PPD* for a representative day of the heating season, in which the mean outdoor temperature is 6.9 °C. The comfort indexes have been calculated considering a fixed air velocity of 0.1 m/s, a clothing factor of 1.1 clo and a metabolic rate of 1.1 Met.

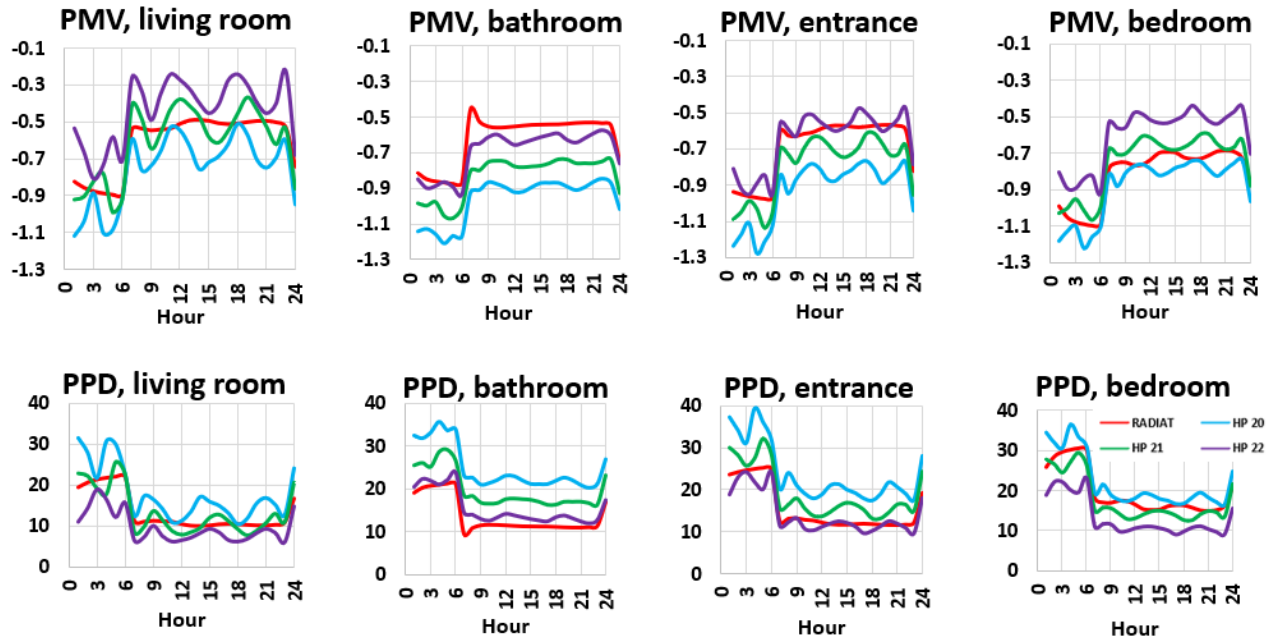

Figure 5.7 – *PMV* (-) and *PPD* (%) obtained by dynamic simulation for the 4 zones considered; the red line refers to case that considers radiators, while the other three lines refers to cases that consider the heat pump with different air temperature set – points.

From **Table 5.4** can be noticed the important reduction in terms of thermal energy demand in the case that consider the heat pump as generator instead of a gas boiler: the reduction in thermal energy demand of the building for case DS2 respect to case DS1 is 23 %, while there is a similar energy demand in cases DS1 and DS4, but in this latter case the heat pump has a set-point temperature of 22 °C during the day. The different thermal energy demand between the two different heating system is due primarily because the heat given by the heat pump has been modelized as a pure convective heating, while the heat given by the gas boiler (that has radiators as terminal emitters) is considered partly convective and party radiative.

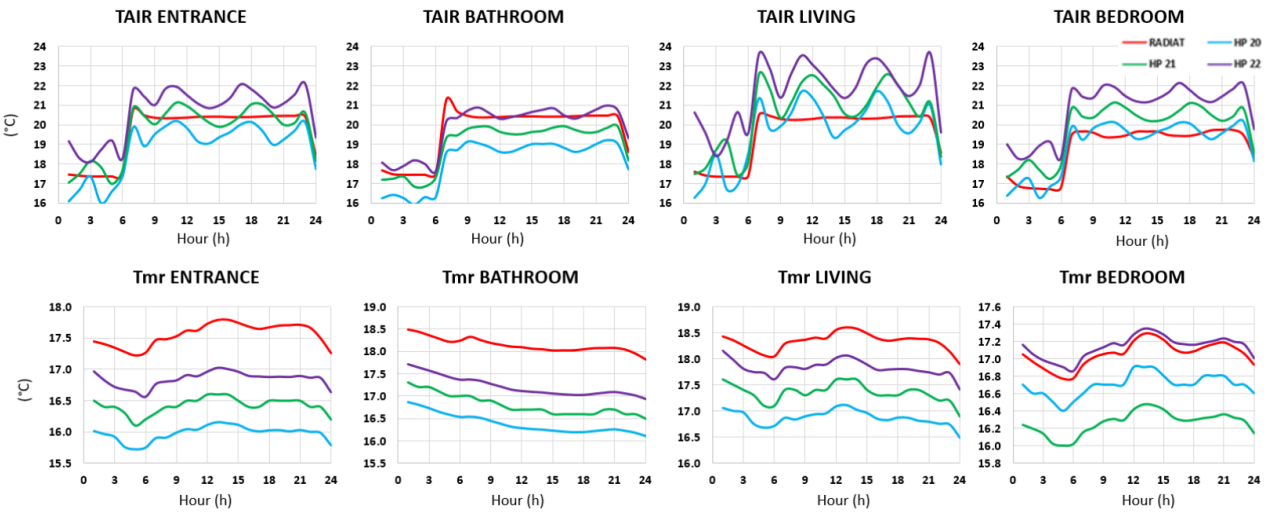

Figure 5.8 – Air temperature (TAIR) and mean radiant temperature (Tmr) for the four zones during the representative day of the heating season (daily mean outdoor air temperature of 6.9°C).

Opting for the heat pump over the gas boiler proves beneficial in terms of energy conservation. However, it compromises the comfort level within the apartment, as depicted in **Figure 5.7**. Notably, the *PPD* is elevated for scenario DS2 (heat pump with a 20°C day-time set-point) across all areas, excluding the radiator-devoid bedroom. A closer examination reveals that PPD levels between scenarios DS1 and DS4 are largely comparable across most thermal zones. This suggests that the heat pump can only match the comfort provided by a gas boiler paired with radiators when set to 22°C. Furthermore, comfort indices were evaluated on the season's chilliest day, with an average external temperature of -4°C. There's a significant deterioration in comfort levels, especially in scenarios employing the heat pump for heating. For instance, in scenario DS1, *PPD* values soar to 50% in the bedroom, entrance, and bathroom. In

comparison, scenario DS4 sees a modest decline in *PPD* (5-10%) relative to DS1, limited to the bedroom and living room. The most pronounced disparity between DS1 and its counterparts in comfort indices stems from the mean radiant temperature. On a representative heating season day with an average outdoor temperature of 6.9°C, DS1's mean radiant temperature in thermal zones outstrips the others by approximately 1-2 K (**Figure 5.8**). This discrepancy becomes even more pronounced on the coldest day of the heating season, with DS1's mean radiant temperature surpassing the others by as much as 3°C.

5.4 CFD analysis

The commercial software STARCCM+ [**11**] has been used to carry out a CFD analysis. The analysed governing equations consist of the mass (1), momentum (2), and energy (3) balance equations for steady state, incompressible, turbulent flows of an ideal gas, namely:

$$\nabla \cdot \vec{v} = 0 \tag{1}$$

$$\rho_0[(\vec{v} \cdot \nabla)\vec{v}] = -\nabla(\mathrm{p} + \rho_0 g z) + \rho_0 g \beta (T - T_0)\nabla \mathrm{z} + \nabla \cdot \tilde{\tau}_{eff} \tag{2}$$

$$\nabla \cdot \left(\vec{v}(\rho e + p)\right) = \nabla \cdot [(k + k_t)\nabla \mathrm{T}] + \tilde{\tau}_{eff} \cdot \vec{v} \tag{3}$$

where $\vec{v}$ is the velocity vector, p is the pressure, β is the thermal expansion coefficient, $\tilde{\tau}_{eff}$ is the effective stress tensor, e is the specific enthalpy, k is the thermal conductivity and k_t the turbulent thermal conductivity.

To effectively capture turbulence anisotropy, we employed the Reynolds Stress Transport (RST) turbulence model in tandem with the Elliptic Blending near-wall Reynolds-stress turbulence closure. The governing equations underwent discretization into an algebraic equation set using a second-order upwind scheme. For addressing the pressure-velocity coupling challenge, we implemented the semi-implicit method for pressure-linked equations (SIMPLE algorithm). Throughout the simulation, convergence was monitored by assessing residuals and observing velocity and temperature metrics at assorted points within the room.

A mesh sensitivity study was executed to strike a balance between computational efficiency and result accuracy. The finalized mesh encompassed 9 x 10^6 elements, featuring a foundational size of 4 cm. Boundary layer modeling incorporated 5 layers, amassing a cumulative thickness amounting to 5% of the base dimension. Surface enhancements were deemed essential for elements like the heat pump's internal unit, radiators, and room furnishings. **Figure 5.9a** depicts the spatial arrangement of

furniture within the apartment. Concurrently, **Figure 5.9(b)** provides an aerial perspective of the ultimate mesh applied to internal surfaces.

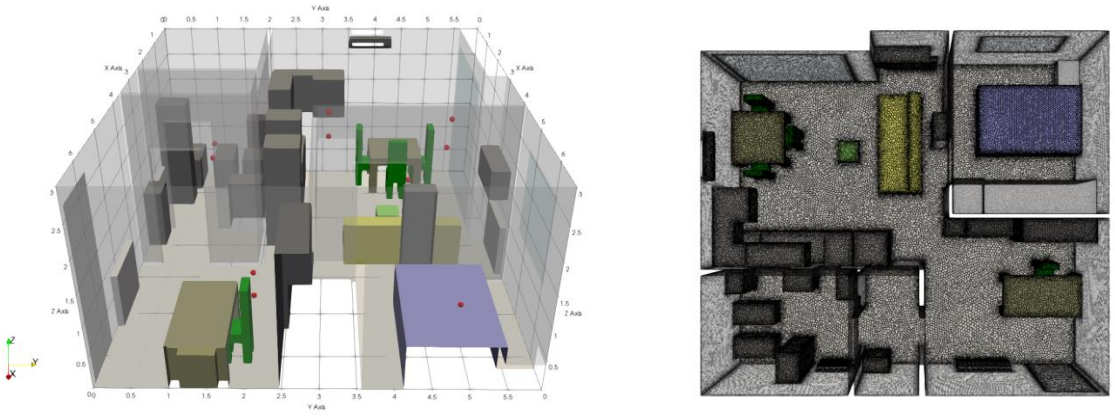

(a) **(b)**

Figure 5.9 – Furniture layout (**a**) and top view of the internal mesh (**b**).

Two distinct steady-state simulations were conducted to evaluate the performance of the two heating systems installed in the apartment on a typical winter day in Bologna, with an external temperature set at 6.9°C. The internal temperatures for the ceiling, floor, and the wall adjacent to the stair hall were maintained at 20°C, 10°C, and 12°C respectively. The heat pump's internal unit features an inlet with a prescribed velocity of 2.4 m/s, in line with measurement performed when the heat pump was switched on in the apartment, and discharges at a 45° angle to the ceiling. The outlet section operates under a pressure outlet boundary condition. In contrast, radiators are represented as heat sources, achieving a surface temperature of 60°C. Simulation outputs informed the assessment of global thermal comfort indices, specifically the *PMV* and its associated *PPD*, within the apartment. **Figure 5.10** visualizes the distribution of *PMV* and *PPD* values across the apartment, highlighting the contrasting thermal comfort landscapes created by the two heating systems. Indeed, the spatial distribution of parameters vital for *PMV* evaluation varies noticeably between the two setups. As depicted in **Figure 5.11**, the streamlines corresponding to the heat pump align with the 45° discharge angle, directing towards the sofa region. Influenced by buoyancy, the airflow then ascends and moves into the bedroom. Consequently, the bathroom and entrance receive a diminished share of warm air, compromising comfort in these zones. This dynamic shifts when radiators serve as the heat source. Their

presence enhances the distribution of mean radiant temperature within the apartment, culminating in a distinctively different comfort profile.

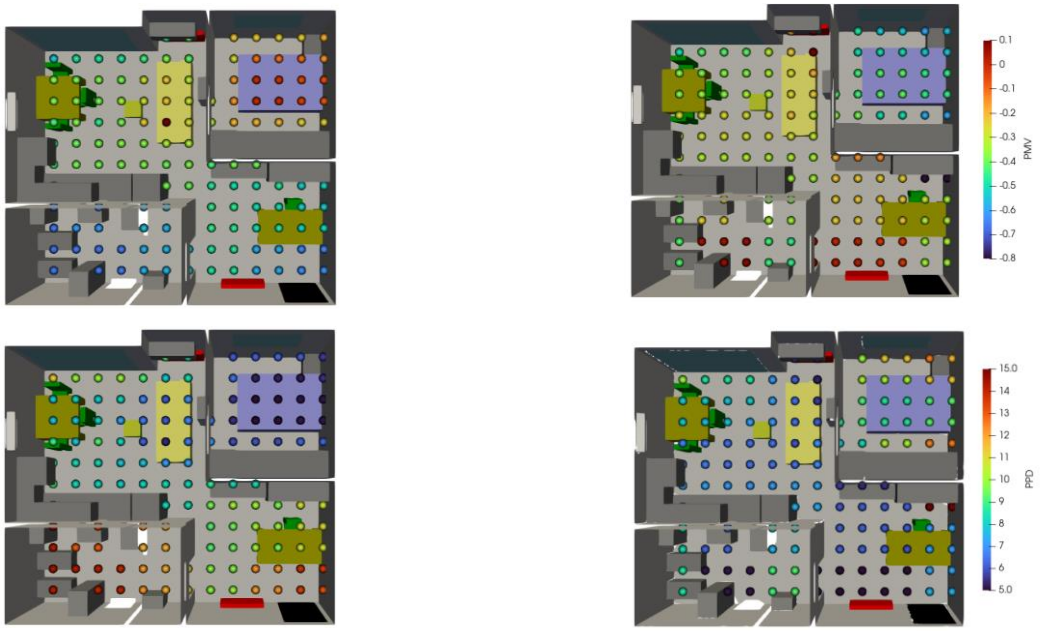

(**a**) (**b**)

Figure 5.10 – Top view of *PMV* (upper figures) and *PPD* (lower figures) distribution for heat pump (**a**) and radiators (**b**).

The CFD analysis highlights contrasting comfort levels associated with the two heating systems. For instance, deploying the heat pump yields near-zero *PMV* values in the bedroom. However, reduced *PMV* values are discernible in both the bathroom and entrance areas (as seen in **Figure 5.10**). Additionally, the pronounced velocity and temperature of the air expelled from the heat pump might create zones of discomfort, with warm thermal streams directly impacting the sofa in the living room. On the other hand, employing radiators fosters a more consistent *PMV* distribution throughout the apartment. This consistency stems from the strategic placement of the terminals, leading to elevated *PMV* values in the bathroom and entrance when compared to the heat pump mode. Nonetheless, this enhancement detracts from the thermal comfort in the bedroom, where the *PMV* values dip considerably, a consequence of lacking a radiator and having a large window.

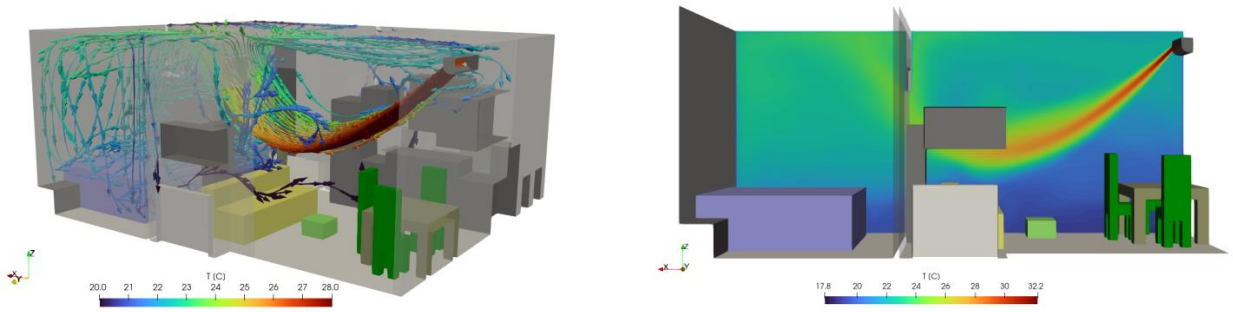

(**a**) (**b**)

Figure 5.11 – Streamlines of the heat pump discharged air (**a**) and temperature profile (**b**) along a section in correspondence of the heat pump internal unit.

5.5 Experimental measurements

In this section, the experimental measurements conducted in the apartment will be briefly presented. These measurements primarily served to establish boundary conditions for the CFD analysis and to validate the model. Specifically, temperature and mean radiant temperature values were determined at various points within the thermal zones. The exit velocity of the air from the internal unit of the heat pump was also measured (measured velocity of 2.4 m/s). Measurements were taken using a thermal camera. **Figure 5.12(a)** displays a thermographic image of the air conditioner's internal unit, where the outlet temperature is observed to be approximately 33°C. Below the split unit, the presence of a pillar can be noticed, where the wall's surface temperature is considerably lower (about 15°C) than the rest of the wall. **Figure 5.12(b)**, on the other hand, presents an image of the radiator located in the living room; it can be observed that when operational, the surface temperature reaches values close to 60°C.

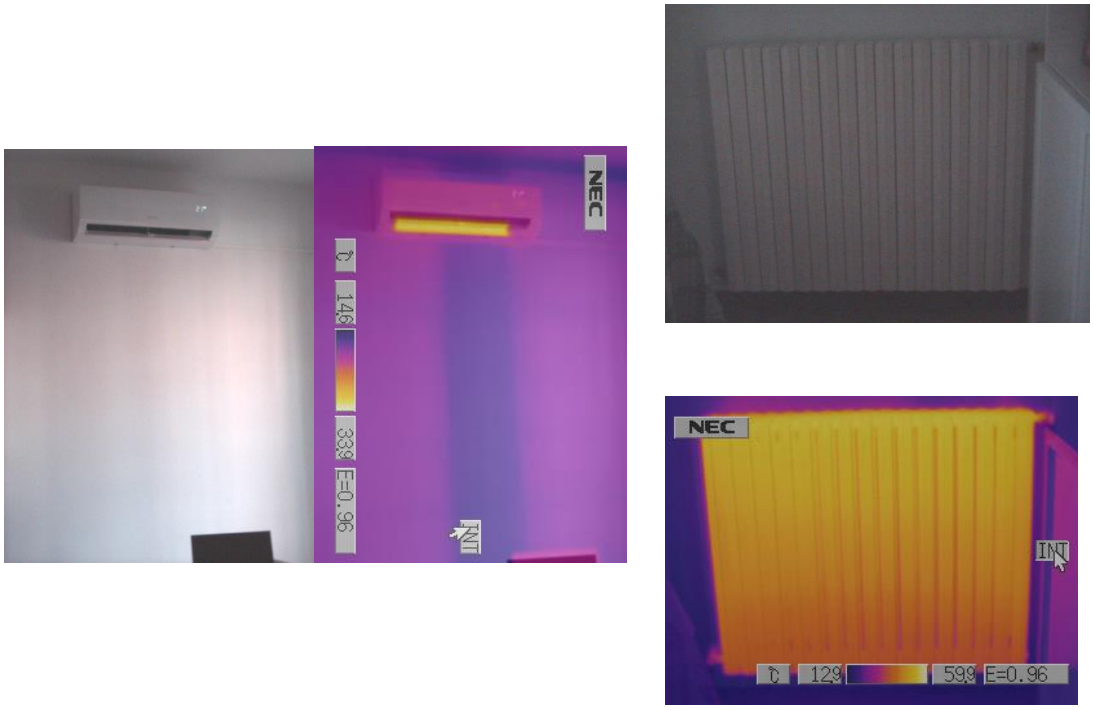

(**a**) (**b**)

Figure 5.12 - Thermographic images of the heat pump's internal unit (**a**) and the radiator located in the living room (**b**).

The inspections conducted using the thermal camera allowed for the identification of thermal bridges due to pillars (**Figure 5.13a**) and in the vicinity of window and door frames (**Figure 5.13b**). However, the presence of these colder areas of the building envelope was not taken into account in the CFD analysis or in the dynamic analysis. In

both cases, an average surface temperature of the walls and, more generally, of the envelope elements was considered.

(**a**) (**b**)

Figure 5.13 - Thermal bridge due to the presence of a pillar (**a**) and thermal bridge at the window in the living room (**b**).

5.6 Comparison between CFD and dynamic analysis and key findings

When comparing the results from both the CFD and dynamic analysis, they both converge to similar conclusions: the use of an air-to-air heat pump leads to a deterioration of indoor comfort compared to using a gas boiler coupled with radiators.

While the outcomes from the two analyses align qualitatively and generally, the quantitative values differ. This variation can be attributed to the distinct calculation methods for comfort indices: dynamic analysis determines comfort at a specific point (or possibly multiple points) throughout the heating season for each thermal zone, yielding an hourly PMV value. In contrast, CFD analysis provides a spatially distributed *PMV* value at different building points but at a specific moment in time (running a time-dependent CFD simulation would demand significantly more computational effort and time). Both methods offer an accurate estimation of comfort within thermal zones, with values potentially being a function of time (dynamic analysis) and space (CFD analysis). CFD is particularly beneficial for information on potential local discomfort, while dynamic analysis provides a holistic perspective on comfort within thermal zones.

The primary insights from this analysis are as follows:

- Utilizing an air-to-air heat pump in place of a gas boiler results in significant energy savings for the building, reaching up to 23%.
- As identified by the dynamic simulation, the comfort perception inside the considered apartment is worse when using a heat pump instead of a gas boiler with radiators, particularly during the colder days of the heating season.
- The subpar comfort indexes, especially on colder days, are mainly attributed to the reduced mean radiant temperature when deploying the heat pump instead of radiators.
- The CFD analysis indicates that while the air-to-air heat pump system can yield satisfactory *PMV* values in the living room and bedroom, it falls short for the bathroom and entrance areas. Additionally, the high velocity and temperature of the expelled air might cause local discomfort for the occupants. To enhance the overall thermal comfort across the apartment, the position of the internal unit could be modified, or an auxiliary unit could be introduced to cater to areas with lower *PMV* values.
- Radiators, as depicted by the CFD simulation, offer a more uniform distribution of internal thermal parameters within the apartment, leading to a more comfortable experience for the inhabitants.

The conducted comfort analysis can serve as a foundation for optimizing indoor comfort, suggesting potential interventions such as repositioning the heat pump's internal unit or incorporating an additional internal unit.

References

[1]: Ballerini V., Palka Bayard de Volo E., Pulvirenti B., Rossi di Schio E., Valdiserri P., Guidorzi P., Influence of different heating systems on thermal comfort perception: a dynamic and CFD analysis, Proceedings of the 40th UIT International Conference, June 26 -28 2023, Assisi (Italy, IT)

[2]: SketchUp Trimble Inc., Google SketchUp Make 2015, https://www.sketchup.com/it (Accessed online 29 September 2023).

[3]: Natale, C.; Naldi, C.; Dongellini, M.; Morini, G.L. Dynamic Modelling of a Dual-Source Heat Pump System through a Simulink Tool. J. Phys.: Conf. Ser. 2022, 2385, 012090, https://doi.org/10.1088/1742-6596/2385/1/012090.

[4]: Dott, R.; Haller, M.; Ruschenburg, J.; Ochs, F.; Bony, J. IEA-SHC Task 44 Subtask C Technical Report: The Reference Framework for System Simulations of the IEA SHC Task 44/HPP Annex 38: Part B: Buildings and Space Heat Load. IEA-SHC. 2013. http://www.taskx.iea-shc.org/data/sites/1/publications/T44A38_Rep_C1_B_ReferenceBuildingDescription_Final__Revised_130906.pdf (Accessed online 29 September 2023).

[5]: UNI/TS 11300-part1, ENERGY PERFORMANCE OF BUILDINGS - PART 1: EVALUATION OF ENERGY NEED FOR SPACE HEATING AND COOLING, 2014 Edition, October 2, 2014

[6]: A: Klein, S.A. et al, 2017, TRNSYS 18: A Transient System Simulation Program, Solar Energy Laboratory, University of Wisconsin, Madison, USA, http://sel.me.wisc.edu/trnsys (Accessed 24 February 2023).

[7]: Klein, S.A.; Duffie, A.J.; Mitchell, J.C.; Kummer, J.P.; Thornton, J.W.; Bradley, D.E.; Arias, D.A.; Beckman, W.A.; TRNSYS 17—A TRaNsient SYstem Simulation Program, User Manual. Multizone Building Modeling with Type 56 and TRNBuild. Version 17.1; University of Wisconsin: Madison, WI, USA, 2010.

[8]: TRNSYS3D - plugin for SketchUp, http://www.trnsys.com/features/suite-of-tools.php.html (Accessed online 24 February 2023).

[9]: Contam Dols, W. and Polidoro, B. (2020), CONTAM User Guide and Program Documentation Version 3.4, Technical Note (NIST TN), National Institute of Standards and Technology, Gaithersburg, MD, https://doi.org/10.6028/NIST.TN.1887r1,

https://tsapps.nist.gov/publication/get_pdf.cfm?pub_id=930691 (Accessed September 29, 2023)

[10]: Holst, S. TRNSYS-Models for Radiator Heating Systems, 1996; http://trnsys.de/static/641c965bac4f593c3b4cc569839a51c2/Type_361_362_320_en.pdf (Accessed 29 September 2023).

[11]: CD-adapco. (2022). STAR-CCM+ [Software]. https://www.cd-adapco.com.

6 Carbon dioxide emissions of a heat pump connected to Italian power grid

Heat pumps can play a pivotal role in the decarbonization process since they typically utilize electricity, which is versatile and can be sourced from renewable energies. In the preceding chapters, we delved into the performance of heat pumps through experimental and dynamic analyses, examining the influence of climate on machine performance and the comfort achieved using heat pumps compared to boilers. This chapter will shift its focus to the environmental facets of heat pumps. Specifically, we aim to quantify the carbon dioxide emissions emitted by a heat pump serving a residential building powered by electricity from the Italian national grid, which consists of both renewable and non-renewable sources. Beyond analyzing the environmental impact of a heat pump, a new model for estimating hourly CO2 emissions due to electricity use in Italy will be introduced. Italy, distinct from other countries, has a pronounced energy dependence in terms of electricity from other European nations; in fact, a non-negligible part of electricity used in Italy is imported. To determine carbon dioxide emissions more accurately from electricity consumption in Italy, it is crucial to consider the amount of electricity imported from abroad. Following this, we will present a model estimating emissions derived from electricity usage in Italy (understood as electricity wholly sourced from the national grid) and subsequently conduct an analysis related to the energy demand of a heat pump serving a residential building [**1-2**].

6.1 Data and models for carbon dioxide emissions estimation

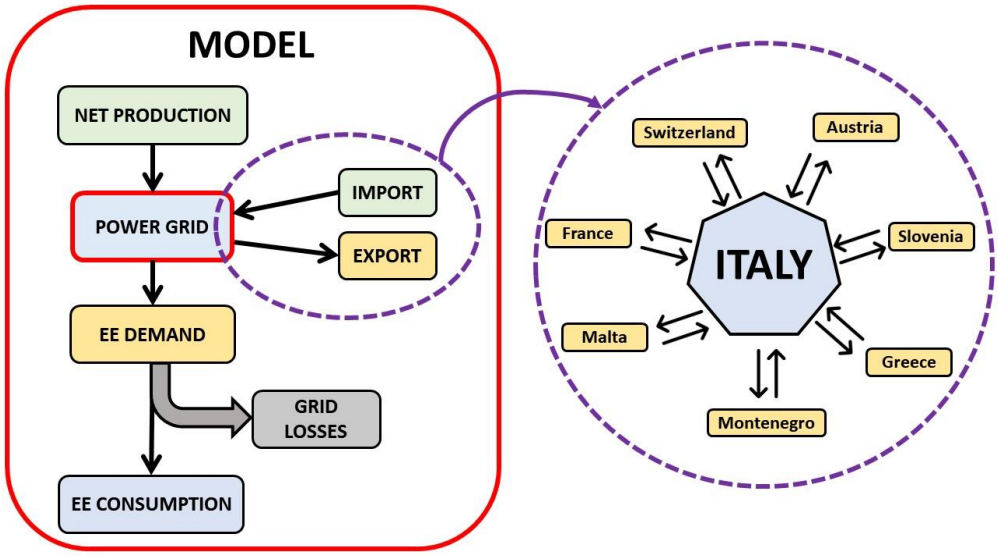

Figure 6.1 – Scheme related to the new model for the estimation of the hourly emission factors.

Before estimating the emissions from a heat pump, a new model will be introduced to determine the hourly emissions associated with the energy drawn from the Italian national electrical grid, accounting for both imported and exported electricity. All electrical grids in Europe are interconnected, meaning that the electricity consumed at any given hour in one country might be produced in another European nation. In this context, for instance, the electricity produced in Italy can directly influence the emissions of another country, which invariably has a different carbon emission factor due to its unique power production mix compared to Italy's. While various models in literature estimate hourly CO2 emission factors, most of them only consider domestically produced electricity, overlooking foreign exchanges. This approach is limiting for Italy, given its significant electricity imports from other countries, often exceeding 10% of its total national demand. After introducing the model, we'll derive hourly factors and subsequently approximate functions to provide hourly emission factor values (calculated by relating the CO2 produced in kg to the electricity drawn from the grid in kWh).

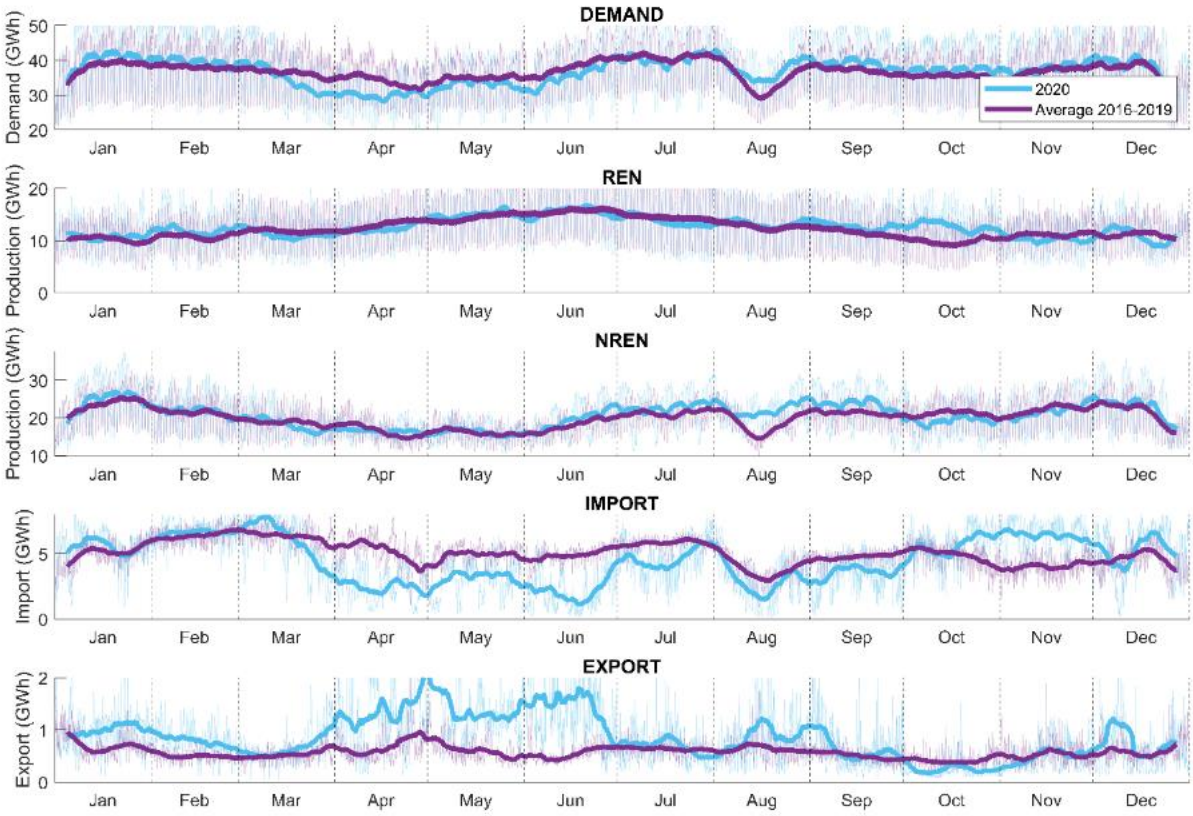

(**a**)

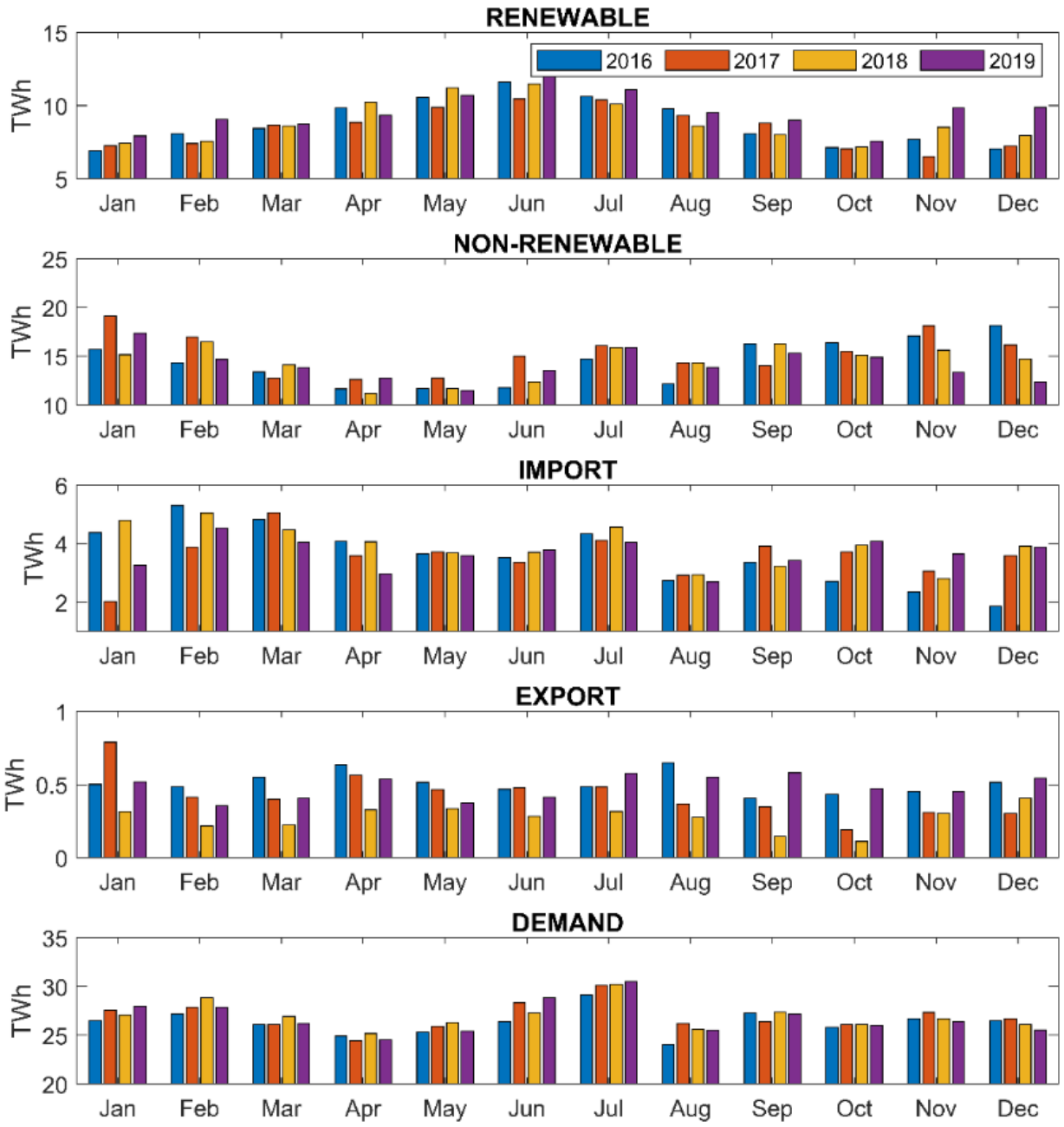

(**b**)

Figure 6.2 – Electricity demand, import, export, renewable (REN) e non – renewable (NREN) production for years 2016 – 2020 (**a**) and focus on monthly values (**b**) for years 2016 – 2019. In (**a**) the bold lines refers to a moving average over 200 h.

Figure 6.1 presents a schematic for estimating emissions. The proposed models require two data sets:

- Electricity production in Italy and its exchanges with other countries;

- Carbon dioxide emission factors for Italy (divided by different sources) and annual emission factors for other countries that trade energy with Italy.

Data regarding energy production and exchanges are sourced from Terna, the Italian Transmission System Operator. Specifically, hourly energy production data from 2016 to 2020 are collected [**3**] and categorized into geothermal, hydroelectric, photovoltaic, biomass, wind source, thermal (non-renewable), and self-consumption. Hourly data on energy exchanges with foreign countries for the same period (2016-2020) are also gathered, detailing the amount of energy imported or exported for the countries depicted in Figure 6.1 (Austria, France, Switzerland, Greece, Slovenia, Malta, and Montenegro). However, data concerning electricity exchanges with Montenegro are excluded, primarily because, as indicated by Terna's platform, exchanges between Montenegro and Italy commenced only from December 27, 2019.

Table 6.1 – Annual electric energy demand, import and export: comparison between year 2020 and the annual average of the years 2016-2019.

	2016-2019	**2020**	**% (2020 vs mean 2016-2019)**
Electricity demand (GWh)	321219	322584	+0.4
Electricity exported (GWh)	5060	7548	+49.2
Electricity imported (GWh)	44274	32155	-27.4

In **Figure 6.2(a)**, data related to renewable and non-renewable energy production, as well as energy imports, exports, and demands of the Italian power grid from 2016 to 2020, sourced from Terna, are depicted. Additionally, **Figure 6.2(b)** showcases monthly values of electricity demand, production, and exchange for the years 2016-2019. Analyzing renewable energy production on an annual basis for the five-year span, the peak production consistently occurs in the summer months, particularly June and July, while production tends to dip during the autumn and winter. For non-renewable sources, the lowest production values are observed in April and May. August sees a reduction in electricity imports, likely due to summer holidays and the resulting drop in Italian factory production. Notably, across all five years, Italy's electricity imports exceed its exports. The year 2020, marked by the outbreak of the Covid-19 pandemic, exhibited unique patterns. Specifically, during the months impacted by lockdowns and

reduced factory activity (parts of March, April, May, and the first two weeks of June), there was a noticeable decline in electricity demand compared to the previous four years. However, during this period, energy production from both renewable and non-renewable sources remained consistent with past patterns. The most significant change in 2020 compared to prior years was in electricity trading with foreign countries: during Italy's 2020 lockdowns and restrictions, there was a surge in electricity exports and a substantial decrease in imports, as detailed in **Table 6.1**.

Figure 6.3 depicts the electricity production from various renewable sources, including photovoltaic, wind, hydropower, geothermal, and bio-energies. From this illustration, it's evident that hydropower and photovoltaic contribute the largest portions, while geothermal energy plays a minimal role. Additionally, **Figure 6.3** highlights that peak production from photovoltaic sources for both 2016 and 2019 occurs in June and July, months known for their high solar irradiance and extended daylight hours in Italy. Examining hydropower reveals its highest production in June. In contrast, energy outputs from biofuels and geothermal sources remain relatively steady throughout the year. Lastly, the figure underscores the variability of wind energy, which, among all renewable sources considered, displays the most fluctuation, with notably lower outputs during the summer months.

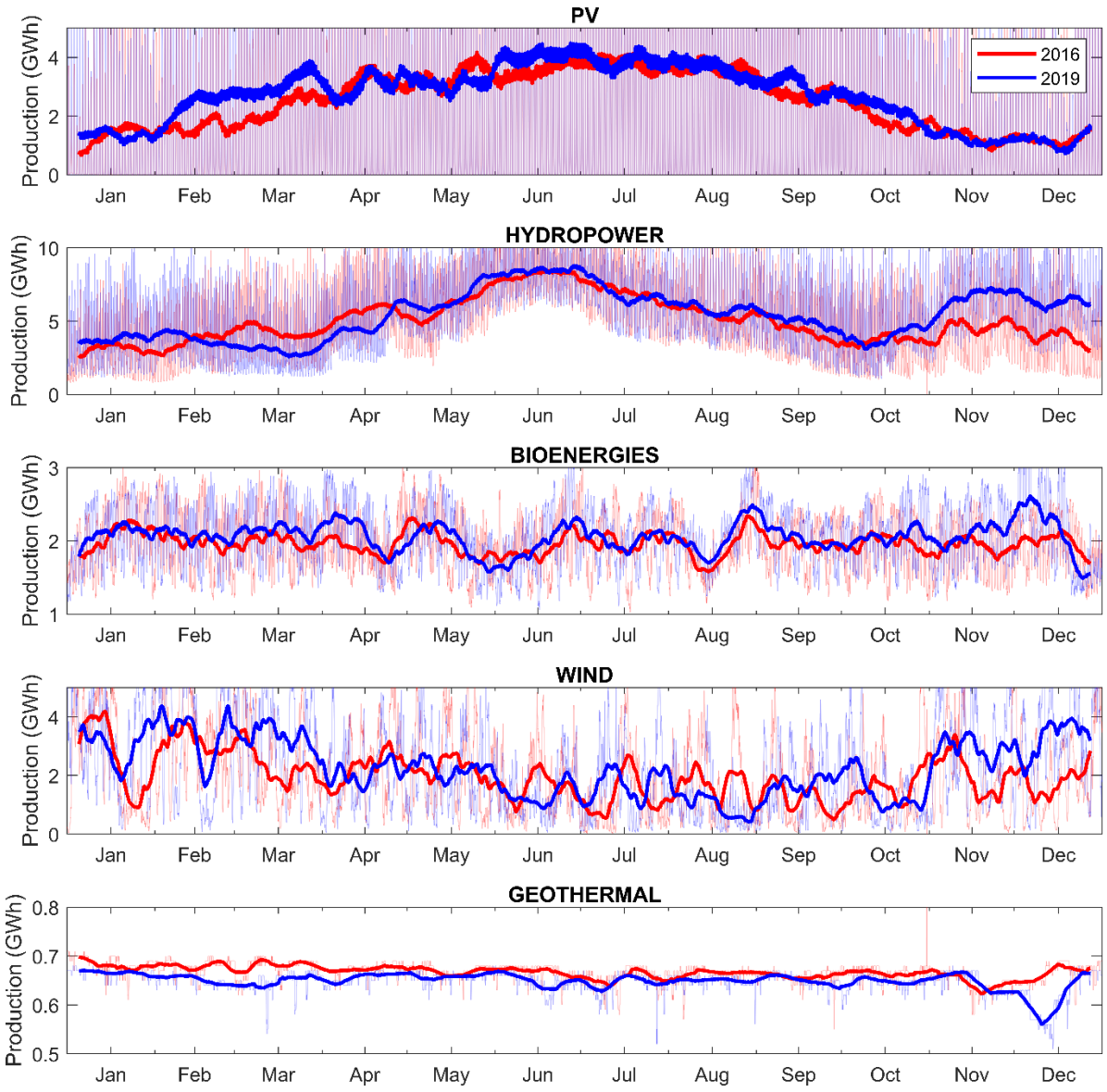

Figure 6.3 – Annual renewable production in Italy by source: photovoltaic (PV), wind, geothermal, hydropower and bio-energies.

Zooming into more granular time frames as depicted in **Figure 6.4**, we can discern that hydropower, and to some extent biofuels, mirror the typical daily electric energy demand patterns in Italy, characterized by two distinct peaks—one in the morning and another in the evening. This characteristic behavior stems from the controllability of these energy sources. Specifically, the ability to manage hydropower generation is facilitated by pumped storage systems, which enable electricity production to align with the daily demand surges. On the other hand, wind and photovoltaic sources, as presented in **Figure 6.4**, lack such programmability. The wind energy profile is notably erratic, while photovoltaic generation exhibits a consistent daily pattern, peaking around

midday. Additionally, it's worth noting the 24-hour periodicity evident in the generation trends for photovoltaic, biofuels, and hydropower.

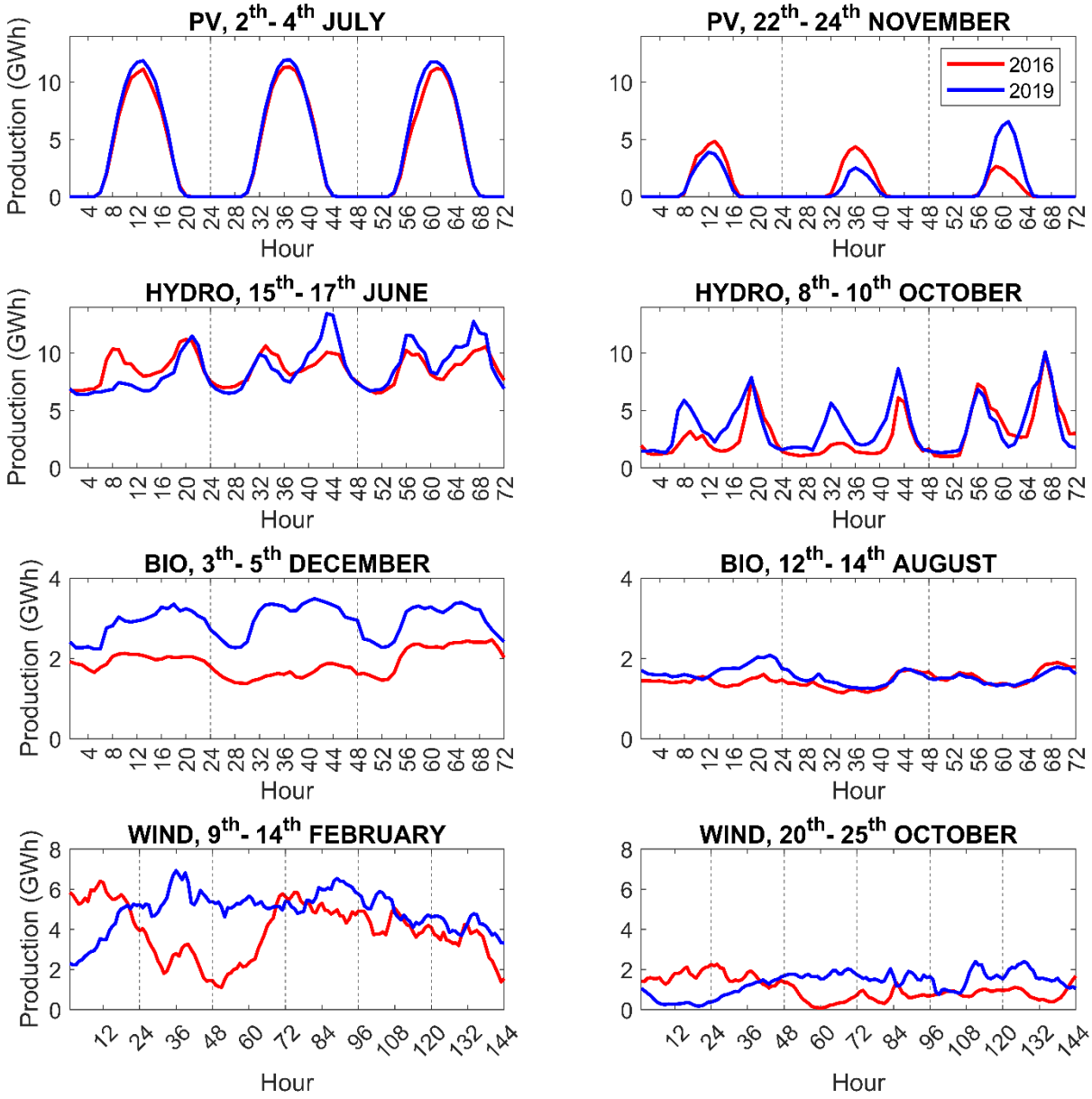

Figure 6.4 – Focus on renewable energy production in Italy for different days of the year.

Emission factors for non-renewable production in Italy used in this study are sourced from the annual report of ISPRA (Italian Institute for Environmental Protection and Research) [4]. **Table 6.2** lists these factors for a span of four years (2016-2019) and includes the annual emission factors for foreign countries connected to the Italian power grid, as provided by the annual AIB (Association of Issuing Bodies) report [5]. Information regarding the specific sources of imported electricity (e.g., categorized as renewable or non-renewable) is absent. Consequently, a mean annual emission

factor as suggested by [6] has been adopted for the electricity imported from other countries. This approach to incorporate imported electricity in the model, even while utilizing a constant annual emission factor for such imports, stems from recognizing the significant proportion of electricity consumed in Italy that originates from external nations. Emission factors for renewable sources are extracted from [7], with values (in kg/kWh) as follows: 0.230 for bio-energies, 0.038 for geothermal, 0.024 for hydroelectric, 0.045 for photovoltaic, and 0.011 for wind production. It's noteworthy that emission factor values for the year 2020, specifically for Italian non-renewable production, were not available from ISPRA at the time of this study, hence the analysis is confined to the years 2016 to 2019.

Table 6.2 – Emission factors expressed in kg/kWh for Italian non-renewable production and for electricity imported from other Countries.

Country	2016	2017	2018	2019
Austria	0.245	0.148	0.142	0.133
Corsica	0.045	0.053	0.047	0.039
France	0.045	0.053	0.047	0.039
Greece	0.574	0.620	0.567	0.549
Malta	0.668	0.761	0.761	0.371
Slovenia	0.427	0.348	0.335	0.244
Switzerland	0.087	0.016	0.014	0.012
Italy (non-renewable)	0.516	0.491	0.494	0.473

Two models will be introduced for determining hourly emissions: the first model, termed the "detailed model", provides hourly emission factor values EF_h (kgCO2/kWh) for every hour of the calendar year. The simplified model, or "simplified model", offers a function that yields the emission value based on the hour of the year. We will now delve into the detailed model, outlining the procedure for determining the hourly factors. The mass of carbon dioxide produced hourly from non-renewable electricity production in Italy can be denoted as $m_{nren,h}$ (kg), from renewable electricity production in Italy as $m_{ren,h}$ (kg), and from electricity imported from abroad as $m_{imp,h}$ (kg):

$$m_{nren,h} = EE_{nren,h} \cdot EF_{nren} \quad (1)$$

$$m_{ren,h} = \sum_j EE_{ren,j,h} \cdot EF_j \quad (2)$$

$$m_{imp,h} = \sum_k EE_{imp,k,h} \cdot EF_k \quad (3)$$

The hourly carbon dioxide production due to internal electricity generation in Italy is the sum of hourly renewable and non-renewable and import from foreign Countries, and is expressed by $m_{int+imp,h}$ (kg):

$$m_{int+imp,h} = m_{imp,h} + m_{ren,h} + m_{nren,h}, \quad (4)$$

The sum of hourly electric energy production in Italy and hourly import from abroad, namely $EE_{int+imp,h}$ (kWh), can be expressed as

$$EE_{int+imp,h} = \sum_k EE_{imp,k,h} + \sum_j EE_{ren,j,h} + EE_{nren,h} \quad (5)$$

Where $EE_{imp,k,h}$ (kWh) refers to the hourly electricity imported for the k-th country (reported in **Figure 6.1**). On account of eqs. (4-5), the hourly mass of carbon dioxide $m_{exp,h}$ (kg) related to hourly electricity exported $EE_{exp,h}$ (kWh), can also be expressed as

$$m_{exp,h} = m_{int+imp,h} \cdot \frac{EE_{exp,h}}{EE_{int+imp,h}} \quad (6)$$

Other useful quantities to determine the expression of the hourly emission factor are the hourly total mass of carbon dioxide emission $m_{tot,h}$ (kg), given by the sum of CO_2 coming from internal production in Italy and import and subtracting the hourly CO_2 related to electricity exported in other Countries,

$$m_{tot,h} = m_{nren,h} + m_{ren,h} + m_{imp,h} - m_{exp,h}, \quad (7)$$

and the hourly electricity demand for Italy $EE_{tot,h}$ (kWh),

$$EE_{tot,h} = EE_{nren,h} + EE_{ren,h} + EE_{imp,h} - EE_{exp,h}. \quad (8)$$

It should be noted that the mass of carbon dioxide associated with electric energy exported to other countries is subtracted (just as the electric energy exported to other countries is). This is because the model's objective is to determine an hourly emission factor related to electric energy drawn from a device connected to the Italian power grid, rather than the total electricity flowing on the Italian power grid each hour but consumed in other countries.

The coefficient of grid losses for Italian power grid p (for years 2016-2019, [**3**]) is now introduced, in order to determine the final expression of hourly emission factor EF_h,

$$EF_h = \frac{m_{tot,h}}{EE_{tot,h}} p, \tag{9}$$

or, equivalently,

$$EF_h = \frac{EE_{nren,h} \cdot EF_{nren} + \sum_j EE_{ren,j,h} \cdot EF_j + \sum_k EE_{imp,k,h} \cdot EF_k - m_{int+imp,h} \cdot \frac{EE_{exp,h}}{EE_{int+imp,h}}}{\sum_k EE_{imp,k,h} + \sum_j EE_{ren,j,h} + EE_{nren,h} - EE_{exp,h}} p. \tag{10}$$

The use of coefficient p allows one to refer the emission factor to the electricity taken from a device connected to the Italian power grid instead of to the total hourly electric energy provided by the grid.

The 'detailed' model introduced in this section is used to ascertain the emission factors, EF_h, over a span of four years (2016-2019). The hourly emission factors for these four years are depicted in **Figure 6.5**, with each year offering 8,760 emission factor values, corresponding to the 8,760 hours of the year. It's evident from the figure that the hourly emission factor exhibits a periodic variation, with its magnitude diminishing during months that have a substantial renewable contribution. Furthermore, **Figure 6.5** highlights a consistent decline in the annual average value from 2016 through 2019.

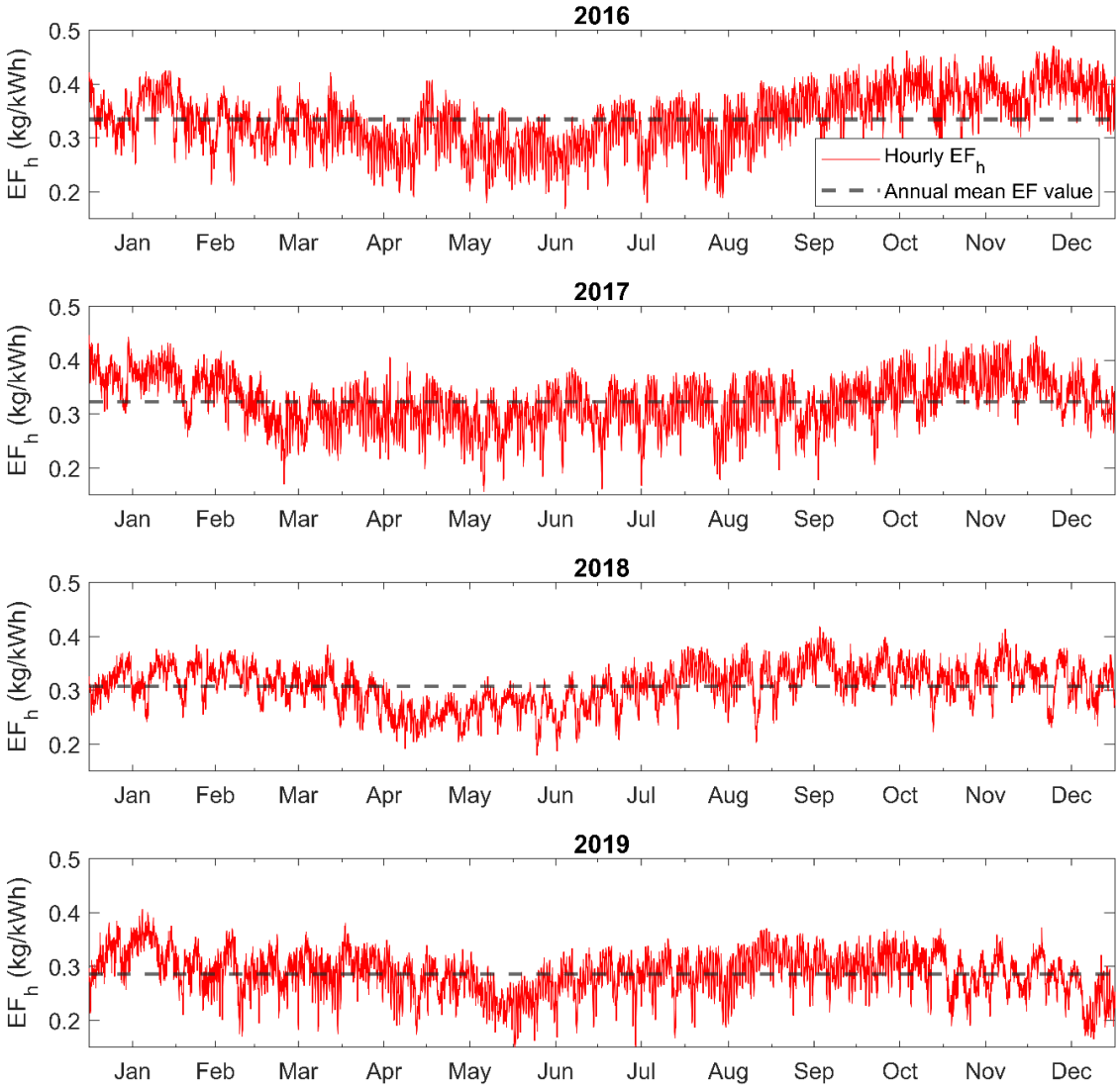

Figure 6.5 – Hourly and average annual emission factor (years 2016-2019).

The 'simplified' model will now be presented. This model defines a time-dependent function to represent the hourly emission factor previously identified. While the detailed model provides EF_h values for each hour of the considered year, the 'simplified' model approximates this with a periodic function defined by specific coefficients. This streamlined approach not only simplifies the analysis but also facilitates understanding the hourly emissions of a device linked to the electrical grid, introducing a predictable behavior pattern.

The hourly emission factor undergoes periodic fluctuations throughout the year, characterized by a 24-hour cycle. An appropriate approximation for the EF_h trend is an envelope function shaped by a sine curve, described as follows:

$$ef(t) = f(t)\Omega(t) + \big(1 - \Omega(t)\big)g(t) \qquad (11)$$

where *ef*(*t*) is the approximated hourly time-dependent emission factor, *f*(*t*) and *g*(*t*) are two polynomial functions and Ω(*t*) is a periodic function. The expressions of functions *f*(*t*), *g*(*t*) and Ω(*t*) are given by

$$\Omega(t) = \sin^2(\omega t + \delta) \tag{12}$$

$$f(t) = a_1 t^2 + b_1 t + c_1 \tag{13}$$

$$g(t) = a_2 t^2 + b_2 t + c_2, \tag{14}$$

where ω, δ, a_1, b_1, c_1, a_2, b_2, c_2 are coefficients determined in order to minimize the error of the approximated formula respect to the EF_h value given by the model.

The sinusoidal function in equation (11) was chosen to achieve a periodic function with a 24-hour cycle. This choice aligns well with the inherent 24-hour periodicity of the emission factor, as described by the 'detailed' model. The trend of the emission factor closely mirrors the daily electricity production pattern in Italy. The two functions, *f*(*t*) and *g*(*t*), represent the approximate maximum and minimum values the emission factor can achieve, effectively determining the amplitude of the final function that constitutes the 'simplified' model.

The coefficient values for the designated years are detailed in **Table 6.3**. Additionally, **Table 6.3** also presents the coefficients for a function driven by the mean values of the hourly EF_h across the years 2016-2019.

Table 6.3 – Coefficients for the approximated periodic function.

Coefficient	2016	2017	2018	2019	Average
a_1	3.83E-09	3.36E-09	1.75E-09	4.01E-10	2.08E-09
b_1	-2.4E-05	-2.7E-05	-1.1E-05	-6.3E-06	-1.5E-05
c_1	0.38544	0.39784	0.34238	0.34044	0.35575
a_2	5.35E-09	5E-09	2.18E-09	1.55E-09	3.85E-09
b_2	-3.9E-05	-4.3E-05	-1.7E-05	-1.5E-05	-3.1E-05
c_2	0.32248	0.33941	0.2985	0.27489	0.3175
ω	0.1309	0.1309	0.1309	0.1309	0.1309
δ	1.51	1.53	1.5	1.52	1.51

In **Figure 6.6** the coefficients of the upper and lower envelope functions (eqs. 13-14) are reported with reference to years 2016-2019; the trends of these functions are reported as well, excluding the year 2017. Despite the limited of amount of data available, we can observe a trend for the coefficients reported, excluding year 2017. For example, we can observe a decrease of coefficients a_1, a_2, c_1 and c_2, and an increase of b_1 and b_2 over the years. We underline that the decrease of the coefficients c_1 and c_2, evident if year 2017 is neglected, means that average annual emissions are reducing respect to time.

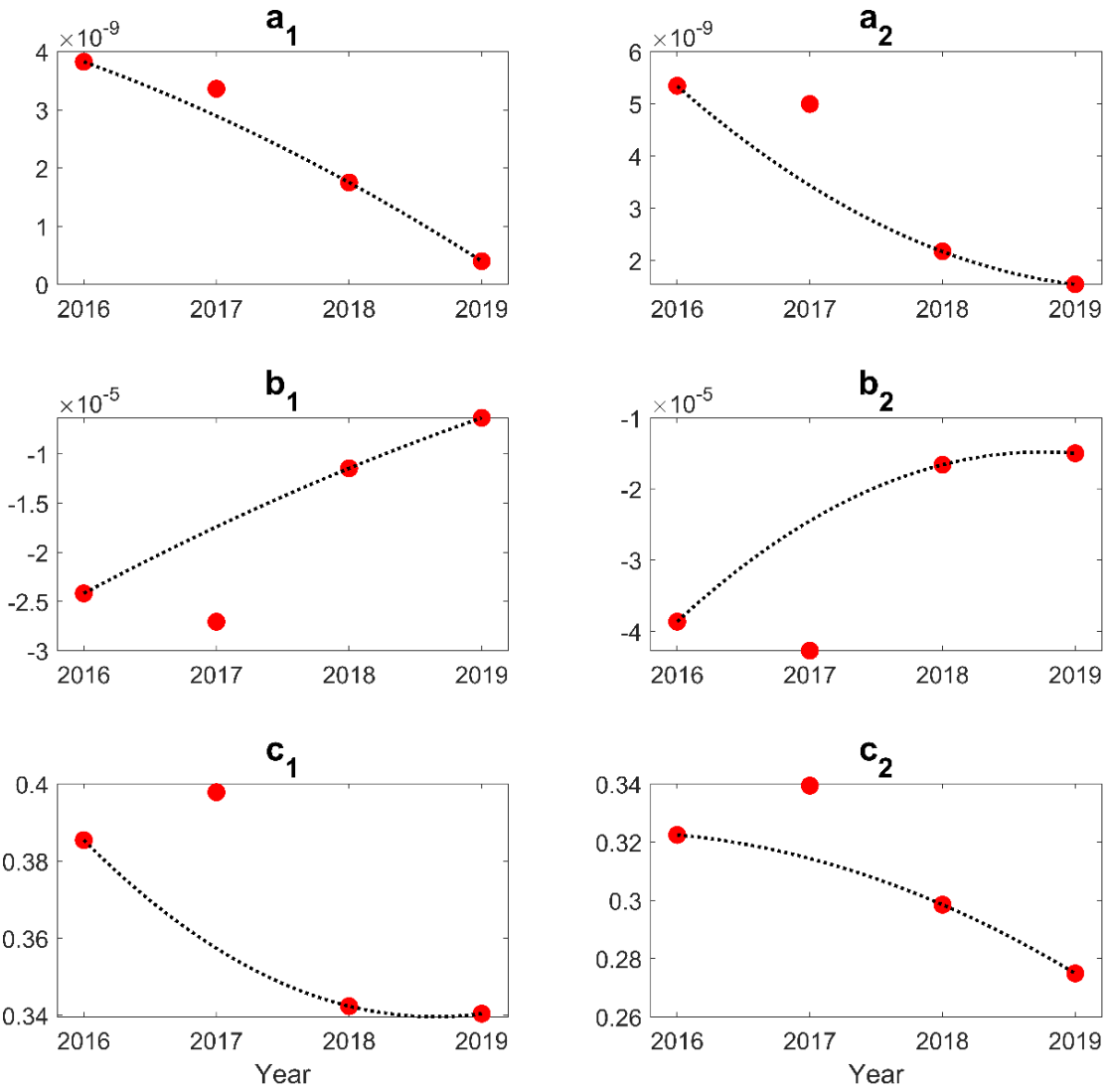

Figure 6.6. Coefficients of the upper and lower envelope functions and their trends (years from 2016 to 2019).

In **Figure 6.7** the hourly emission factor from the two models is reported, for years 2016-2019, for some specific (working) days, allowing a more evident comparison between real data and the interpolating function.

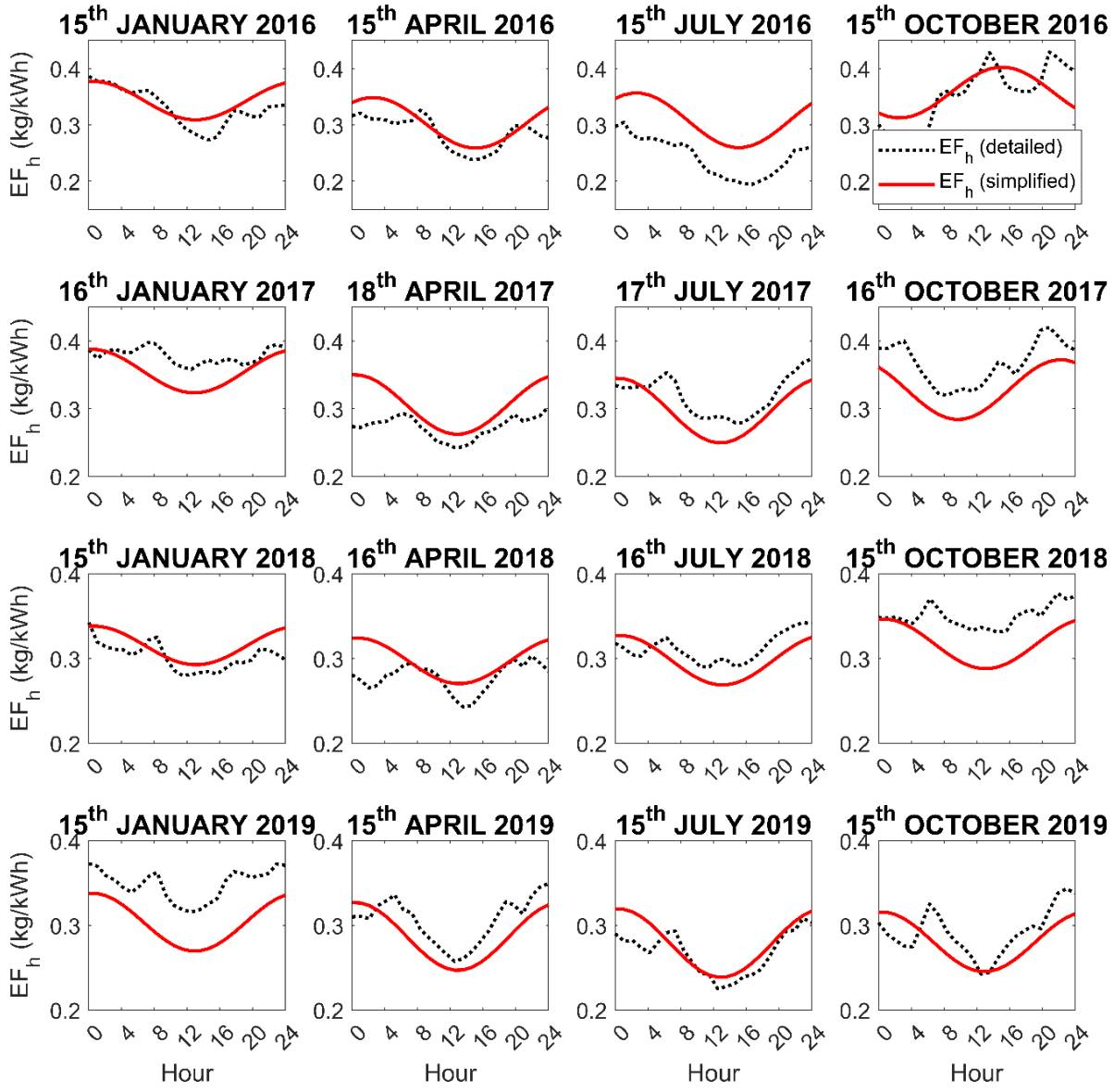

Figure 6.7 – Hourly emission factor from the detailed model and from the simplified model for some working days (years 2016-2019).

6.2 Determination of heat pump carbon dioxide emissions

The subsequent analysis will center on assessing the hourly carbon dioxide emissions stemming from an air-to-water heat pump that services a residential building situated in Milan. The building in question is based on the design proposed by IEA [**8**], specifically

a two-story family home with a space heating demand of 45 kWh/(m^2y) in Strasbourg's standard climate.

The building, as modeled in the simulations, spans a total floor area of 360 m^2. Its primary structural components, which include the floor, roof, and both internal and external walls, exhibit a transmittance that fluctuates between 0.241 W/m^2K and 0.885 W/m^2K.

For all thermal zones, an air change rate due to infiltration is assumed to be 0.3 h^{-1}. All windows are double-paned, featuring a 4-16-4 mm design filled with Argon gas. With the frame constituting 15% of the total window area (inclusive of both glass and frame), the cumulative transmittance of the window is estimated to be U-window = 1.5 W/m^2K. Thermal gains attributable to occupants and electrical equipment are considered dynamic throughout the day, as suggested in [**9**]. Specifically, the thermal contribution of a single occupant is bifurcated into two portions: 20 W from convection and 40 W from radiation. Similarly, thermal gains due to electrical devices are evenly allocated between convection and radiation. For any parameters not expressly detailed for conciseness, the values proposed by IEA Task 44 [**8**] for the SFH45 model are employed. In this study, the Trnsys software package serves as the modeling tool, utilizing the multizone building Trnsys Type 56 [**10, 11**].

In **Figure 6.8** the electric energy demand for heating and cooling season is reported. The total energy demand of the reversible air-to-water heat pump is 5079 kWh for heating season and 4150 kWh for cooling season.

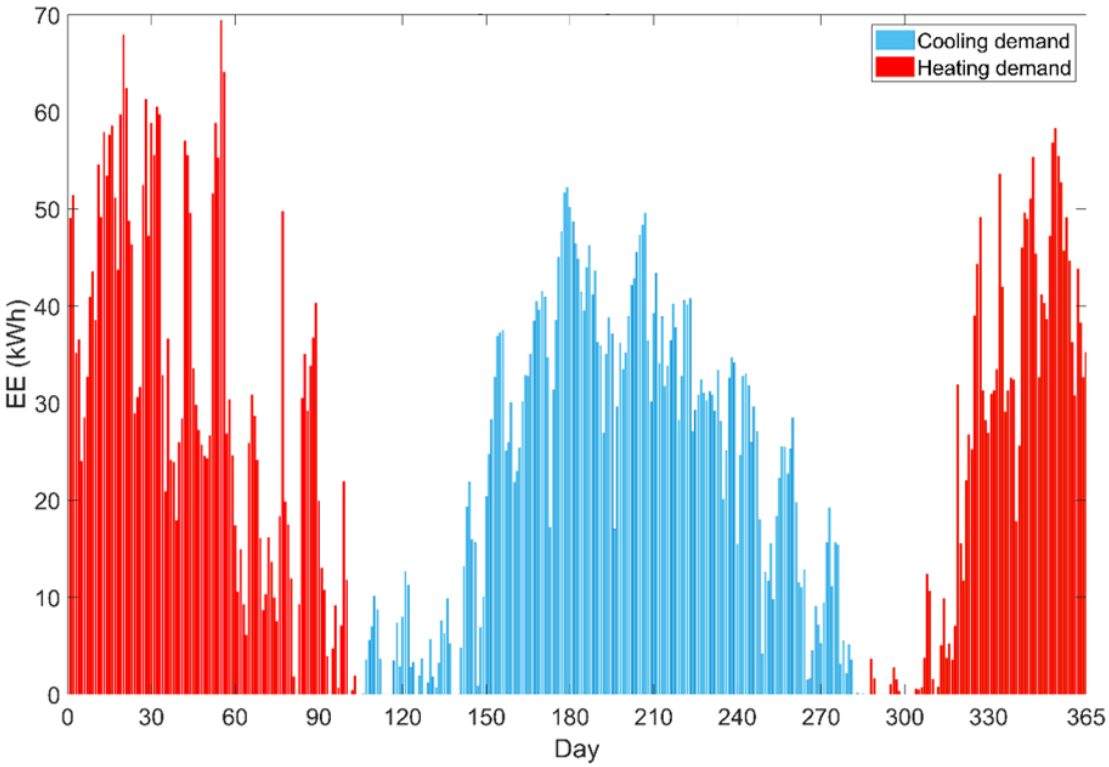

(**a**)

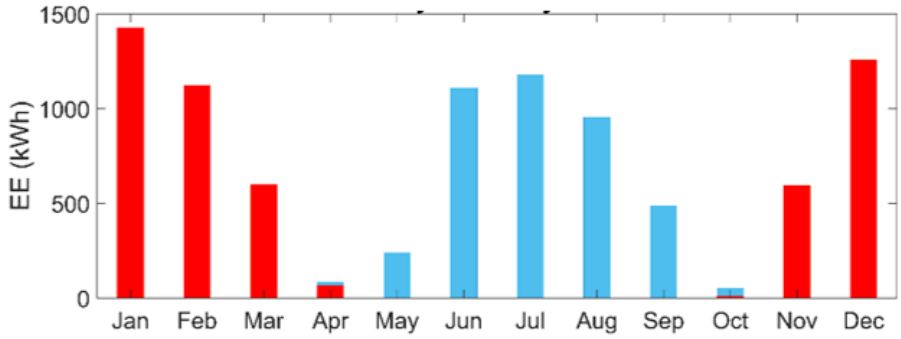

(**b**)

Figure 6.8 – Daily (**a**) and monthly (**b**) electricity demand of the heat pump for heating and cooling.

The emissions associated with the heat pump are detailed in **Table 6.4**. The calculated emissions are presented for both the heating and cooling seasons. The value is determined by multiplying the hourly electric energy demand for the entire season by the corresponding emission factor, as derived from both the detailed and simplified models. Additionally, a constant emission factor scenario is considered, where an average annual factor of 0.366 kg/kWh for 2016, 0.360 kg/kWh for 2017, 0.308 kg/kWh for 2018, 0.286 kg/kWh for 2019, and finally, an average factor of 0.313 kg/kWh is used.

Table 6.4 – Annual emissions for heating and cooling season in kg of CO2 and percentage error of the simplified model respect to the detailed model and percentage error of using a constant emission factor respect to the detailed model.

	Year	Constant emission factor	Detailed model	Simplified model	Error simplified model vs. detailed model (%)	Error constant emission factor vs. detailed model (%)
Annual emissions (kg) for heating	**2016**	1699	1832	1842	+0.55	-7.27
	2017	1639	1780	1798	+0.98	-7.94
	2018	1564	1628	1643	+0.87	+3.96
	2019	1454	1487	1514	+1.81	-2.21
	Averaged	1589	1682	1689	+0.42	-5.53
Annual emissions (kg) for cooling	**2016**	1388	1232	1241	+0.73	+12.71
	2017	1339	1213	1196	-1.41	+10.41
	2018	1278	1222	1210	-0.94	+4.58
	2019	1188	1122	1116	-0.51	+5.92
	Averaged	1298	1197	1190	-0.58	+8.46

The detailed model gives the most accurate information on carbon dioxide emissions. **Table 6.4** shows that the evaluations coming from the approximated model generally underestimate the annual emissions for cooling while overestimate the annual emissions for heating. This is due both to the fact that any approximation mathematically cannot give the same precision of detailed data, and to the fact that in winter season the overall contribution of the renewable sources is smaller than in summer. Now if is considered the average hourly values of the detailed model, and the average approximated periodic function, can be compared the results in terms of percent error: the use of the approximated mean function implies a small percentage error (0.42% for heating and 0.58% for cooling). Therefore, we can assert that average approximated periodic function can be used for estimating the emissions accurately, obtaining result

comparable to those obtained by the detailed model on yearly basis. On the contrary, the last column of **Table 6.4** shows that the constant emission factor induces a much less accurate estimation. In fact, in **Table 6.4** the percent error of the simplified model respect to the detailed model is reported for heating and cooling season, as well. We can observe that the function well approximates the carbon dioxide emissions for the case under investigation, with a maximum error of 1.8% for heating season and 1.4% for cooling. Therefore, it can be stated that yearly approximated functions well approximate the emissions given by the model.

Table 6.5 – Mean annual emission factor considering the net foreign exchange ($\overline{EF_n}$) and neglecting the exchange with other countries ($\overline{EF_{n,int}}$). In the last column is reported also the percentage difference in the two cases for years 2016 – 2019.

Year	$\overline{EF_n}$	$\overline{EF_{n,int}}$ **(Only internal production)**	**Difference (%)**
2016	0.334	0.366	8.6
2017	0.323	0.360	10.3
2018	0.308	0.346	11.1
2019	0.286	0.324	11.7

Table 6.5 presents the constant annual emission values when considering the exchange of electrical energy with foreign countries ($\overline{EF_n}$) and when only internal production is considered ($\overline{EF_{n,int}}$). It can be observed that the values obtained when not considering import and export to/from abroad are higher. **Figure 6.9** graphically illustrates the hourly emission factor values using the detailed model, both considering and neglecting foreign exchange. Here as well, one can observe that the values, when only considering

internal electric energy production (blue line), tend to be higher.

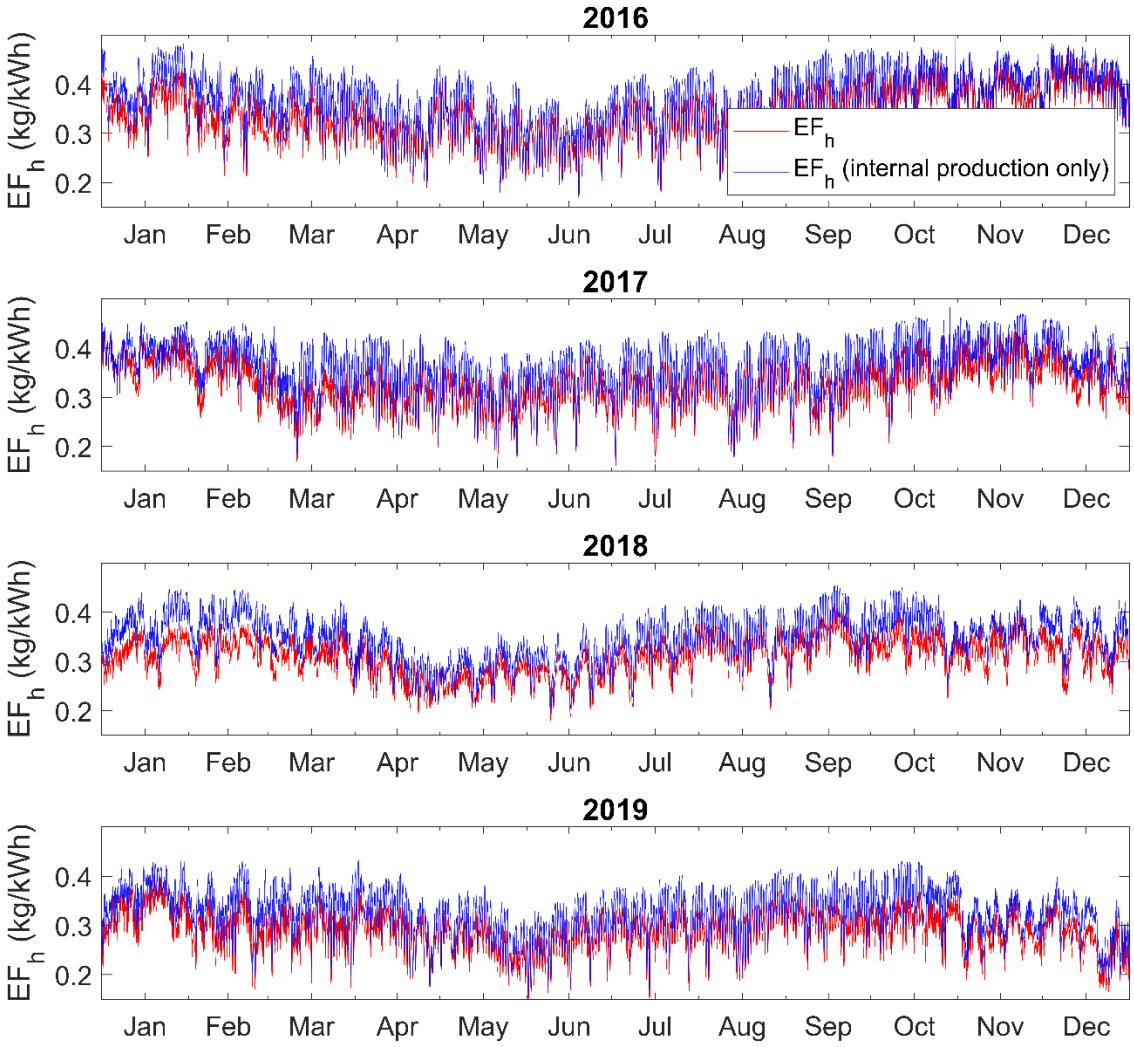

Figure 6.9 – Hourly emission factor considering and neglecting the electricity net foreign exchange with other countries.

6.3 Findings of the analysis

In this analysis, the emissions of a heat pump serving a residential building were presented. This was done after introducing a model (and its simplification) to determine hourly carbon dioxide emissions for electric devices connected to the national electricity grid in Italy, taking into account the net foreign exchange with other countries with which the national electric grid is interconnected. The main findings are as follows:

- Using constant emission factors tends to underestimate emissions for the heating season and overestimate them during the season when cooling is required for the building.

- The simplified model derived from the detailed model produced results similar to the detailed model.
- Emission factors determined by excluding net foreign exchange are higher than those considering it.

Lastly, using hourly emission factors compared to constant emission factors can be a key point in defining new control rules for the heat pump, with the aim of reducing emissions. For instance, in the case of a heat pump connected to a thermal storage, one could think of operating the heat pump more when the hourly emission factor is lower during the day, and then use the accumulated thermal energy during hours when the emission factor is higher.

References

[1]: Valdiserri, P.; Ballerini, V.; Rossi di Schio, E. Interpolating Functions for CO2 Emission Factors in Dynamic Simulations: The Special Case of a Heat Pump. *Sustainable Energy Technologies and Assessments* **2022**, *53*, 102725, doi:10.1016/j.seta.2022.102725.

[2]: Valdiserri, P.; Ballerini, V.; Rossi di Schio, E. Hourly Data for Evaluating the Carbon Dioxide Emission Factor of Heat Pumps or Other Devices Connected to the Italian Grid. *Data in Brief* **2022**, 108682, doi:10.1016/j.dib.2022.108682.

[3]: ref Terna TERNA. Statistical data on electricity in Italy. Available online: https://www.terna.it/it/ istemaelettrico/statistiche/pubblicazioni-statistiche (accessed on 2 October 2023).

[4]: ISPRA Atmospheric emission factors of greenhouse gases from power sector in Italy and in the main European countries. Edition 2020 — English (https://www.isprambiente.gov.it)

[5]: AIB (Association of Issuing Bodies). European Residual Mix Factors (various years). Available online: http://www.aib-net.org/facts/115uropean-residual-mix (accessed on 2 October 2023).

[6]: Terna Transparency Report - Download Center. Available online: https://www.terna.it/it/sistema-elettrico/transparency-report/download-center (accessed on 2 October 2023).

[7]: IPCC (Intergovernmental Panel on Climate Change). 5th assessment report - synthesis. Available online: https://www.ipcc.ch/report/ar5/syr/ (accessed on 2 October 2023).

[8]: Dott, R.; Haller, M.; Ruschenburg, J.; Ochs, F.; Bony, J. IEA-SHC Task 44 Subtask C Technical Report: The Reference Framework for System Simulations of the IEA SHC Task 44/HPP Annex 38: Part B: Buildings and Space Heat Load. 2013. Available online: https://www.semanticscholar.org/paper/The-Reference-Framework-for-System-Simulations-of-%2F-Dott-Haller/d3638ed65daa87f131266e19cd08aaed2eb43b46 (accessed on 2 October 2023).

[9]: E. Rossi di Schio, V. Ballerini, M. Dongellini, P. Valdiserri, Defrosting of air-source heat pumps: Effect of real temperature data on seasonal energy performance for different locations in Italy, «APPLIED SCIENCES», 2021, 11, pp. 1 – 15, https://www.doi.org/10.3390/app11178003.

[10]: Klein, S.A.; Duffie, A.J.; Mitchell, J.C.; Kummer, J.P.; Thornton, J.W.; Bradley, D.E.; Arias, D.A.; Beckman, W.A.; Braun, J.E. TRNSYS 17: A Transient System Simulation Program; University of Wisconsin: Madison, WI, USA, 2010.

[11]: Klein, S.A.; Duffie, A.J.; Mitchell, J.C.; Kummer, J.P.; Thornton, J.W.; Bradley, D.E.; Arias, D.A.; Beckman, W.A.; Braun, J.E. TRNSYS 17—A TRaNsient System Simulation Program, User Manual. Multizone Building Modeling with Type 56 and TRNBuild. Version 17.1; University of Wisconsin: Madison, WI, USA, 2010.

7 Energy Optimization Strategies Alternative or Combined to Heat Pumps: Building Insulation to Reduce Thermal Energy Demand

The previous chapters delved into the distinct characteristics of heat pumps. In this final chapter, we will not focus on heat pumps but will introduce two distinct analyses aimed at reducing the thermal demand of buildings. Moreover, these strategies can be synergistically combined with the adoption of heat pumps. The first section will discuss the use of repurposed materials (surgical masks) for building insulation. Instead of treating these masks as landfill waste, they can be repurposed to create insulating panels to be used in construction, replacing traditional insulants like rock wool and polystyrene. Experimental analyses have shown that the thermophysical properties of panels created with surgical masks are comparable to those of conventional building insulants. The latter part of the chapter will briefly present a dynamic analysis of an energy retrofit performed on an existing public building located in Bialystok, Poland. The same building was then virtually analyzed when located in northern Italy, specifically in Bologna.

7.1 Experimental analysis involving surgical face masks employed as insulant panels

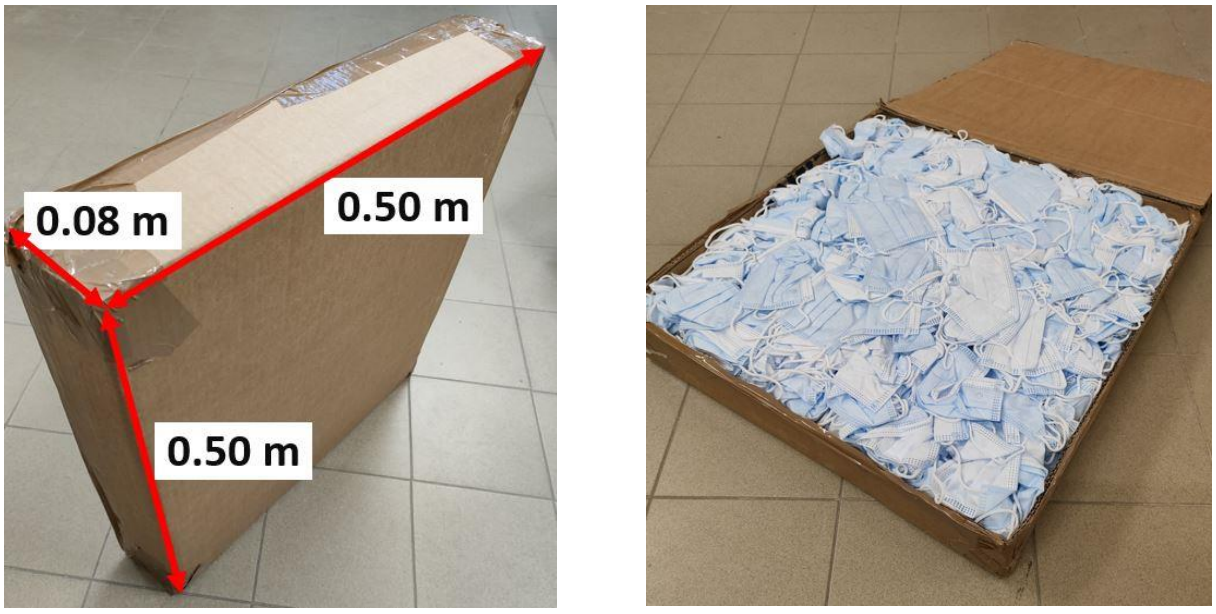

(**a**) (**b**)

Figure 7.1 – Carton box filled with surgical face masks (**a**); mask placed inside the carton box in disordered arrangement (**b**).

The idea, as previously indicated, is to repurpose surgical masks, which became widely used during the COVID-19 pandemic, to create insulating panels for construction. These

panels are essentially made up of cardboard boxes filled with used surgical masks that would otherwise be destined for landfill. Being panels crafted from commonly used materials, they are designed to be self-made by individuals at a low cost and can be particularly beneficial for social housing. **Figure 7.1** displays a photo of a cardboard panel filled with surgical masks, which can be used as insulation. This box also serves as a sample, measuring 0.50 x 0.50 x 0.07 m, and was used to perform thermal conductivity measurements in accordance with the standard [1]. In particular, the conductivity of the panels was determined by varying the amount of masks inside (and thus the overall density of the panel), the arrangement of the masks within the cardboard box, adding polyurethane foam, and removing the nose clip-on. The results and tests conducted are detailed in **Table 7.1**, along with the outcomes.

Table 7.1 – Test performed to determine the thermal conductivity (λ) for different densities (ρ) and different specimen composition.

Description	$\boldsymbol{\rho}$ **(kg/m^3)**	$\boldsymbol{\lambda}$ **(W/(mK))**
Masks in ordered arrangement	90.4	0.039
Masks in ordered arrangement	60.1	0.046
Masks in disordered arrangement	90.4	0.042
Shredded masks in polyurethane foam without clip-on	54.0	0.048
Crumped masks without clip-on	60.1	0.047
Crumped masks without clip-on (2 repetitions)	50.0	0.051 – 0.052*
Crumped masks without clip-on (2 repetitions)	40.0	0.055 – 0.059*
Crumped masks without clip-on (2 repetitions)	30.1	0.064 – 0.072*

*In these cases, two different thermal conductivity values are reported, since two test repetitions for each value of density have been performed; in the second test the masks have been rearranged in the carton box.

Based on the thermal conductivity results outlined in **Table 7.1**, the primary findings include:

- thermal conductivity decreases as the specimen density increases, particularly for crumpled masks (as shown in **Figure 7.2**).
- test repeatability is confirmed for specimen densities above 60 kg/m³.

- introducing polyurethane foam to adhere the masks within the cardboard box doesn't result in improved thermal conductivity.
- optimal thermal conductivity outcomes, comparable to those seen in commercial insulants, are achieved with specimen densities surpassing 60 kg/m³.
- tests without the nose clip-on yield superior performance, indicating lower thermal conductivity.

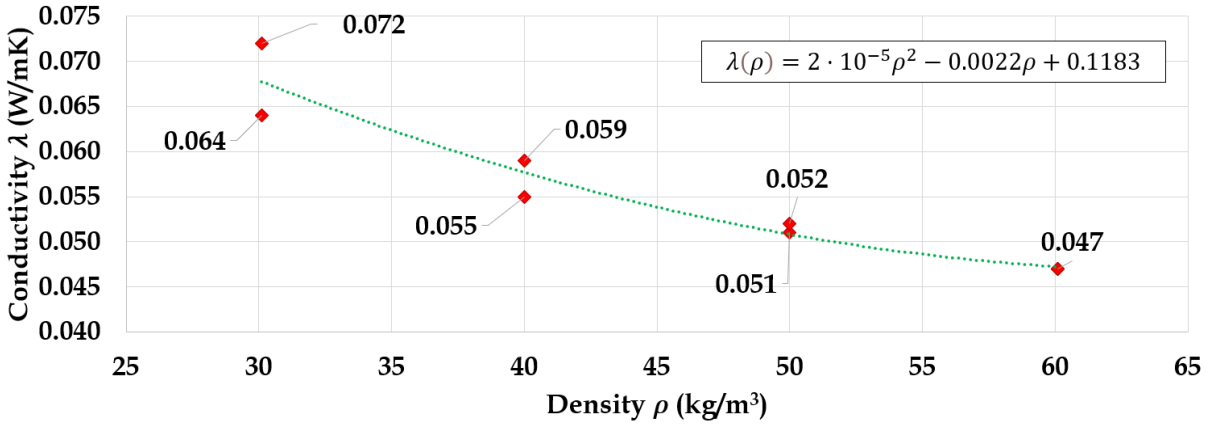

Figure 7.2 – Thermal conductivity trend function of the density; it is reported also the approximating function (green dashed line) and its expression.

The conductivity tests revealed that the obtained conductivity values are close to those of commercial materials used in construction when the samples have a density exceeding 60 kg/m³.

Figure 7.3 – Test specimen employed to assess the water vapor transmission of the surgical face masks.

Tests were also conducted to determine the vapor permeability of the masks. Specifically, a test was carried out where a sample of 25 masks was stacked and placed over a cylinder containing a saturated solution of water and potassium nitrate KNO_3

(**Figure 7.3**), which maintains a fixed relative humidity. The sample was then inserted into a test chamber and kept at a constant temperature and humidity of 23°C and 50%, respectively. The sample was weighed at time intervals of at least 24 hours, and the measurement results and their trend are shown in **Figure 7.4**. It can be observed that the masks are permeable to vapor, and the weight of the sample is practically a linear function of time, with a transmission rate of vapor of about 87.2 mg/h.

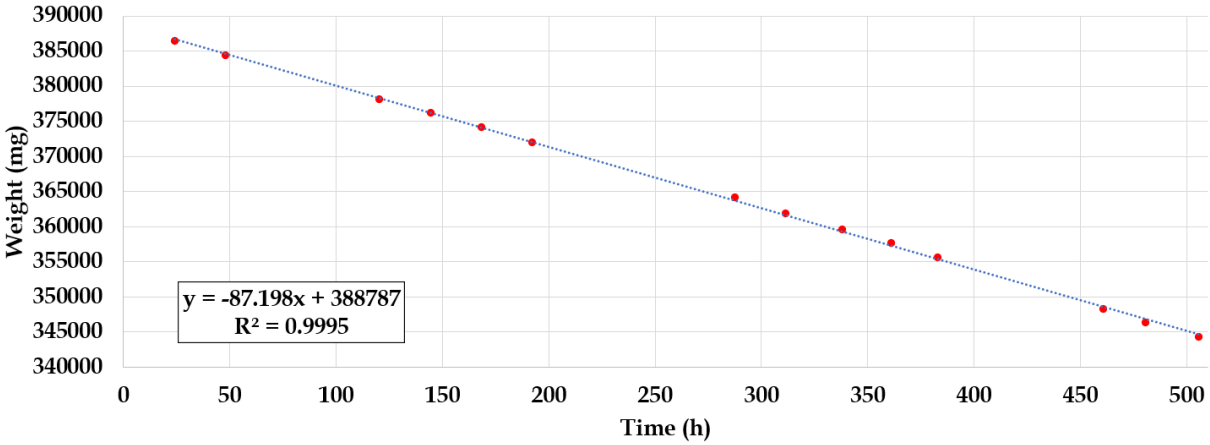

Figure 7.4 – Test specimen weight vs time to assess the water vapor transmission through the specimen.

7.2 Dynamic analysis of a residential building insulated employing panels filled with face masks

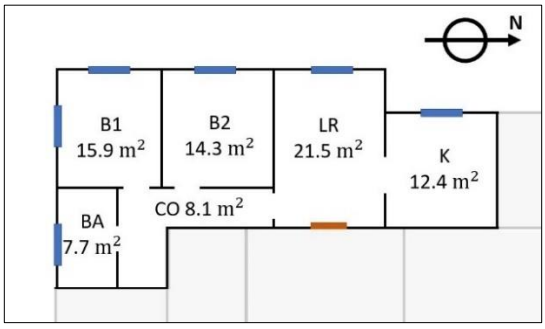

(a)

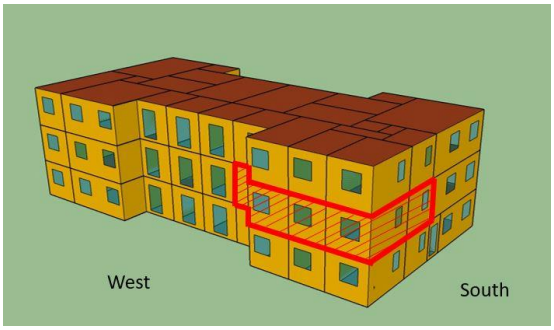

(b)

Figure 7.5 –Layout of the apartment **(a)**; 3D view of the apartment block, where the hatched red area indicates the apartment analyzed **(b)**.

To assess the possible energy saving achievable when panels made of surgical face masks are installed indoors, a dynamic numerical analysis has been performed using

Trnsys software package [2, 3]. According to **Figure 7.5**, the analysed apartment is on the first floor of a building block located in Milan (Italy).

Table 7.2 - Characteristics of the building envelope elements of the reference case (the apartment without insulation).

Envelope element	**Thickness (m)**	**U-value (W/m²K)**
External wall	0.34	1.302
Internal wall	0.18	1.364
Floor and ceiling	0.42	0.626
Dividing wall	0.10	1.958

It presents approximately 80 m^2 of floor area and is divided into six thermal zones. The characteristics of the building envelope elements are summarized in **Table 7.2**, and they are representative of Italian buildings constructed between 1970 and 1990. The standard heating season runs from October 15th to April 14th, encompassing 2404 heating degree days and a winter design temperature of -5°C. The hourly and average monthly outdoor temperatures are derived from the Meteonorm database [4]. The Energy Performance Index for Heating (EP_H), the Predicted Mean Vote (*PMV*), and the Predicted Percentage of Dissatisfaction (*PPD*) estimated in the various scenarios have been juxtaposed. Six scenarios have been investigated, in which different panels have been set up indoors as detailed in **Table 7.3** and **Table 7.4**.

Table 7.3 – Thickness, thermo-physical characteristics and transmittance values *U* of principal apartment envelope components after building insulation with surgical face masks, in three different cases a) /b) /c).

	Element	**Thickness (m)**	***Conductivity* (W/mK)**	***Thermal capacity* (kJ/kgK)**	***Density* (kg/m³)**
External wall	Plasterboard	0.015	0.20	1.45	660
	Insulant (masks)	0.08	0.04[a]/ 0.059[b]/0.066[c]	0.87	90

(*U* = 0.376[a]/ 0.495[b]/0.533[c] W/m²K)	Internal plaster	0.01	0.70	1	1400
	Hollow bricks	0.08	0.36	0.8	1000
	Air gap	0.16	-	-	-
	Hollow bricks	0.08	0.47	0.8	1000
	External plaster	0.01	0.90	0.8	1800
Internal wall (*U* = 0.372[a]/ 0.489[b]/0.525[c] W/m²K)	Plasterboard	0.015	0.20	1.45	660
	Insulant (masks)	0.08	0.04[a]/ 0.059[b]/0.066[c]	0.87	90
	Internal plaster	0.01	0.70	1	1400
	Hallow bricks	0.16	0.36	0.8	1000
	Internal plaster	0.01	0.70	1	1400

Table 7.4 – Parameters set in the dynamic analysis performed; density, specific thermal capacity and thermal conductivity refers to the insulating layer. S1 case refers to the non-insulated apartment, cases S2, S3 and S4 considers the surgical face masks as insulant (see **Table 7.3**), case S5 refers to rockwool insulant, and case S6 to polystyrene insulant.

Case	**External wall *U* (W/m²K)**	**Internal wall *U* (W/m²K)**	**Density (kg/m³)**	**Thermal capacity (kJ/kgK)**	***Conductivity* (W/mK)**
S1	1.302	1.364	-		
S2	0.376	0.372	90	0.87	0.039
S3	0.495	0.489	75	0.87	0.059

S4	0.533	0.525	60	0.87	0.066
S5	0.339	0.336	90	1.03	0.035
S6	0.347	0.343	20	1.45	0.036

Scenario S1 serves as the pre-renovation baseline. Scenarios S2-S4 incorporate insulating panels crafted from surgical face masks, while the final two scenarios, S5 and S6, utilize commercial insulating materials: mineral wool and polystyrene, respectively. The insulating panels have a uniform thickness of 0.08 m, but their density and thermal conductivity differ as detailed in **Table 7.4**. **Figure 7.6** delineates the placement of these insulating panels, with red lines indicating insulated external walls and green lines representing insulated internal walls. Positioned indoors on the vertical walls, these panels are paired with a 0.01 m thick plasterboard layer. Specifically, insulation is applied to all external walls and to internal walls that border the stairwell and neighboring units.

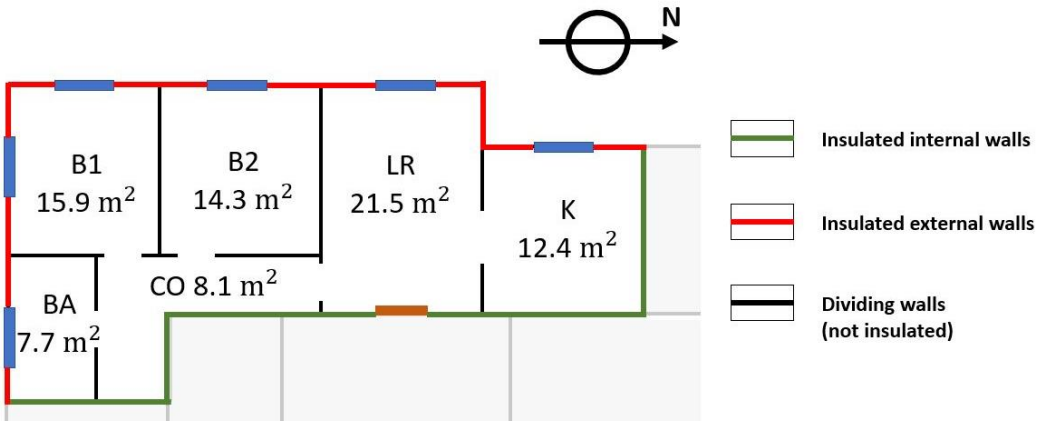

Figure 7.6 – Insulated walls in cases S2-S6.

The heating system is comprised of a boiler with an output capacity of 20 kW, linked to a storage tank with a volume of 0.1 m³. Five radiators are strategically placed across different thermal zones, excluding the corridor. The boiler's water temperature setpoint is set at 70°C. Thermal zones maintain a setpoint of 20°C from 6:00 am to 11:00 pm, dropping to 18°C during nighttime. For the bathroom, the daytime temperature setpoint stands at 24°C and drops to 18°C at night. The temperature for adjacent apartments is maintained at 20°C, while the temperature for the building's entrance, stairwells, and hallways is computed by the software. The average transmittance for windows, accounting for both the glass and frame, is 2.83 W/m²K. Internal gains are based on

the presence of four occupants and the usage of electrical equipment, following the standards set by IEA SFH Task 44 [**5**]. Across all thermal zones, the air exchange rate is set at 0.5 h^{-1}.

Table 7.5 – Annual results obtained by the simulations: thermal energy demand of the apartment *ET*, annual apartment energy demand related to the floor area (79.86 m^2) EP_H, and energy demand reduction of cases S2-S6 respect to case S1.

Case	***ET* (kWh)**	***EP*$_H$ (kWh/m^{2}y)**	**Annual *ET* reduction (kWh)**	**Annual percentage *ET* reduction (%)**
S1	7756	97.1	-	-
S2	4170	52.2	3586	46.2
S3	4586	57.4	3170	40.9
S4	4712	59	3044	39.2
S5	4070	51.0	3686	47.5
S6	4095	51.2	3661	47.2

The outcomes in terms of EP_H and thermal energy savings are presented in **Table 7.5**. Incorporating insulating panels crafted from masks (scenarios S2-S4) leads to an energy demand reduction ranging between 39% and 46%. In scenario S2, the energy consumption drops by 3586 kWh, a figure that aligns closely with the values established for scenarios S5 and S6, which employ commercial materials. This similarity can be attributed to the comparable thermal conductivity of the insulating panels. Dynamic simulations were also conducted to determine comfort indices for the various spaces within the building. The values used for *PMV* calculations can be found in **Table 7.6**.

Table 7.6 – Parameters employed to determine the *PMV*.

Variable	**Value**
Air temperature t_{air} (°C)	Obtained by simulation
Mean radiant temperature t_{mr} (°C)	Obtained by simulation

Relative humidity *UR* (%)	Obtained by simulation
Air velocity v_{air} (m/s)	Fixed (0.1 m/s)
Clothing factor *c* (clo)	Fixed (1 clo)
Metabolic rate *MR* (Met)	Fixed (1.1 Met)

The addition of insulating panels leads to an increase in surface temperature, which in turn results in a comprehensive improvement in comfort indices, as depicted in **Figure 7.7**. This figure showcases the comfort indices for the bathroom (BA) and the two rooms, B1 and B2, during the coldest day of winter in Milan. From the presented values, it's evident that both the insulation using mask panels (case S2) and commercial insulation (case S5) offer comparable enhancements in comfort. Therefore, it can be asserted that the dynamic analysis reaffirms that insulating panels made from masks yield results analogous to those achieved using commercial insulating panels, both in terms of the building's energy performance and in relation to comfort.

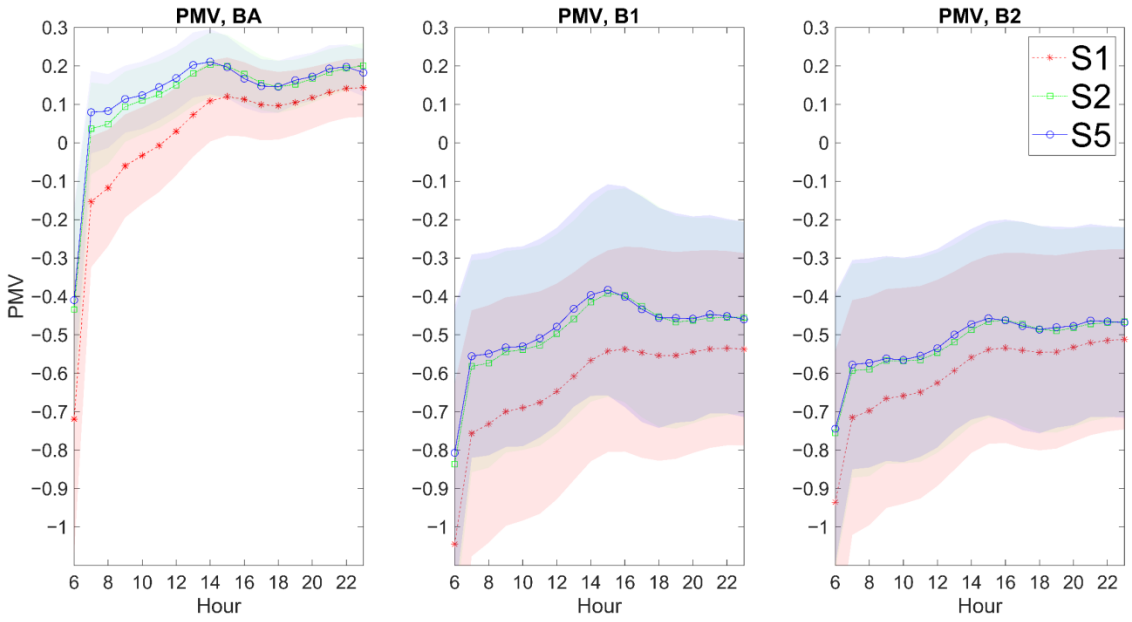

(**a**)

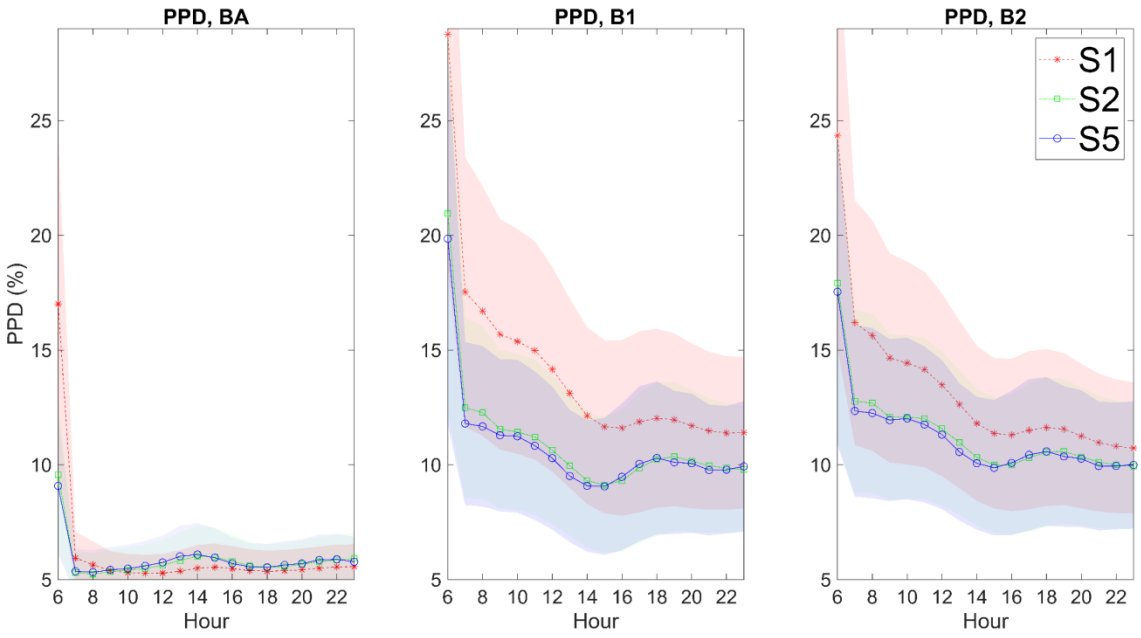

(**b**)

Figure 7.7 – *PMV* and *PDD* ((**a**) and (**b**) respectively) values for three thermal zones: BA, B1 and B2. The values reported as marks are the mean values of *PMV* and *PDD* calculated for each daily hour, for each heating season's day; the area represents the standard deviation.

7.3 Energy retrofit comparison between Italy and Poland

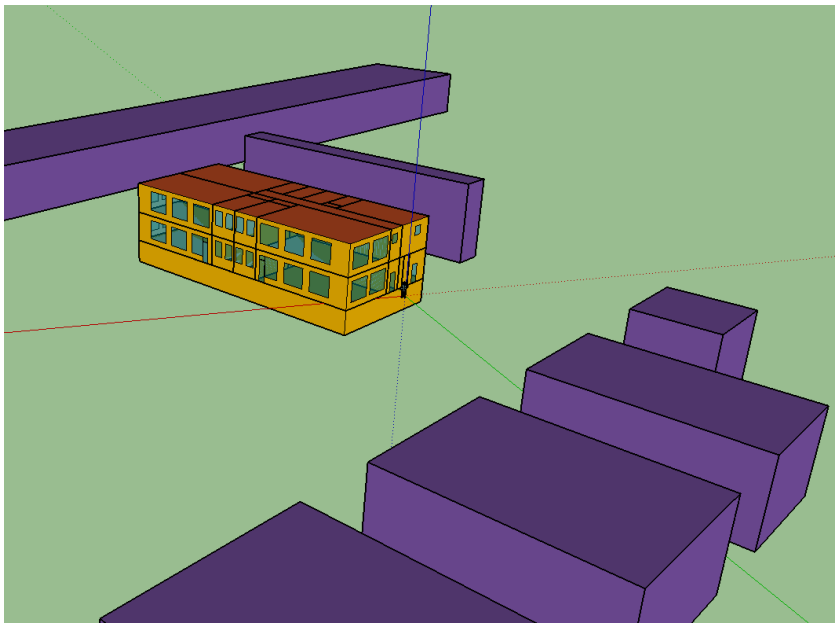

Figure 7.8 – 3D view of the kindergarten as implemented in Trnsys.

In the subsequent sections, an analysis conducted using the Trnsys software on an existing building located in Bialystok (Poland, PL), both before and after an energy

retrofit, will be presented. The building will then be virtually relocated to Bologna, and values from the dynamic simulations will be compared with actual energy consumption values obtained from measurements.

The building analyzed is a two-story kindergarten, featuring 6 classrooms, a kitchen, offices, and restrooms. A 3D view of it and the neighboring buildings that cast shadows upon it is visible in **Figure 7.8**. The total floor area is approximately 600 m^2 and the volume is about 1800 m^3, with room heights of 3 m. As can be seen from **Figure 7.8**, the building has large windows. Below the ground floor, there is a cellar with a height of 2.55 m, partly used as a technical room.

The considered building underwent a building retrofit process during the years 2019 – 2021 [**7**]; in particular, the external and ground-facing vertical walls were insulated, and the windows were replaced. The transmittance values before and after the intervention are reported in **Table 7.7**.

Table 7.7 – U-values prior and after building retrofit for the principal building envelope elements.

Zone	***U*** **(W/(m²K)) prior**	***U*** **(W/(m²K)) after**
External doors	2.500	1.300
Ground floor	2.604	2.604
Internal walls	2.110	2.110
Inter-floor (ground floor- cellar)	1.587	1.587
Inter-floor (ground – first floor)	2.041	2.041
Roof	3.165	0.166
Vertical walls	1.178	0.196
Vertical walls on the cellar	1.453	0.186
Windows	1.700	0.900

To conduct the climatic analysis using the Trnsys software, weather data were obtained from the PVGIS platform [**8, 9**]; specifically, a typical meteorological year was reconstructed by obtaining irradiation, relative humidity, temperature, and wind speed

and direction data from the platform. Data collected from [**8, 9**] shows that the climate in Bialystok is colder compared to Bologna; in January, for example, the average daily temperature reaches values close to -20°C, while in Bologna the average daily temperature rarely falls below 0°C. The main characteristics (winter design temperature, heating degree days, and annual average temperature) are reported in **Table 7.8**.

Table 7.8 – Main climatic parameters for Bologna and Bialystok.

	Białystok	**Bologna**
HDD	3763	2440
Mean annual temperature (°C)	9.3	13.9
Winter design temperature (°C)	-19	-5

The dynamic analysis was conducted considering the presence of 20 people in the classrooms from Monday to Saturday from 6:30 am to 5:30 pm, while in the offices and kitchen, the presence of 1 person was considered from 6:00 am to 6:00 pm, also from Monday to Saturday. A total contribution of 60 W per person was considered (where 20 W is the convective contribution and 40 W is the radiative contribution) [**5**]. The internal gains due to electrical appliances and lighting were quantified as 5 W/m^2 for the classrooms and offices, 20 W/m^2 for the kitchen, and 2.5 W/m^2 for all other rooms. These gains were considered only during the period of room usage. In the kitchen, a latent load due to the production of 1 kg/h of steam for cooking was also considered, limited to the period of room usage. Air changes were considered to be 0.5 h^{-1} in all rooms and the set point was set at 20°C in all rooms, except for the corridors, stairs, and entrance. The building is connected to the district heating network of the city of Bialystok, and the emission terminals are considered to be aluminum radiators. **Figure**

7.9 shows the layout of the building and the system implemented in Trnsys.

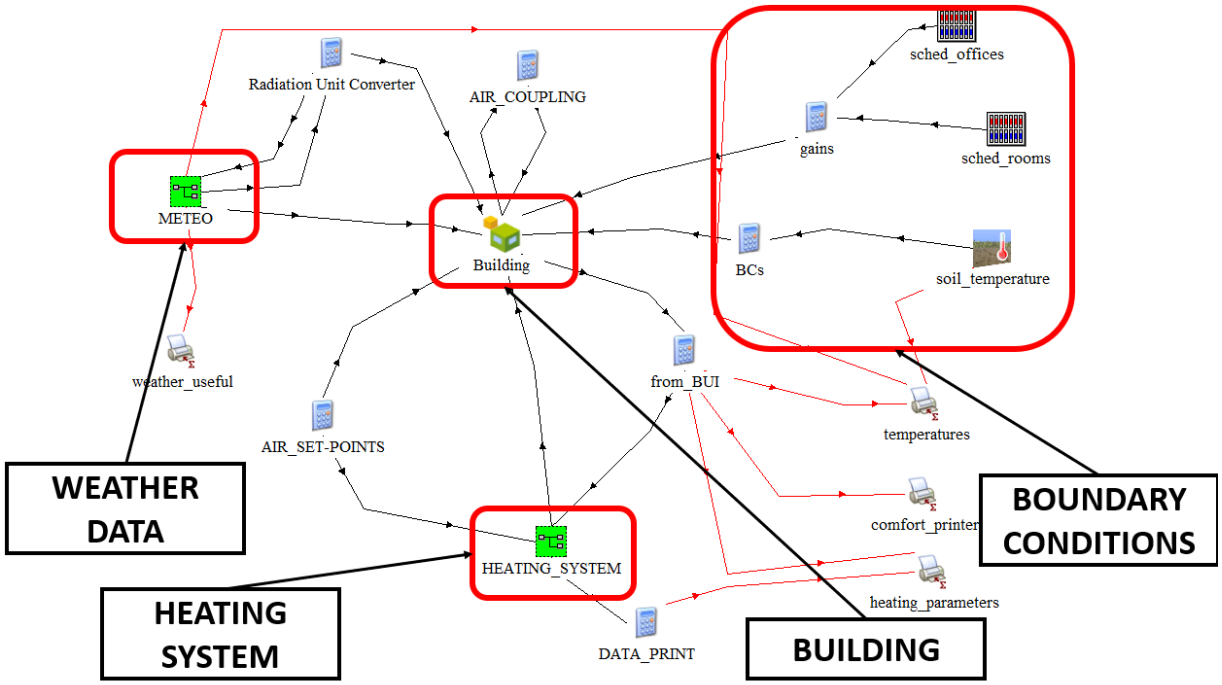

Figure 7.9 – Layout of the heating system and building as implemented in Trnsys.

In **Table 7.9** are reported the dynamic analyses results in terms of yearly thermal energy demand for heating (*ET*) and EP_H.

Table 7.9 – Annual energy demand for heating and EP_H for the building analyzed.

Case	Location	Building	*ET* (kWh/y)	EP_H (kWh/m²y)
S1	Białystok	Before Renovation	211269	343.5
S2	Białystok	After Renovation	68108	110.7
S3	Bologna	Before Renovation	122593	199.3
S4	Bologna	After Renovation	33471	54.4

The Trnsys analysis reveals that, considering the heating season and the data presented in **Table 7.9**, the percentage of energy reduction post-renovation is similar in Bologna and Białystok (a 72.7% reduction in S4 compared to S3 for Bologna, and a 67.8%

reduction in S2 compared to S1 for Białystok), despite the distinct heating degree days defining the two municipalities (2440 for Bologna and 3763 for Białystok). The decrease in annual thermal energy demand for buildings in Białystok and Bologna is 143161 kWh and 89122 kWh, respectively. It is observed that even in the presence of widely varying heating degree days between the two locations, following the energy retrofit, the dynamic analysis for the heating season yielded very similar values in percentage terms. The results obtained from the dynamic simulation were validated for case S2 with actual consumption results obtained from measurements at the considered kindergarten, and the comparison reveals a good fit of the values (range 0 – 19%), similar to that of other cases found in the literature [**10**].

References

[1]: BSI, British Standard Institution., 2001., Thermal performance of building materials and products - Determination of thermal resistance by means of guarded hot plate and heat flow meter methods - Products of high and medium thermal resistance, (Standard No. 12667).

[2]: A: Klein, S.A. et al, 2017, TRNSYS 18: A Transient System Simulation Program, Solar Energy Laboratory, University of Wisconsin, Madison, USA, http://sel.me.wisc.edu/trnsys (Accessed 2 October 2023).

[3]: Trnsys 42 Klein, S.A.; Duffie, A.J.; Mitchell, J.C.; Kummer, J.P.; Thornton, J.W.; Bradley, D.E.; Arias, D.A.; Beckman, W.A.; TRNSYS 17—A TRaNsient SYstem Simulation Program, User Manual. Multizone Building Modeling with Type 56 and TRNBuild. Version 17.1; University of Wisconsin: Madison, WI, USA, 2010.

[4]: Meteonorm version 8, https://meteonorm.com/ (Accessed 2 October 2023).

[5]: Dott, R.; Haller, M.; Ruschenburg, J.; Ochs, F.; Bony, J. IEA-SHC Task 44 Subtask C Technical Report: The Reference Framework for System Simulations of the IEA SHC Task 44/HPP Annex 38: Part B: Buildings and Space Heat Load. IEA-SHC.; 2013; http://www.taskx.iea-shc.org/data/sites/1/publications/T44A38_Rep_C1_B_ReferenceBuildingDescription_Final_Revised_130906.pdf (Accessed 2 October 2023).

[7]: Municipality of Białystok, (in Polish): Improvement of energy efficiency of PS No. 7, PS No. 52, PS No. 73, PS No. 42 and PS No. 71.;

https://www.Białystok.pl/pl/dla_mieszkancow/fundusze_unijne/realizowane/okresprogramowania20142020/poprawa-efektywnosci-energetycznej-ps-nr-7-ps-nr-52-ps-nr-73-ps-nr-42-i-ps-nr-71.html?vid=27822 (Accessed on 2 October 2023)

[8]: Huld, T.; Müller, R.; Gambardella, A. A New Solar Radiation Database for Estimating PV Performance in Europe and Africa. Solar Energy 2012, 86, 1803–1815, https://doi.org/10.1016/j.solener.2012.03.006.

[9]: JRC Photovoltaic Geographical Information System (PVGIS) - European Commission Available online: https://re.jrc.ec.europa.eu/pvg_tools/en/ (Accessed on 2 October 2023).

[10]: Krawczyk, D.A. Theoretical and real effect of the school's thermal modernization - A case study. Energy and Buildings 81 (2014) 30–37; https://doi.org/10.1016/j.enbuild.2014.04.058.

8. Activities performed during the three-year PhD programme

In this chapter, the main activities carried out during the three years of the doctoral program will be summarized. The works published during the doctorate are reported in the References section of this chapter. Throughout the 3 years of the doctorate, results have been presented at international conferences (participation at the UIT International Heat and Mass Transfer Conference in 2021, 2022, and 2023, and at the Carnot User Meeting held in Bologna in June 2023).

The first year of the PhD programme was devoted to investigating in-depth the effect of real climatic conditions on the seasonal indexes of air-to-water heat pumps, exploring the literature on this topic, and performing dynamic analyses using Trnsys software. Additional analyses on on-off and inverter heat pumps were also performed [**1, 2**]. A significant portion of the time was spent to properly understand the use of this simulation software and to analyse the obtained results. During this year, analyses of the variations in the performance of heat pumps with changing climatic conditions were carried out [**3**], as well as analyses on defrost [**4**].

The second year was dedicated to conducting experimental analyses on heat pumps at the Technical Physics laboratory of the University of Bologna on a prototype of a dual-source heat pump [**5**] and on insulating panels to be used in building and created with reused materials (surgical masks) [**6**]. A significant part of the year was dedicated to analysing the emissions due to heat pumps and determining the hourly emission factors for electrical devices connected to the national electricity grid [**7, 8**]. Finally, part of the time was dedicated to dynamic and economic analysis to determine the cost differences in heating buildings with heat pumps and gas boilers [**9, 10**].

The third year was dedicated to analysing comfort inside the residential building in Bologna, to assess the influence of different heating systems on thermal comfort perception (gas boiler combined with radiators and air-to-air heat pump) [**11**]. 3 months were spent conducting research abroad in Bialystok, Poland, where a public building (a kindergarten) was analysed with dynamic simulation software, before and after an energy retrofit intervention. During this year, dynamic analyses related to the geothermal heat pump assisted by solar collectors were also carried out [**12**].

References

[1]: Paper: Rossi di Schio, E.; Ballerini, V. THE SCOP OF AN AIR SOURCE HEAT PUMP: COMPARISON BETWEEN ON-OFF AND INVERTER HEAT PUMP. JPHMT 2021, 24, 79–86, https://doi.org/10.17654/HM024010079.

[2]: Paper: Rossi di Schio, E.; Ballerini, V.; Valdiserri, P. The Bin Method to Investigate the Effect of Climate Conditions on the SCOP of Air Source Heat Pumps: The Italian Case. 1790-5044 2022, 17, 124–130, https://doi.org/10.37394/232012.2022.17.13.

[3]: Paper: Ballerini, V.; Dongellini, M.; Schio, E.R. di; Valdiserri, P. Effect of Real Temperature Data on the Seasonal Coefficient of Performance of Air Source Heat Pumps. J. Phys.: Conf. Ser. 2022, 2177, 012025, https://doi.org/10.1088/1742-6596/2177/1/012025.

[4]: Paper: Rossi di Schio, E.; Ballerini, V.; Dongellini, M.; Valdiserri, P. Defrosting of Air-Source Heat Pumps: Effect of Real Temperature Data on Seasonal Energy Performance for Different Locations in Italy. Applied Sciences 2021, 11, 8003, https://doi.org/10.3390/app11178003.

[5]: Paper: Dongellini, M.; Ballerini, V.; Morini, G.L.; Naldi, C.; Pulvirenti, B.; Rossi di Schio, E.; Valdiserri, P. A New Climate Chamber for Air-Source and Ground-Source Heat Pump Testing Based on the Hardware-in-the Loop Approach: Design and Cross Validation. Journal of Building Engineering 2023, 64, 105661, https://doi.org/10.1016/j.jobe.2022.105661.

[6]: Conference proceedings: Ballerini, V., Caniato, M., Neri, M., Pilotelli, M., Rossi Di Schio, E., Valdiserri, P., THERMOPHYSICAL CHARACTERIZATION OF SURGICAL MASKS FOR POSSIBLE REUSE IN BUILDING REFURNISHING, 39th UIT International Conference, 20-22 June 2022, Gaeta (Italy), conference proceedings

[7]: Paper: Valdiserri, P., Ballerini, V., Rossi Di Schio, E., Interpolating functions for CO2 emission factors in dynamic simulations: the special case of a heat pump, Sustainable Energy Technologies and Assessments 2022, 53, 102725, https://doi.org/10.1016/j.seta.2022.102725.

[8]: Paper: Valdiserri, P., Ballerini, V., Rossi Di Schio, E., Hourly data for evaluating the carbon dioxide emission factor of heat pumps or other devices connected to the Italian grid, Data in Brief 2022, 108682, https://doi.org/10.1016/j.dib.2022.108682.

[9]: Paper: Ballerini, V.; Rossi di Schio, E.; Valdiserri, P. How the Energy Price Variability in Italy Affects the Cost of Building Heating: A Trnsys-Guided Comparison between Air-Source Heat Pumps and Gas Boilers. Buildings 2022, 12, 1936, https://doi.org/10.3390/buildings12111936.

[10]: Paper: Ballerini, V., Rossi Di Schio, E., Replacement of gas boilers with air source heat pumps: An economic analysis based on a trnsys evaluation and on the actual energy prices in Italy, JPHMT 2022, 30, 151–160, https://doi.org/10.17654/0973576322061.

[11]: Conference proceedings: Ballerini V., Palka Bayard de Volo E., Pulvirenti B., Rossi di Schio E., Valdiserri P., Guidorzi P., Influence of different heating systems on thermal comfort perception: a dynamic and CFD analysis, 40th UIT International Conference, June 26 -28 2023, Assisi (Italy, IT)

[12]: Paper: Ballerini, V.; Rossi di Schio, E.; Valdiserri, P.; Naldi, C.; Dongellini, M. A Long-Term Dynamic Analysis of Heat Pumps Coupled to Ground Heated by Solar Collectors. Applied Sciences 2023, 13, 7651, https://doi.org/10.3390/app13137651.

Conclusions

The main topics analyzed in this work can be summarized as follows:

- Influence of varying climatic conditions on heat pump performance
- Impact of the defrost effect on air heat pumps
- Experimental analyses on dual-source heat pumps
- Dynamic analysis of a heat pump assisted by thermal solar collectors with ground refill during the summer season
- Economic and comfort analysis between heating systems with heat pumps and gas boilers
- Analysis of emissions from a heat pump connected to the Italian electrical grid
- Solutions for energy efficiency in buildings and the use of reused materials in construction.

The principal findings from the analysis related to climatic conditions, considering actual climatic values (temperature, irradiation, relative humidity, and wind direction and speed) for buildings located in three Italian locations with different climates (Milan, S. Benedetto del Tronto, and Livigno), are a significant difference in the building's thermal demand from one year to the other (up to 37%) but more limited differences in terms of SCOP (up to 7%). The defrost analysis, conducted for a heat pump serving a residential building virtually located in the three aforementioned Italian locations, showed that the thermal demand and the SCOP are significantly influenced by the defrost effect, and the heat pump's electrical energy demand can increase up to 16% if defrost is considered compared to when it is neglected. Moreover, the analysis revealed that if the test reference year is used for the three locations, the number of defrost cycles are generally underestimated compared to using actual weather data.

Subsequently, hybrid systems for heating were analyzed, specifically, a dual-source heat pump was analyzed in the laboratory, and a dynamic analysis was conducted to determine the performance of geothermal heat pumps solar-assisted with ground refill during the summer. The analyses highlighted the advantages of using ground – coupled heat pumps coupled to thermal solar collectors. The dynamic analysis considering the refill, on the other hand, confirmed the presence of the stabilization of the soil temperature drift and the heat pump's SCOP after 15 years of operation if ground refill is adopted. This strategy is useful for buildings presenting imbalances between winter and summer load demand and is useful because the refill can be exploited using smaller

probe fields, while maintaining good heat pump performance and limited soil temperature drift.

The dynamic analysis related to the economic aspects of using heat pumps instead of gas boilers combined with radiators showed that the operating costs of the heat pump remained lower in almost all the analyzed cases, even following the increases in energy material prices in Italy due to the Russian-Ukrainian conflict. However, the analysis (dynamic, experimental, and CFD) related to comfort showed substantial differences between the two possible heating systems applied in residential sector: in particular, using an air-to-air heat pump compared to a gas boiler combined with radiators results in a decrease in comfort indexes inside the heated environments, mainly due to the lower radiant temperature of the environment in the case of using an air-to-air heat pump, which transfers heat to the internal environment primarily by convection (radiators, on the other hand, transfer heat to the environment in which they are positioned by convection and irradiation). Furthermore, the CFD analysis showed possibilities of local discomfort in environments due to the incorrect positioning of the internal unit and highlighted the importance of adequate design of heat pump systems to limit discomfort situations.

The analysis related to emissions aimed to obtain hourly values of CO_2 emissions related to devices connected to the Italian electricity grid. These values were then used to determine the emissions related to a heat pump: in this case, it was observed that the use of the constant annual emission factors instead of the hourly ones leads to an underestimation of the thermal machine's emissions during the heating season and an overestimation during the summer period (differences up to 12.7%); hourly emission factors can also be a key point to determine new control logics aimed at minimizing emissions.

The decarbonization process also includes the theme of energy efficiency of the building envelope; dynamic savings obtainable from an energy retrofit on an existing building in Bialystok were analyzed. The building was then virtually positioned in Bologna and the dynamic analysis showed that in percentage terms the reductions in thermal energy following the energy retrofit are comparable in the two locations, despite them having a very different climate.

Finally, to complete the picture of possible activities to carry forward the decarbonization process, the focus was on the concept of circular economy and reuse: experimental and dynamic analyses were carried out on insulating panels to be used in construction and

formed from reused materials (surgical masks that would otherwise be considered waste after being used for their main purpose). The experimental results confirmed the low thermal conductivity of the masks, comparable to that of commercial insulators (minimum thermal conductivity of 0.039 W/(mK) for a test specimen made of surgical face masks of 90 kg/m^3); moreover, the results obtained from the dynamic analysis on a residential building insulated with mask panels are similar to the results obtained considering commercial insulation.

Acknowledgments

I would like to express my gratitude to Professor Rossi di Schio for the support, advice, and availability provided to me throughout this doctoral journey. Heartfelt thanks also go to those who have supported me and with whom I have shared moments, both in the doctoral journey and in everyday and private life.